

“Ideal” Topological Heavy Fermion Model in Two-dimensional Moiré Heterostructures with Type-II Band Alignment

Yunzhe Liu,¹ Anoj Aryal,² Dumitru Calugaru,³ Zhenyao Fang,² Kaijie Yang,⁴
Haoyu Hu,⁵ Qimin Yan,² B. Andrei Bernevig,^{3,5,6} and Chao-xing Liu*¹

¹*Department of Physics, The Pennsylvania State University, University Park, Pennsylvania 16802, USA*

²*Department of Physics, Northeastern University, MA 02115*

³*Department of Physics, Princeton University, Princeton, NJ 08544*

⁴*Department of Materials Science and Engineering,*

University of Washington, Seattle, Washington 98195, USA

⁵*Donostia International Physics Center, P. Manuel de Lardizabal 4, 20018 Donostia-San Sebastian, Spain*

⁶*IKERBASQUE, Basque Foundation for Science, Bilbao, Spain*

(Dated: July 9, 2025)

Topological flat bands play an essential role in inducing exotic interacting physics, ranging from fractional Chern insulators to superconductivity, in moiré materials. When topological flat bands possess concentrated quantum geometry, a topological heavy fermion (THF) model was proposed as the starting point to describe the interacting moiré physics. In this work, we propose a design principle for realizing “ideal” THF model, which can host an exact flat band with “ideal quantum geometry”, namely the trace of Fubini-Study metric equals to the Berry curvature, in a class of two-dimensional moiré heterostructures with type-II band alignment. We first introduce a moiré Chern-band model to describe this system and show that topological flat bands can be realized in this model when the moiré superlattice potential is stronger than the type-II atomic band gap of the heterostructure. Next, we map this model into a THF model that consists of a localized orbital for “f-electron” and a conducting band for “c-electron”. We find that both the flatness and quantum geometry of the mini-bands in this THF model depend on the energy gap between c-electron and f-electron bands at Γ which is experimentally controllable via external gate voltages. This tunability will allow us to realize an “ideal” topological flat band with zero band-width and “ideal quantum geometry” in this THF model. Our design strategy of topological flat bands is insensitive of twist angle. We also discuss possible material candidates for moiré heterostructures with type-II band alignment.

I. INTRODUCTION

The discovery of flat bands in two-dimensional (2D) moiré materials, including twisted bilayer graphene (tBG) [1–18] and twisted transition metal dichalcogenides (TMDs) [19–37], has sparked intense research interest due to their potential to host exotic correlated phases [22, 38–43], such as superconductivity and fractional Chern insulators. Unlike flat bands associated with localized atomic orbitals in a trivial insulator, the flat bands in these moiré materials possess nontrivial quantum geometry [4, 9–15, 27–30, 38, 43–50] characterized by Berry curvature and Fubini-Study metric, which plays a crucial role in the emergence of exotic correlated states like the fractional Chern insulator phase [13, 51–57]. Quantum geometry generally obeys the trace condition, where the trace of Fubini-Study metric has a lower bound set by the magnitude of Berry curvature. When the “ideal quantum geometry” condition [58], namely, the trace of Fubini-Study metric equals the Berry curvature, is satisfied, it has been shown [13, 55–57, 59] that the fractional Chern insulator phase emerges as the ground state under short-ranged electron-electron interaction for topological flat bands. It was theoretically proposed that the ideal quantum geometry condition is satisfied in a tBG model under the “chiral” limit [8, 13] with a vanishing tunneling between the AA sites, which *cannot* can

be directly applied to the realistic tBG systems [60, 61]. An experimentally feasible and tunable platform to realize topological flat bands with ideal quantum geometry is desirable for exploring interacting topological states and other correlated states in moiré materials.

In certain moiré systems like tBG, where the nontrivial quantum geometry is localized around specific regions in the moiré Brillouin zone (mBZ), a topological heavy fermion (THF) model [12, 62–65] provides a compelling theoretical framework for understanding the coexistence of local moment behavior from strongly interacting localized states and metallic/superconducting behaviors from conducting states, and thus can serve as a starting point to understand a variety of interacting physics [12, 64, 66–71]. Despite these theoretical advancements, a significant challenge lies in identifying new two-dimensional (2D) moiré materials exhibiting THF physics, i.e. heavy fermion simulators [64].

In this work, we tackle these challenges by proposing a design paradigm for realizing an “ideal” THF model, in which the topological flat bands with ideal quantum geometry can be achieved by tuning external gate voltages, using moiré heterostructures composed of 2D materials with type-II band alignment. The design principle of the THF model in moiré heterostructures is illustrated in Fig.1. The THF model consists of the conducting electrons, called “c-electron”, and the localized

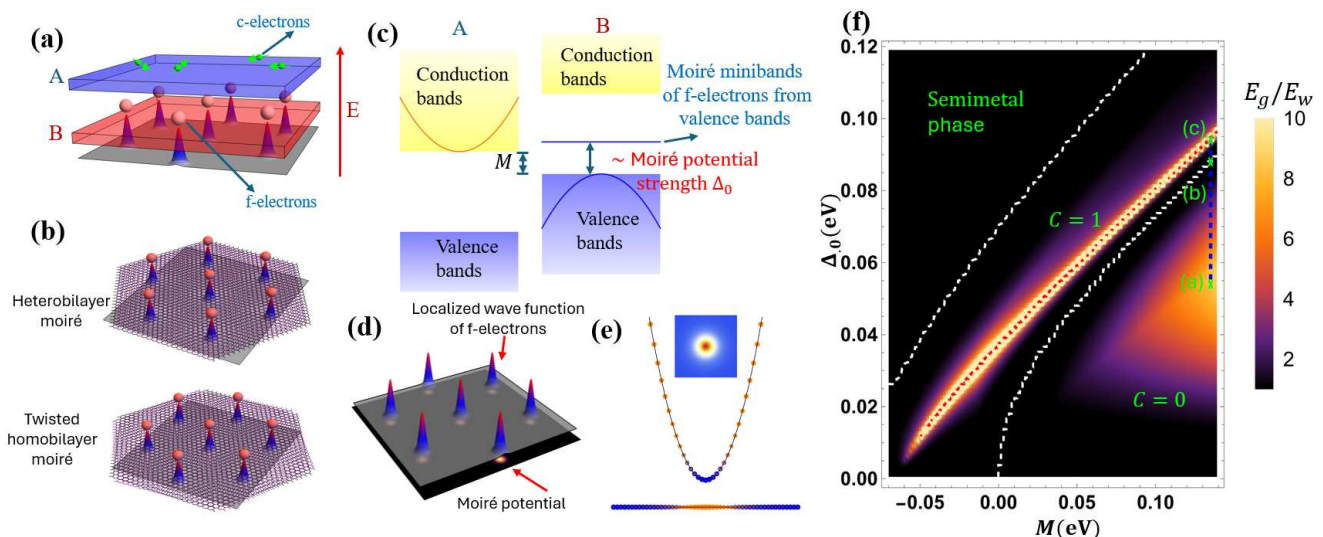


FIG. 1. (a) Illustration of the setup, which consists of two parts, A and B. In part A, electrons with a small effective mass behave as itinerant “c-electrons”, depicted by green spheres. In part B, the electron wavefunctions are periodic and localized due to moiré potential, and can be regarded as “f electrons”, depicted by pink spheres. An electric field can be applied to tuning band alignment between the parts A and B. (b) Part B can be formed by either twisted homobilayers or heterobilayers. The moiré potential arises from twisting or lattice mismatch. (c) Illustration of type-II band alignment. The conduction and valence bands originate from the parts A and B, respectively. The atomic band gap of the heterostructure is labeled as M . Due to the moiré potential, the moiré mini-band from the top valence band can become flat and shift upward in energy. When the strength of the moiré potential Δ_0 is larger than M , band inversion can occur, leading to a topological flat band. (d) Schematic figure of localized wavefunctions at the peak positions of moiré potential. (e) The formation of topological flat band after band inversion in the THF model. The sizes of orange and blue dots represent the contribution from “c-electrons” and “f-electrons”. Inset shows the concentration of Berry curvature around Γ . (f) Phase diagram for $\Delta_0 > 0$. E_g and E_w denote the band gap between VB1 and the other minibands and the bandwidth of VB1, respectively. The background color shows E_g/E_w . White dashed lines separate different phases and the red line guides the peak for E_g/E_w of VB1.

electrons, dubbed “f-electron”. Our setup in Fig.1(a) includes two parts, part A, which is made of 2D material with high mobility conduction bands to provide c-electrons, and part B for f-electron, which is realized via 2D moiré materials either by forming a superlattice potential in a moiré hetero-bilayer or twisting the 2D material homo-bilayer, as shown in Fig.1(b). Due to the moiré potential, the highest-energy moiré miniband from the valence band in part B gets localized and forms periodic bound states for f-electrons, as schematically shown in Fig.1(d). Since conduction band electrons normally have a smaller effective mass compared to valence band electrons in many semiconducting compounds, we below assume the c-electron is from the conduction bands of part A while the f-electron is from the valence bands of part B. But it should be pointed out that it is also possible to interchange the roles of the conduction and valence bands, namely the c-electron is from the valence band of part B while the f-electron is from the conduction band of part A, when the moiré potential is imposed on part A. To be concrete, we here consider all the low-energy bands around Γ in the atomic Brillouin zone (ABZ). In order to form topological flat bands with c- and f-electrons, two criteria are required: (1) the energy difference between the conduction band minimum (CBM) in part A and the valence band maximum (VBM) in part B at

Γ in ABZ is small (a few hundreds of meV) to form a type-II band alignment of the hetero-structure [72–76], so that applying moiré potential can reverse the band ordering, as shown in Fig.1(c); and (2) the electronic states at Γ for the c-electrons in part A and f-electrons in part B should belong to different irreducible representations (irreps) of the crystal symmetry group for the heterostructure. For a small moiré potential in part B, we would expect the periodic bound states for f-electrons to form a trivial flat band. With increasing moiré potential strength, denoted as Δ_0 below, the trivial flat bands are pushed up in energy, and when the moiré potential strength Δ_0 is stronger than the type-II atomic band gap M of the heterostructure, we would expect the band ordering between the CBM of c-electrons and the moiré miniband of f-electrons from valence bands reverses at Γ , potentially leading to topological flat bands when the irreps of c- and f-electrons at Γ are different, as shown in Fig.1(e).

Below we will introduce a moiré Chern-band model to illustrate this general scheme for designing topological flat bands in Fig.1(a)-(e) and numerically demonstrate the emergence of topological flat bands in this model for two limits of the moiré superlattice potential: (1) the potential within the first-shell approximation and (2) the δ -function-like potential. Next, we will map the moiré

Chern-band model to the THF model and demonstrate that the exact topological flat band with "ideal quantum geometry" can be realized in this THF model by tuning the type-II atomic band gap M in Fig.1(c). We emphasize that this exact topological flat band is insensitive to the twist angle and can be achievable by tuning external gate voltages in experiments. Finally, we will discuss the potential material realization of this model in 2D moiré material heterojunctions and semiconductor heterostructures with superlattice potentials from patterned dielectric substrates. We exemplify 2D moiré material heterojunction with the type-II band alignment by $\text{Ti}_2\text{Se}_2/\text{Zn}_2\text{Te}_2$ with the moiré potential on the Ti_2Se_2 layer and show the existence of topological flat bands in this moiré heterojunction. We also provide a list of possible choices of two different 2D materials in this class of materials. More detailed calculations about realistic materials can be found in Supplementary Materials (SM) Sec.D[77].

II. MOIRÉ CHERN-BAND MODEL

We first introduce the Chern-band model under moiré superlattice potential, and its physical realization will be discussed in Sec.IV. The model Hamiltonian is given by [78, 79]

$$\hat{H}_{mC} = \hat{H}_C + \hat{H}_m. \quad (1)$$

\hat{H}_C describes a two-band effective model that allows for a non-zero Chern number and is given by [80–82]

$$\hat{H}_C = \sum_{\mathbf{k}\alpha\beta} a_{\alpha\mathbf{k}}^\dagger [H_C(\mathbf{k})]_{\alpha\beta} a_{\beta\mathbf{k}}$$

$$H_C(\mathbf{k}) = \begin{pmatrix} \epsilon(\mathbf{k}) + \mathcal{M}(\mathbf{k}) & Ak_+ \\ Ak_- & \epsilon(\mathbf{k}) - \mathcal{M}(\mathbf{k}) \end{pmatrix}, \quad (2)$$

where $a_{\alpha\mathbf{k}}$ ($a_{\alpha\mathbf{k}}^\dagger$) is the fermion annihilation (creation) operator with $\alpha = 1, 2$ indexing orbital basis, \mathbf{k} is the momentum expanded around Γ in the ABZ, $k_\pm = k_x \pm ik_y$, $\mathcal{M}(k) = M + Bk^2$, and $\epsilon(k) = Dk^2$. M, B, D, A are material dependent parameters, in which M and B govern the system's topology. Specifically, the system has Chern number $C = \pm 1$ when $MB < 0$, and $C = 0$ when $MB > 0$. H_C has continuous translation and rotation symmetries in the x-y plane. For our heterostructure setup in Fig.1(a), we would expect the $\alpha = 1$ orbital mainly contributes to the conduction band in part A while the $\alpha = 2$ orbital mainly gives the valence band in part B, forming the type-II band alignment in Fig.1(c). In the calculation below, we always choose $B, M > 0$ so that the Hamiltonian H_C is in the trivial insulator regime and furthermore choose $B, D > 0$ so that the valence band has a larger effective mass compared to the conduction band. The linear term Ak_\pm describes the interlayer coupling between the conduction band in part A and the valence band in part B. For the

material systems discussed in Sec.IV, we find its value around $\sim 0.72\text{eV} \cdot \text{\AA}$ for InAs/GaSb quantum wells and $\sim 1\text{eV} \cdot \text{\AA}$ for $\text{Ti}_2\text{Se}_2/\text{Zn}_2\text{Te}_2$ heterojunctions, which is several times smaller than the value $\sim 3.9\text{eV} \cdot \text{\AA}$ in HgTe quantum wells [83]. It should be noted that the above Hamiltonian \hat{H}_C breaks time reversal (TR) and thus it serves as the spin-up block in the full Hamiltonian for the nonmagnetic materials that respect TR symmetry, as discussed in Sec.IV, while the spin-down block can be related to \hat{H}_C by TR.

\hat{H}_m describes the moiré superlattice potential. To be concrete, we choose a hexagonal superlattice form described by the space group $P6/mmm$, leading to the $P6$ symmetry for \hat{H}_{mC} , which can be generated by six-fold rotation C_{6z} . Furthermore, we consider the diagonal term for the moiré potential,

$$\hat{H}_m = \sum_{\alpha=1,2} \int d^2\mathbf{r} a_{\alpha\mathbf{r}}^\dagger H_m^{\alpha\alpha}(\mathbf{r}) a_{\alpha\mathbf{r}}, \quad (3)$$

with $a_{\alpha\mathbf{r}} = \frac{1}{\sqrt{V}} \int d^2k a_{\alpha\mathbf{k}} e^{i\mathbf{k}\cdot\mathbf{r}}$, and $H_m^{\alpha\alpha}(\mathbf{r} + \mathbf{R}) = H_m^{\alpha\alpha}(\mathbf{r})$, where \mathbf{R} is the moiré superlattice vectors, given by $\mathbf{R} = n_1 \mathbf{a}_1^M + n_2 \mathbf{a}_2^M$ with $n_1, n_2 \in \mathcal{Z}$ and $\mathbf{a}_1^M = (1, 0)a_0^M$, $\mathbf{a}_2^M = (\frac{1}{2}, \frac{\sqrt{3}}{2})a_0^M$, where a_0^M is the moiré primitive lattice constant. We can expand the moiré potential in the moiré reciprocal lattice space as

$$H_m^{\alpha\alpha}(\mathbf{r}) = \sum_{\mathbf{g} \in \mathbf{G}_M} \Delta_\alpha(\mathbf{g}) e^{i\mathbf{g}\cdot\mathbf{r}} \quad (4)$$

and $\mathbf{G}_M = \{n_1 \mathbf{b}_1^M + n_2 \mathbf{b}_2^M | n_1, n_2 \in \mathcal{Z}\}$. Here, $\mathbf{b}_1^M = (2\pi, -\frac{2\pi}{\sqrt{3}}) \frac{1}{a_0^M}$ and $\mathbf{b}_2^M = (0, \frac{4\pi}{\sqrt{3}}) \frac{1}{a_0^M}$ label the primitive moiré reciprocal lattice vectors. We will consider two limits for $\Delta_\alpha(\mathbf{g})$ below.

A. First-Shell Potential Approximation

The first limit is to consider the first-shell potential approximation for the moiré potential, which has been successfully applied to the Bistritzer-MacDonald model of tBG [1, 84]. For our model, the first momentum shell includes six momenta, $\mathbf{G}_M^{\text{I}} = \{\mathbf{b}_2^M, \mathbf{b}_1^M, -\mathbf{b}_2^M, -\mathbf{b}_1^M, \mathbf{b}_2^M + \mathbf{b}_1^M, -\mathbf{b}_2^M - \mathbf{b}_1^M\}$, which can be connected by six-fold rotation symmetry C_{6z} around the z axis, and thus one parameter Δ_α for one α can characterize the moiré potential strength within the first-shell potential approximation. We further choose $\Delta_1 = 0$ and $\Delta_2(\mathbf{g}) = \Delta_0$ for $\mathbf{g} \in \mathbf{G}_M^{\text{I}}$ for the calculations below to describe the moiré potential only existing in the valence bands of part B, where Δ_0 represents the moiré potential strength. We note that the zero shell $\mathbf{g} = 0$ just corresponds to a constant energy shift, so it can be absorbed into the Fermi energy and atomic gap M . We choose the parameters for the valence band to possess a heavy effective mass compared to the conduction band, so we would expect the valence band will

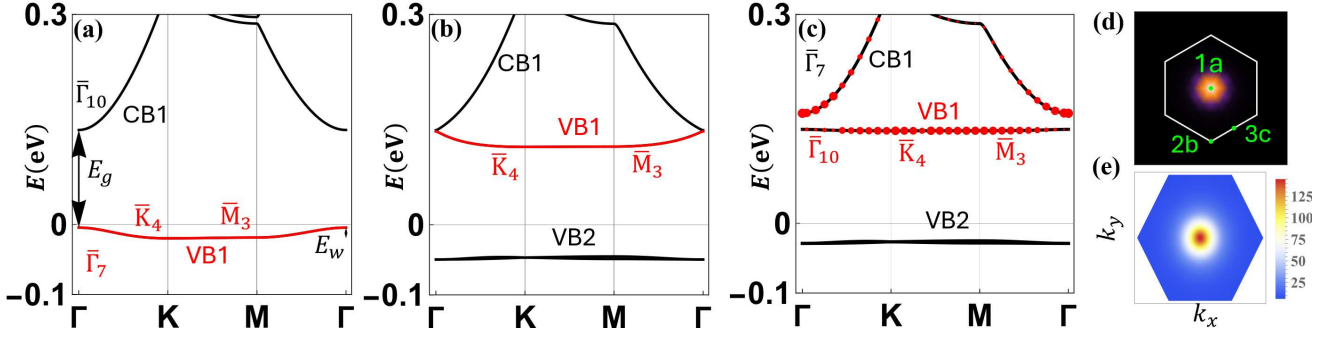


FIG. 2. (a)-(c) show the band dispersion for the parameters $M = 0.135\text{eV}$ and $\Delta_0 = 0.054\text{ eV}$, 0.089 eV and 0.094 eV , respectively, as denoted by the points (a)-(c) in the phase diagram of Fig.1(f). The band irreps of VB1 and CB1 are labeled in (a)-(c). In (c), the size of red dots in the VB1 and CB1 represents the overlap between the Bloch states and the Wannier orbital that is localized at the Wyckoff positions $1a$, as shown in (d). Three different Wyckoff positions are labeled by green dots in (d). (e) shows the Berry curvature distribution of VB1 in (c).

get localized by the moiré potential and thus focus on the highest valence mini-bands, denoted as VB1 below (see Fig.2(a)-(c)). We also choose $M > 0$ for which the atomic Hamiltonian \hat{H}_C is in the normal insulator regime.

Fig.1(f) reveals the mini-band flatness and topological phase diagram for the VB1 as a function of atomic band gap M and moiré potential strength Δ_0 . The color represents the ratio E_g/E_w , where E_g denotes the minimal mini-band gap between the VB1 and other mini-bands (mini-bands VB2 or CB1 labelled in Fig.2(b)), while E_w denotes the bandwidth of VB1. The bright color is for a large E_g/E_w , implying the occurrence of the flat VB1 mini-bands that are well separated in energy from VB2 and CB1. The white dashed lines label the mini-gap closing between the VB1 and other mini-bands, potentially corresponding to the topological phase transition of the VB1. The Chern number C of the VB1 is calculated and labeled in each insulating regime in Fig.1(f). We notice a striking bright line, as depicted by the red dashed line in Fig.1(f), in the $C = 1$ regime, which corresponds to topologically nontrivial flat mini-bands. To understand the formation of topological flat bands, we examine the band dispersion of the VB1 and the corresponding irreps of VB1 at high symmetry momenta (Γ , \mathbf{K} and \mathbf{M}) in Fig.2(a)-(c) for the parameter values marked by green crosses along the blue dashed line in Fig.1(f). The irreps of VB1 are calculated from the rotation eigenvalues of the eigen-wavefunctions of \hat{H}_{mC} (see SM Sec.B.1 [77]). For a small Δ_0 , the VB1 in Fig.2(c) is described by periodic localized orbitals from the valence band, which are confined by the maxima of moiré potential that correspond to the $1a$ Wyckoff position in the moiré unit cell, since our atomic model is in the normal insulator regime ($M > 0$). The irreps at high symmetry momenta of VB1, $(\bar{\Gamma}_7, \bar{K}_4, \bar{M}_3)$, coincide with the elementary band representation (EBR) ${}^2\bar{E}_1 \uparrow G(1)$ of the $P6$ group, which corresponds to the $J_z = 3/2$ orbital located at the $1a$ Wyckoff position, where J_z labels the out-of-plane total angular momentum (See Sec.B.2 in SM[77] for more details). The localized orbital plays the role of f-electron in

the THF model. With increasing Δ_0 , the VB1 is getting more localized and pushed up in energy, leading to a band inversion between the VB1 and CB1 at Γ point, as shown in Fig.2(b). After band inversion, the irreps at high symmetry momenta of VB1 are changed to $(\bar{\Gamma}_{10}, \bar{K}_4, \bar{M}_3)$, which is no longer an EBR. We directly evaluate the rotation eigenvalues of VB1 at high-symmetry momenta: C_{6z} eigenvalue $\eta(\Gamma) = e^{-i\frac{\pi}{6}}$ at Γ , three-fold rotation C_{3z} eigenvalue $\theta(\mathbf{K}) = -1$ at \mathbf{K} , and two-fold rotation C_{2z} eigenvalue $\epsilon(\mathbf{M}) = i$ at \mathbf{M} , respectively. Using the connection between the Chern number and rotation eigenvalues, $e^{iC\pi/3} = -\eta(\Gamma)\theta(\mathbf{K})\epsilon(\mathbf{M})$ [85], we find $C = 1 \pmod{6}$, which is consistent with the value from direct calculations in Fig.1(f). The red dots in the energy dispersion of Fig.2(c) represent the projection of localized Wannier functions for $J_z = 3/2$ orbitals, as shown in Fig.2(d). This Wannier orbital dominates the flat band VB1 away from Γ but forms the conduction band bottom of CB1 around Γ due to band inversion, and thus serves as the f-electron in the THF model discussed below. Fig.2(e) shows the Berry curvature distribution of VB1, which concentrates around Γ . Fig.1(f) and Fig.2 demonstrate the existence of topological flat bands of VB1 with concentrated Berry curvature for the moiré potential within the first-shell approximation.

We note that the topological flat band of VB1 is not limited to one point (c) in Fig.1(f), but exists along the whole red dashed line, as demonstrated in SM Sec.B.1[77]. Below we will provide a brief overview of the evolution of the VB1 along the red dashed line in Fig.1(f). As shown in Fig.S1 of SM, we find the VB1 moves from the conduction band bottom for a large Δ_0 and $M > 0$ to the valence band top for a small Δ_0 and $M < 0$, while the flatness and topological nature ($C = 1$) of VB1 remain along the red line in Fig.1(g). Along this line, the Berry curvature distribution of VB1 is changed. For a large Δ_0 , the Berry curvature is concentrated around Γ in Fig.2(e). When reducing Δ_0 along the red line in Fig.1(f), the Berry curvature becomes distributed across the entire mBZ (See Fig.S1 of SM[77]).

We note that the parameter regime for the topological flat bands with relatively uniform Berry curvature has been studied for the Hamiltonian \hat{H}_{mC} in Eq.(1) within the first-shell potential approximation in Refs.[78, 79]. Our work here focuses on different parameter regimes as compared to Refs.[78, 79]. There are two main differences: (1) the conduction and valence bands have the same absolute value of the effective mass in Ref.[78], which corresponds to $D = 0$ in Eq.(2); and (2) moiré potential exists for both the conduction and valence bands in Refs.[78, 79], which corresponds to $\Delta_1 = \Delta_2$ in Eq.(4). Consequently, both conduction and valence bands feel strong moiré potential and form moiré minibands, leading to a relatively uniform Berry curvature distribution in mBZ for topological flat bands. In our case, the small effective mass and the absence of moiré potential $\Delta_1 = 0$ for the conduction bands make the electrons in part A itinerant, thus providing c-electrons, while the large effective mass and strong moiré potential in part B induce periodic localized states from the valence bands, naturally leading to f-electrons. Thus, the topological flat band possesses concentrated Berry curvature distribution as shown in Fig.2(e), which can be described by the THF model in Sec.III and are thus in different parameter regimes from those with a relatively uniform Berry curvature distribution discussed in Refs.[78, 79].

B. Periodic δ -function-like Potential

The second limit is to consider the periodic δ -function-like moiré potential, which can more naturally illustrate our physical picture of topological flat bands with concentrated Berry curvature and allow for analytical expressions for the parameters of the THF model discussed in Sec.III A. The δ -function potential, described by

$$H_m^{\alpha\alpha}(\mathbf{r}) = \Delta_0 \Omega_0 \sum_{\mathbf{R}} \delta(\mathbf{r} - \mathbf{R}) \quad (5)$$

with $\alpha = 1, 2$, Δ_0 representing moiré potential and Ω_0 the moiré unit cell area, introduces uniform coupling between momentum states separated by moiré reciprocal lattice vectors $\mathbf{g} \in \mathbf{G}_M$ as its Fourier components retain equal amplitude for all \mathbf{g} s. It should be noted that we introduce δ -function potential into both the conduction and valence bands in Eq.(5) for the convenience of deriving the Green's function formalism below. When $\Delta_0 > 0$, we find the δ -function potential has little influence on the energy states around the conduction band bottom, as discussed in SM Sec.C.1[77]. Thus, we would expect introducing δ -potential with $\Delta_0 > 0$ for both conduction and valence bands in Eq.(5) will mainly give rise to the bound states of the valence band and have little influence on low-energy conduction bands. In the momentum space, the δ -function-like potential can be written as

$$\hat{H}_m = \Delta_0 \sum_{\mathbf{k}\alpha} \sum_{\mathbf{g}, \mathbf{g}'} a_{\alpha, \mathbf{k}+\mathbf{g}}^\dagger a_{\alpha, \mathbf{k}+\mathbf{g}'}, \quad (6)$$

in the second quantization form, where \mathbf{k} is chosen within the first mBZ, \mathbf{g}, \mathbf{g}' are for any moiré reciprocal lattice vector, $\mathbf{g}, \mathbf{g}' \in \mathbf{G}_M$. We note that δ -function potential couples a state at the momentum $\mathbf{k}+\mathbf{g}$ to a state at $\mathbf{k}+\mathbf{g}'$ with an equal strength Δ_0 for any values of \mathbf{g}, \mathbf{g}' , and this long-range coupling in momentum space will lead to the divergence of the bound state energy under ideal 2D δ -function potential (See SM Sec.C.1[77]). Therefore, we introduce a momentum cutoff G_Λ , $|\mathbf{g}|, |\mathbf{g}'| \leq |G_\Lambda|$, for the \mathbf{g}, \mathbf{g}' summations in the moiré reciprocal space for Eq.(6).

This problem for the δ -function-like potential can be solved using the Green's function formalism[86], which is discussed in SM Sec.B.2[77]. In the momentum space, the full Hamiltonian with the δ -function-like moiré potential can be written as

$$H_{mC}(\mathbf{k}) = H_0(\mathbf{k}) + N_g \Delta_0 P_0 \quad (7)$$

where $H_0(\mathbf{k})$ is a block diagonal matrix given by

$$H_0(\mathbf{k}) = \begin{pmatrix} H_C(\mathbf{k} + \mathbf{g}_1) & 0 & \dots & 0 \\ 0 & H_C(\mathbf{k} + \mathbf{g}_2) & \dots & 0 \\ \vdots & \vdots & \ddots & \vdots \\ 0 & 0 & \dots & H_C(\mathbf{k} + \mathbf{g}_{N_g}) \end{pmatrix}.$$

\mathbf{g}_j is the moiré reciprocal lattice vectors within the momentum cut-off G_Λ ($j = 1, 2, \dots, N_g$), and $P_0 = |\phi_0\rangle \langle \phi_0| \otimes \sigma_0$ is the projection operator with $|\phi_0\rangle = \frac{1}{\sqrt{N_g}} [1, 1, \dots, 1]^T$ and σ_0 is the 2-by-2 identity matrix. For this Hamiltonian, the trace of the Green's function, $G = (E1_{2N_g \times 2N_g} - H_{mC}(\mathbf{k}))^{-1}$, can be derived as (See SM Sec.C.2[77])

$$\text{Tr}(G) = \text{Tr}_\sigma(\mathbf{g}(\mathbf{k}, E)) + \text{Tr}_\sigma \left(\Delta_0 \sum_j \mathbf{g}^0(\mathbf{k} + \mathbf{g}_j, E) \frac{1}{\sigma_0 - \Delta_0 \mathbf{g}(\mathbf{k}, E)} \mathbf{g}^0(\mathbf{k} + \mathbf{g}_j, E) \right), \quad (8)$$

where Tr_σ means the trace over 2-by-2 σ matrix on the orbital basis $\alpha = 1, 2$, $\mathbf{g}^0(\mathbf{k} + \mathbf{g}_j, E) = (E\sigma_0 - H_C(\mathbf{k} + \mathbf{g}_j))^{-1}$ is the free Green's function of H_C and $\mathbf{g}(\mathbf{k}, E) = \sum_j \mathbf{g}^0(\mathbf{k} + \mathbf{g}_j, E)$. The poles of $\text{Tr}(G)$ determine the energy spectrum of H_{mC} (denoted as $\mathcal{E}_n(\mathbf{k})$ below). For any eigen-energy $E_\eta(\mathbf{k} + \mathbf{g}_j)$ of $H_C(\mathbf{k} + \mathbf{g}_j)$, one can prove the limit $\lim_{E \rightarrow E_\eta(\mathbf{k} + \mathbf{g}_j)} \text{Tr}(G) \approx -\frac{1}{\Delta_0}$ (See SM Sec.C.2 [77]). Therefore, the eigen-energy of $H_C(\mathbf{k} + \mathbf{g}_j)$ for any j is *not* the pole of $\text{Tr}(G)$. From Eq.(8), the poles of $\text{Tr}(G)$ can only come from $\frac{1}{\sigma_0 - \Delta_0 \mathbf{g}(\mathbf{k}, E)}$ and thus the eigen-energy spectrum $\mathcal{E}_n(\mathbf{k})$ of H_{mC} is determined by

$$\text{Det}(\sigma_0 - \Delta_0 \mathbf{g}(\mathbf{k}, \mathcal{E}_n(\mathbf{k}))) = 0. \quad (9)$$

The spectrum function $\mathcal{A}(\mathbf{k}, E) = -\Im(\text{Tr}(G))/\pi$ is numerically calculated from Eq.(8) and depicted in Fig.3(a) and (b), where \Im denotes the imaginary part. In Fig.3(a)

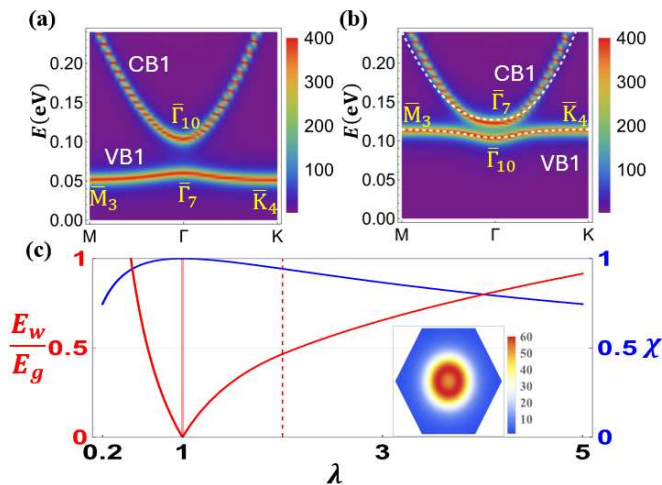


FIG. 3. (a) and (b) show the energy spectra before and after band inversion for moiré Chern-band model with periodic δ -function-like potential. The potential strength Δ_0 is 3.85meV and 4.05meV, respectively. In panel (b), the white dashed line represents the dispersion obtained from the THF model. (c) E_w/E_g and $\chi = \frac{\int \Omega(\mathbf{k}) d\mathbf{k}}{\int \text{Tr}(g(\mathbf{k})) d\mathbf{k}}$ as a function of λ . When $\lambda = \frac{\Delta E \alpha}{\beta^2} = 1$, $\frac{\Omega_{xy}(\mathbf{k})}{\text{Tr}(g(\mathbf{k}))} = 1$ for every \mathbf{k} and $E_w/E_g = 0$. For the parameters of the THF fitting to the band dispersion in (b), we find $\lambda = 2.01$ indicated by the red dashed line. The insert shows the Berry curvature distribution of topological flat band.

for a small Δ_0 , we find a flat band, denoted as VB1, which is originated from the valence band and is extremely localized at the $1a$ Wyckoff position by the δ -function-like potential (see Fig.S9 in SM Sec.C.2[77]). Using the perturbation theory (SM Sec.C.2[77]), we can analytically solve the binding energy of VB1, given by

$$E_0 = -M - \frac{A^2}{2B} + \frac{(B-D)G_\Lambda^2}{e^{\frac{\Omega_B(B-D)}{\Delta_0\pi}} - 1} \quad (10)$$

where $\Omega_B = \frac{8\pi^2}{\sqrt{3}(a_0^M)^2}$ is the area of mBZ. The binding energy in Eq.(10) diverges with G_Λ^2 and fits well with the full numerical calculations for a large G_Λ (See Fig.S10 of SM[77]). With further increasing the moiré potential Δ_0 in Fig.3(b), the band inversion between VB1 and CB1 around Γ leads to the emergence of topological flat mini-band. We also directly calculate the irreps for VB1 at high symmetry momenta, e.g. Γ , \mathbf{K} and \mathbf{M} , in Fig.3(a) and (b), which coincide with those in Fig.2(a) and (c). This is because the potential maximum appears at the $1a$ Wyckoff position in moiré unit cell, and the trivial flat band from the valence band can be regarded as localized $J_z = 3/2$ orbitals at the $1a$ Wyckoff position for both cases of moiré potential. Based on the studies of both the first-shell approximation and δ -function-like potential, we conclude the physical picture shown in Fig.1 can be generally applied and the topological flat band of VB1 can emerge (Fig.2(c) and Fig.3(b)) once the moiré potential strength Δ_0 is larger than the atomic band gap M ,

irregardless of the detailed moiré potential form and the twist angle, which only determines the length scale of the moiré unit cell.

III. THE THF MODEL

A. Mapping to THF model

The band inversion for moiré Chern-band model with either the first-shell approximation or periodic δ -function-like potential can be captured by a THF model with the form

$$\hat{H}_{HF}^0 = \sum_{|\mathbf{k}| < \Lambda_c} \left[\alpha \mathbf{k}^2 c_{\mathbf{k}}^\dagger c_{\mathbf{k}} + \Delta E f_{\mathbf{k}}^\dagger f_{\mathbf{k}} + (\beta k_+ c_{\mathbf{k}}^\dagger f_{\mathbf{k}} + h.c.) \right], \quad (11)$$

where $k_\pm = k_x \pm ik_y$, the annihilation operator $c_{\mathbf{k}}$ is for c-electrons of CB1 while $f_{\mathbf{k}}$ is for f-electrons of VB1. The parameters $\alpha, \Delta E, \beta$ can be extracted from the moiré Chern-band model in Eq.(1) for both types of moiré potentials. Particularly, the expressions for the relation between $\alpha, \Delta E, \beta$ in the THF model and Chern-band model parameters such as M and Δ_0 can be derived analytically for the periodic δ -function-like potential, as shown below in Eq.(12). The α term describes the dispersion of c-electrons, the ΔE term describes the energy difference between the c-electron and f-electron at Γ , and the β term describes the hybridization between c-electron and f-electron. We have set the energy of the conduction band bottom to be zero. The full THF model should also include the interaction terms $\hat{H}_{HF} = \hat{H}_{HF}^0 + \hat{H}_{int}$ with \hat{H}_{int} describing the screened Coulomb interaction previously derived in Ref. [64]. We focus on the derivation of \hat{H}_{HF}^0 in this section.

For the first-shell potential approximation of moiré potential, the mapping to the THF model can be constructed via the maximally localized Wannier function method [87, 88], as detailed in SM Sec.B.2[77]. To do that, we first construct the maximally localized Wannier function $|W_{\mathbf{R}}^{(1)}\rangle$ for $J_z = 3/2$ orbital at the $1a$ position, as shown in Fig.2(d), and its projection to the VB1 and CB1 is shown by the sizes of red dots in Fig.2(c). We also consider the wavefunction of the conduction band bottom at Γ , denoted as $|\phi_{1,\mathbf{k}=0}\rangle$, and project the full Hamiltonian $\hat{H}_{mC}(\mathbf{k})$ into the subspace spanned by $|W_{\mathbf{R}}^{(1)}\rangle$ and $|\phi_{1,\mathbf{k}=0}\rangle$, leading to the THF model \hat{H}_{HF}^0 in Eq.(11) with the parameters $\alpha, \beta, \Delta E$ extracted numerically in Eq.(S.B17) of SM Sec.B.2 [77].

A similar procedure can be applied to the periodic δ -function-like moiré potential to map the moiré Chern-band model to the THF model. Due to the simplicity of periodic δ -function-like potential, we can solve all the parameters in the THF model via the Löwdin perturbation

theory [89], given by

$$\alpha = B + D; \Delta E = \mathcal{E}_0 - M - \Delta_0; \beta = \frac{AN_v}{\mathcal{E}_0 + M}, \quad (12)$$

where N_v is a normalization factor of the localized f-electron wavefunction $f_0^\dagger |0\rangle$ and \mathcal{E}_0 is the binding energy in Eq.(10). More details for the derivations of these parameters can be found in SM Sec.C.3[77]. We emphasize that ΔE depends on both M and Δ_0 , so it can be tuned by an external gate voltage experimentally. In Fig.3(b), the white dashed lines are calculated from the THF model in Eq.(11) with the parameters directly extracted from the perturbation theory in Eq.(12), and the dispersion fits well with the full numerical calculations for CB1 and VB1. The momentum-space Berry curvature distribution of the topological flat band in Fig.3(b) is calculated for the THF model and plotted in the inset of Fig.3(c), which is concentrated around Γ and similar to the result shown in Fig.2(e).

B. Topological Flat Band with Ideal Quantum Geometry in THF model

The THF Hamiltonian \hat{H}_{HF}^0 in Eq.(11) can possess an exact flat band with "ideal quantum geometry" when the condition $\Delta E = \beta^2/\alpha$ is satisfied. To see that, we introduce the mode operator

$$\gamma_{1,\mathbf{k}}^\dagger = (c_{\mathbf{k}}^\dagger \ f_{\mathbf{k}}^\dagger)u_{1,\mathbf{k}}; \quad u_{1,\mathbf{k}} = \sqrt{\frac{1}{\alpha E_{\mathbf{k}}}} \begin{pmatrix} \alpha k_+ \\ \beta \end{pmatrix} \quad (13)$$

so that the Hamiltonian (11) becomes

$$\hat{H}_{HF}^0 = \sum_{|\mathbf{k}| < \Lambda_c} \left[E_{\mathbf{k}} \gamma_{1,\mathbf{k}}^\dagger \gamma_{1,\mathbf{k}} + (\Delta E - \frac{\beta^2}{\alpha}) f_{\mathbf{k}}^\dagger f_{\mathbf{k}} \right], \quad (14)$$

where $E_{\mathbf{k}} = \alpha k^2 + \frac{\beta^2}{\alpha}$. When $\Delta E = \frac{\beta^2}{\alpha}$, the second term in Eq.(14) vanishes so \hat{H}_{HF}^0 only depends on a single mode operator $\gamma_{1,\mathbf{k}}^\dagger$, but not on the other mode

$$\gamma_{0,\mathbf{k}}^\dagger = (c_{\mathbf{k}}^\dagger \ f_{\mathbf{k}}^\dagger)u_{0,\mathbf{k}}; \quad u_{0,\mathbf{k}} = \sqrt{\frac{1}{\alpha E_{\mathbf{k}}}} \begin{pmatrix} -\beta \\ \alpha k_- \end{pmatrix} \quad (15)$$

which is orthogonal to $\gamma_{1,\mathbf{k}}^\dagger$. Thus, the solution of Eq.(15) corresponds to an exact flat band with zero energy (See Fig.1(e)). Since the eigen-wavefunction in Eq.(15) only contains k_- except a normalization factor, this exact flat band realizes "ideal quantum geometry" (See SM Sec.B.3[77])

$$Tr(g) = \Omega_{xy} = \frac{2\alpha^2\beta^2}{(\beta^2 + \alpha^2k^2)^2}, \quad (16)$$

where $\Omega_{xy} = -2Im(\langle \partial_{k_x} u_{0,\mathbf{k}} | \partial_{k_y} u_{0,\mathbf{k}} \rangle)$ is the Berry curvature and $g_{ij} = Re(\langle \partial_{k_i} u_{0,\mathbf{k}} | \partial_{k_j} u_{0,\mathbf{k}} \rangle - \langle \partial_{k_i} u_{0,\mathbf{k}} | u_{0,\mathbf{k}} \rangle \langle u_{0,\mathbf{k}} | \partial_{k_j} u_{0,\mathbf{k}} \rangle)$

($i, j = x, y$) is the Fubini-Study metric tensor of the flat band [90]. We notice that ΔE describes the energy difference between c-electrons and f-electrons at Γ and is related to the atomic band gap M in Eq.(12), which can be controlled by an external gate voltage (See Fig.1(a)). When tuning the dimensionless parameter $\lambda = \Delta E \frac{\alpha}{\beta^2}$ away from 1, the bandwidth of the flat band increases and the ratio $\chi = \frac{\int \Omega_{xy}(\mathbf{k}) d\mathbf{k}}{\int Tr(g(\mathbf{k})) d\mathbf{k}}$ departs from the ideal quantum geometry ($\chi = 1$), as shown in Fig. 3(c). The energy separation between the exact flat band ($\gamma_{0,\mathbf{k}}$) and the dispersive band ($\gamma_{1,\mathbf{k}}$) is $\Delta E = \frac{\beta^2}{\alpha}$ at Γ . We estimate $\Delta E \approx 40\text{meV}$ with $\beta \approx 0.2 \text{ nm}\cdot\text{eV}$ and $\alpha \approx 1 \text{ nm}^2\cdot\text{eV}$. Therefore, depending on the energy order of the Coulomb interaction energy U , our system is in the projected regime for $U \ll \Delta E$ and in the heavy fermion regime when $U > \Delta E$ [64].

IV. MATERIAL REALIZATION

A. Semiconductor hetero-structures

The model Hamiltonian (2) can appear as one spin block in the Bernevig-Hughes-Zhang (BHZ) model [91] when there is spin $U(1)$ symmetry or out-of-plane mirror symmetry, as discussed in SM Sec.A.1 [77], which was originally applied to HgTe/CdTe [91–93], InAs/GaSb quantum wells [94, 95], topological insulator films of (Bi,Sb)₂(Te,Se)₃ compounds [96, 97] and Dirac semimetal Cd₂As₃ thin films [79, 98]. We would expect two degenerate topological flat bands with opposite spin appearing in the BHZ model with moiré potential, and these two bands are related to each other by TR symmetry and carry non-trivial Z_2 topological invariant. We note that the inverted band ordering at the atomic level is *not* necessary, since topological flat bands can occur in the regime of $M > 0$. Therefore, the narrow gap semiconductor heterostructures, such as InAs/AlSb, InSb/InSe or PbTe/PbSnTe [99–101], are also potential candidates. The superlattice potential in semiconductor heterostructures can be achieved by patterning dielectric substrates or via a nearby moiré superlattice layer, which has been discussed in the literature [102–105]. In SM Sec.B.1 and C.2 [77], we use the moiré BHZ model with the material parameters for the HgTe/CdTe quantum wells as a model system for demonstration.

B. 2D material hetero-structure with Γ -valley

The existing 2D material databases [106–110] allow for a systematic search of 2D materials for type-II heterostructures with a narrow atomic band gap. We search for two 2D materials, denoted as Material 1 and Material 2, to form a heterostructure based on the following criteria: (1) type-II band alignment between two 2D materials; (2) the location of the CBM of Material 1 and

VBM of Material 2 at Γ in the ABZ; (3) different irreps for CBM in Material 1 and VBM in Material 2 at Γ [111, 112]; (4) the band gap between CBM in Material 1 and VBM in Material 2 smaller than 0.5 eV; and (5) the lattice mismatch smaller than 15%. Based on these criteria, a list of possible 2D material heterostructures with the symmetry groups $p\bar{3}m1$ is shown in Table SIII of SM Sec.D [77].

Next we will show that the low-energy physics of the heterostructures in Table SIII of SM [77] can be related to the BHZ model under moiré potentials with additional off-diagonal terms. Here we take $\text{Ti}_2\text{Se}_2/\text{Zn}_2\text{Te}_2$ heterostructure as an example with both material compounds belonging to the space group $p\bar{3}m1$ with the wave-vector group of D_{3d} at Γ . We will study this heterostructure in three steps. In the first step, we will calculate the electronic band structures and band irreps at Γ for individual Ti_2Se_2 and Zn_2Te_2 , as well as the $\text{Ti}_2\text{Se}_2/\text{Zn}_2\text{Te}_2$ heterostructure with a matched lattice constant, using the density function theory (DFT) calculations [111, 112] (Fig.4(a), (b) and (c)). Here we relax the lattice constant of Ti_2Se_2 to match that of Zn_2Te_2 , so that there is no moiré pattern formed between Ti_2Se_2 and Zn_2Te_2 in this step for the DFT calculations. In the second step, we will build a four-band effective model to reproduce the electronic band structures of $\text{Ti}_2\text{Se}_2/\text{Zn}_2\text{Te}_2$ heterostructure within the energy range between -0.1eV and 0.1eV (inset in Fig.4(c)). In the last step, we introduce a moiré potential into the Ti_2Se_2 layer using the four-band effective model within the first-shell potential approximation and treat the parameters of moiré potential as tuning parameters to identify the regime for the existence of topological flat bands in this system (Fig.4(f) and (g)).

We start from the band structures for individual Ti_2Se_2 and Zn_2Te_2 without spin-orbit coupling (SOC). The conduction band of Ti_2Se_2 has a lower energy than that of Zn_2Te_2 , while the valence band of Zn_2Te_2 has a higher energy than that of Ti_2Se_2 , thus forming a type-II band alignment for $\text{Ti}_2\text{Se}_2/\text{Zn}_2\text{Te}_2$ heterostructure. According to Table SIII of SM [77], the conduction band of Ti_2Se_2 belongs to 1D irrep Γ_2^- with the z-directional orbital angular momentum $L_z = 0$, while the valence band of Zn_2Te_2 belongs to 2D irrep Γ_3^- with the $L_z = \pm 1$. The difference in orbital angular momentum $\Delta L_z = \pm 1$ implies the linear- k coupling between the conduction and valence bands. The atomic band gap between the CBM of Ti_2Se_2 and the VBM of Zn_2Te_2 is around 0.2 eV without SOC, which is in the suitable energy range to form a narrow gap heterostructure. It should be noted that the inversion symmetry in D_{3d} is broken when Ti_2Se_2 and Zn_2Te_2 form a heterostructure, so that the wave-vector group D_{3d} is reduced to C_{3v} , and the corresponding irreps Γ_2^- for CBM and Γ_3^- for VBM at Γ are reduced to Γ_1 with orbital angular momentum $L_z = 0$ and Γ_3 with $L_z = \pm 1$, respectively, according to the character tables for the D_{3d} and C_{3v} groups shown in Table SIV of Sec.D.2 in SM [77]. Based on the Γ_1 and Γ_3 irreps for

the conduction and valence bands, we can construct the effective Hamiltonian without SOC as

$$H_0(\mathbf{k}) = \begin{pmatrix} E_1 + A_1 k^2 & iB_0 k_+ & iB_0 k_- \\ -iB_0 k_- & E_2 + A_2 k^2 & 0 \\ -iB_0 k_+ & 0 & E_2 + A_2 k^2 \end{pmatrix} \quad (17)$$

on the basis $\{|\Gamma_1, L = 0\rangle, |\Gamma_3, L = +1\rangle, |\Gamma_3, L = -1\rangle\}$, where E_1, E_2, A_1, A_2, B_0 are material-dependent parameters. $H_0(\mathbf{k})$ takes the same form for spin up and spin down basis.

We next consider the influence of SOC on the electronic band structure using DFT calculations. With SOC, the spin degeneracy for the $L_z = 0$ orbital remains and forms the $J_z = \pm \frac{1}{2}$ state, where J_z is the z-directional total angular momentum including orbital angular momentum and spin, while the $L_z = \pm 1$ orbitals are split into the $J_z = \pm \frac{3}{2}$ and $J_z = \pm \frac{1}{2}$ states. According to the character table of the D_{3d} group (Table SIV in SM [77]), the 1D irrep Γ_2^- becomes the 2D irrep $\bar{\Gamma}_4^-$, while the 2D irrep Γ_3^- splits into two 2D irreps, $\bar{\Gamma}_4^-$ and $\bar{\Gamma}_5^- \bar{\Gamma}_6^-$. Thus, we expect the CBM of Ti_2Se_2 to belong to $\bar{\Gamma}_4^-$ ($J_z = \pm \frac{1}{2}$), while the VBM of Zn_2Te_2 belongs to either $\bar{\Gamma}_4^-$ ($J_z = \pm \frac{1}{2}$) or $\bar{\Gamma}_5^- \bar{\Gamma}_6^-$ ($J_z = \pm \frac{3}{2}$), depending on the sign of SOC in Zn_2Te_2 . Fig.4(a) and (b) show the band structure of Ti_2Se_2 and Zn_2Te_2 with SOC, respectively, from the DFT calculations. One finds that the VBM of Zn_2Te_2 belongs to $\bar{\Gamma}_5^- \bar{\Gamma}_6^-$ irrep with $J_z = \pm \frac{3}{2}$. The electronic band structure of $\text{Ti}_2\text{Se}_2/\text{Zn}_2\text{Te}_2$ heterostructure, in which the lattice constant of Ti_2Se_2 has been relaxed to match that of Zn_2Te_2 (no moiré pattern), is calculated in Fig.4(c) with red and blue colors representing the projections of the bands into the Ti_2Se_2 and Zn_2Te_2 layers, respectively. One can see the conduction band is from the Ti_2Se_2 layer and the topmost valence band around Γ is from the Zn_2Te_2 layer. Furthermore, the inset of Fig.4(c) shows the zoom-in of the band dispersion around Γ (within the black rectangle box) within the energy range between -0.2eV and 0.2eV with the band irreps at Γ . We find the CBM at Γ belongs to $\bar{\Gamma}_4^-$ irrep ($J_z = \pm \frac{1}{2}$) while the VBM belongs to $\bar{\Gamma}_5^- \bar{\Gamma}_6^-$ irrep ($J_z = \pm \frac{3}{2}$), consistent with the above symmetry analysis for the positive Δ_{SOC} case (see SM Sec.D2 [77]). Based on the symmetry property, the \mathbf{k} -independent SOC term has the form

$$H_{SOC}^s = \begin{pmatrix} 0 & 0 & 0 \\ 0 & s\Delta_{SOC} & 0 \\ 0 & 0 & -s\Delta_{SOC} \end{pmatrix}, \quad (18)$$

within one layer, where we choose $s = +$ and $-$ for spin up \uparrow and spin down \downarrow , respectively, and Δ_{SOC} labels the SOC strength.

Since both the Hamiltonian H_0 and H_{SOC} are block diagonal in the spin basis, we may only consider the spin-up block with a 3-by-3 Hamiltonian

$$H_{3b,\uparrow} = H_0(\mathbf{k}) + H_{SOC}^+ \quad (19)$$

on the basis wavefunctions $|\Gamma_1, J_z = \frac{1}{2}, \uparrow\rangle, |\Gamma_3, J_z = \frac{3}{2}, \uparrow\rangle$ and $|\Gamma_3, J_z = -\frac{1}{2}, \uparrow\rangle$, which provide one conduction

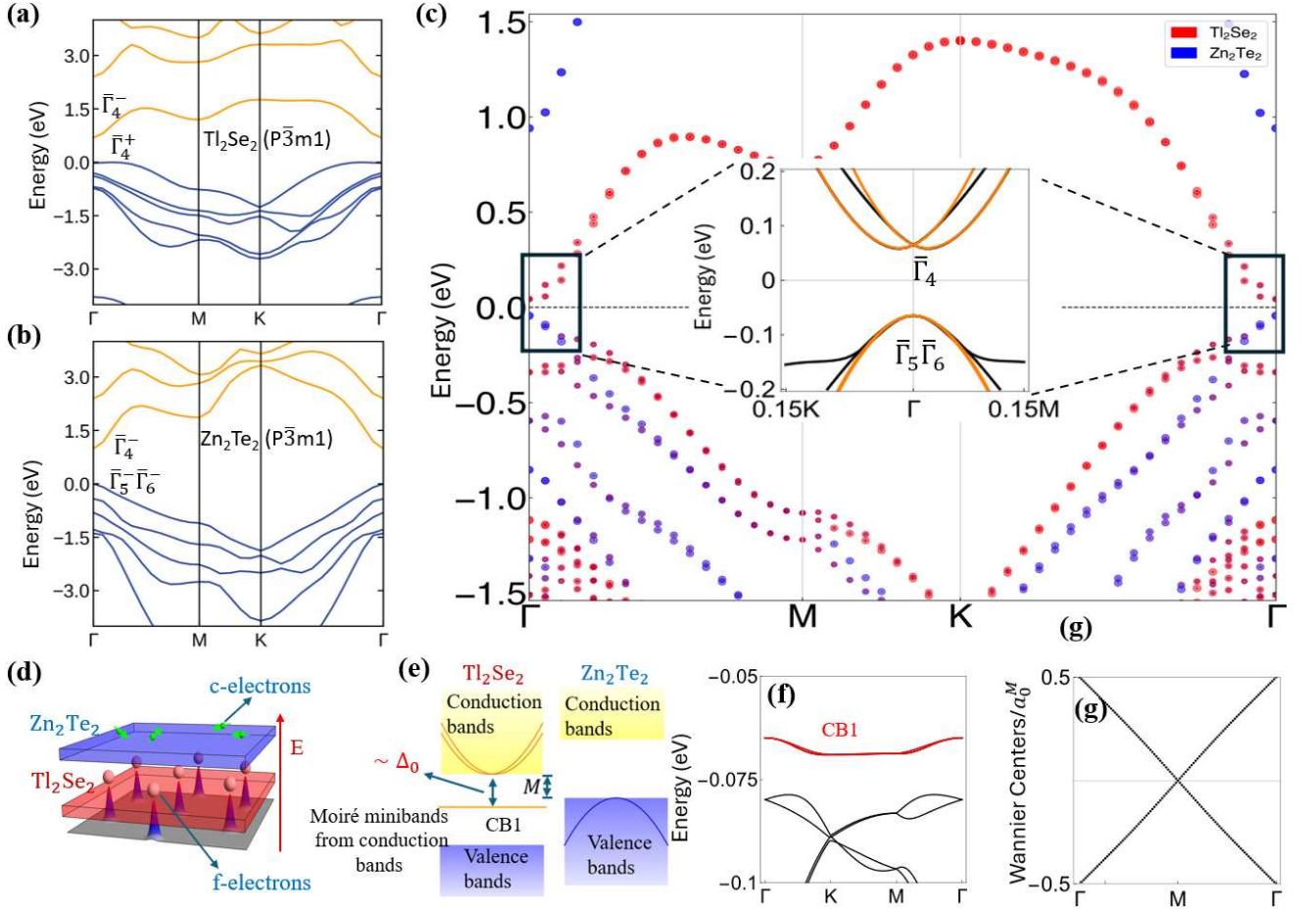


FIG. 4. (a) and (b) show band dispersions near Fermi energy for monolayer Tl_2Se_2 and Zn_2Te_2 , individually. The irreps of conduction band bottom and valence band top at Γ are labeled in the plot for both compounds. (c) The band dispersion of $\text{Tl}_2\text{Se}_2/\text{Zn}_2\text{Te}_2$ heterostructure without moiré forms a type-II band alignment. The sizes of red and blue dots represent the projections to the Tl_2Se_2 and Zn_2Te_2 layers. The inset of (c) presents a zoomed-in view of the band dispersion near Γ point from DFT calculation (black curves) and the corresponding effective model fitting (orange curves). (d) Schematics for $\text{Tl}_2\text{Se}_2/\text{Zn}_2\text{Te}_2$ heterostructure with moiré potential applied to Tl_2Se_2 layer. (e) Schematics of type-II band alignment. The conduction and valence bands originate from Tl_2Se_2 and Zn_2Te_2 , respectively. (f) The band dispersion of $\text{Tl}_2\text{Se}_2/\text{Zn}_2\text{Te}_2$ heterostructure with moiré potential on Tl_2Se_2 layer. Topological flat bands, labelled by CB1, are highlighted in red color. (g) The Wannier centers flow of CB1 with a winding feature demonstrate non-trivial Z_2 number of CB1.

band and two valence bands. The topmost valence band has the $|\Gamma_3, J_z = \frac{3}{2}, \uparrow\rangle$ character for $\Delta_{SOC} > 0$ and the $|\Gamma_3, J_z = -\frac{1}{2}, \uparrow\rangle$ character for $\Delta_{SOC} < 0$. As shown in SM Sec.D.2 [77], projecting the Hamiltonian $H_{3b,\uparrow}$ into the subspace of the conduction and topmost valence bands always leads to the Chern-band model H_C in Eq.(2), no matter the sign of Δ_{SOC} , although the basis wavefunctions depend on the sign of Δ_{SOC} . In $\text{Tl}_2\text{Se}_2/\text{Zn}_2\text{Te}_2$ hetero-structure, our DFT calculations show $\Delta_{SOC} > 0$, so that the topmost valence band is from $|\Gamma_3, J_z = \frac{3}{2}, \uparrow\rangle$ and the $|\Gamma_3, J_z = -\frac{1}{2}, \uparrow\rangle$ state should be projected out. After projecting out this state by perturbation theory, we find $H_{3b,\uparrow}$ is reduced to $H_{hetero}^{\uparrow\uparrow}(\mathbf{k})$, given by

$$H_{hetero}^{\uparrow\uparrow}(\mathbf{k}) = \begin{pmatrix} E_1 + \tilde{A}_1 k^2 & iB_0 k_+ \\ -iB_0 k_- & \tilde{E}_2 + A_2 k^2 \end{pmatrix}, \quad (20)$$

on the basis wavefunctions $|\Gamma_1, J_z = \frac{1}{2}, \uparrow\rangle$, and $|\Gamma_3, J_z = \frac{3}{2}, \uparrow\rangle$, where $\tilde{A}_1 = A_1 + \frac{B_0^2}{E_1 - E_2 + \Delta_{SOC}}$, $\tilde{E}_2 = E_2 + \Delta_{SOC}$ and other parameters remain the same as those in Eq.(17). The TR partner of $H_{hetero}^{\uparrow\uparrow}(\mathbf{k})$ is denoted as $H_{hetero}^{\downarrow\downarrow}(\mathbf{k})$, given by

$$H_{hetero}^{\downarrow\downarrow}(\mathbf{k}) = (H_{hetero}^{\uparrow\uparrow}(-\mathbf{k}))^*, \quad (21)$$

on the basis wavefunctions $|\Gamma_1, J_z = -\frac{1}{2}, \downarrow\rangle$, and $|\Gamma_3, J_z = -\frac{3}{2}, \downarrow\rangle$.

For the $\text{Tl}_2\text{Se}_2/\text{Zn}_2\text{Te}_2$ heterostructure, the conduction band from the Tl_2Se_2 layer shows a strong Rashba-type of spin splitting (see the inset of Fig.4(c)). Thus, an additional \mathbf{k} -dependent SOC term should be included

in the effective model, and the full Hamiltonian reads

$$H_{hetero}(\mathbf{k}) = \begin{pmatrix} H_{hetero}^{\uparrow\uparrow}(\mathbf{k}) & H_{hetero}^{\uparrow\downarrow}(\mathbf{k}) \\ (H_{hetero}^{\uparrow\downarrow}(\mathbf{k}))^\dagger & H_{hetero}^{\downarrow\downarrow}(\mathbf{k}) \end{pmatrix}, \quad (22)$$

where $H_{hetero}^{\uparrow\uparrow}(\mathbf{k})$ and $H_{hetero}^{\downarrow\downarrow}(\mathbf{k})$ are the spin up and down blocks given in Eqs.(20) and (21), respectively. $H_{hetero}^{\uparrow\downarrow}(\mathbf{k})$ takes the form of the Rashba-type of SOC for the conduction band and is given by

$$H_{hetero}^{\uparrow\downarrow}(\mathbf{k}) = \begin{pmatrix} -iRk_- & 0 \\ 0 & 0 \end{pmatrix}. \quad (23)$$

By choosing the parameters $E_1 = -\tilde{E}_2 = 0.0649$ eV, $\tilde{A}_1 = 16.874 \text{ \AA}^2 \cdot \text{eV}$, $A_2 = -16.80 \text{ \AA}^2 \cdot \text{eV}$, $B_0 = 0.909 \text{ \AA} \cdot \text{eV}$ and $R = 0.727 \text{ \AA} \cdot \text{eV}$, we find the band dispersion depicted by the orange lines from the Hamiltonian in Eq.(22) fits well with that depicted by the black lines from the DFT calculations within the energy range between -0.1eV and 0.1eV in the inset of Fig.4(c). It should be noted that the atomic band gap of the $\text{Tl}_2\text{Se}_2/\text{Zn}_2\text{Te}_2$ heterostructure (without moiré potential) is around ~ 0.13 eV, which is smaller than the energy difference $\sim 0.2\text{eV}$ between the CBM of Tl_2Se_2 and the VBM of Zn_2Te_2 (without SOC), shown in Table SIII of SM Sec.D.2[77], because the DFT calculation of band structure of the $\text{Tl}_2\text{Se}_2/\text{Zn}_2\text{Te}_2$ heterostructure include SOC and charge transfer between two layers and tend to reduce the energy gap.

After establishing the atomic Hamiltonian in Eq.(22) for the heterostructure, we next consider the moiré potential, which can be introduced into either Zn_2Te_2 layer or Tl_2Se_2 layer. As the Rashba SOC exists only for the conduction band in the Tl_2Se_2 layer, but not in the Zn_2Te_2 layer, it is different for the moiré potential occurring in the Tl_2Se_2 or Zn_2Te_2 layers. We consider two different configurations for moiré potential. The first configuration is to introduce moiré potential to the Zn_2Te_2 layer, which localizes the valence band and pushes the topmost valence mini-band, denoted as VB1, to higher energy and leads to band inversion with the conduction band in the Tl_2Se_2 layer. However, we find that due to the strong Rashba SOC in the conduction band of the Tl_2Se_2 layer, the VB1 becomes highly dispersive in the topologically non-trivial regime, as discussed in detail in SM Sec.D.3 [77].

The second configuration is to introduce moiré superlattice potential into the conduction band in the Tl_2Se_2 layer instead, as shown in Fig.4(d). This configuration can be described by the Hamiltonian

$$\hat{H} = \hat{H}_{hetero} + \hat{H}_m, \quad (24)$$

where

$$\hat{H}_{hetero} = \sum_{\mathbf{k}\alpha\beta} a_{\alpha\mathbf{k}}^\dagger [H_{hetero}(\mathbf{k})]_{\alpha\beta} a_{\beta\mathbf{k}}, \quad (25)$$

with $H_{hetero}(\mathbf{k})$ given in Eq.(22) and the basis index $\alpha, \beta = 1, 2, 3, 4$, and the moiré potential at the Tl_2Se_2

layer is given by

$$\hat{H}_m = \sum_{\alpha} \int d^2r a_{\alpha\mathbf{r}}^\dagger H_m^{\alpha\alpha}(\mathbf{r}) a_{\alpha\mathbf{r}}, \quad (26)$$

with the first shell approximation, $H_m^{\alpha\alpha}(\mathbf{r}) = \sum_{g \in \mathbf{G}_M^1} \Delta_0 e^{i\mathbf{g} \cdot \mathbf{r}} (\delta_{\alpha,1} + \delta_{\alpha,3})$. One should note that $\alpha = 1, 3$ is for the conduction bands in Tl_2Se_2 layer and $\alpha = 2, 4$ for the valence bands in Zn_2Te_2 layer, and thus the moiré potential only exists at the Tl_2Se_2 layer. The moiré potential can confine the conduction band into the localized states and decrease the energy of the lowest conduction mini-bands, denoted as CB1 in Fig.4(e). We note that the confining potential quenches the influence of SOC on CB1 and the spin splitting of CB1 is reduced for a strong moiré potential strength Δ_0 . When a strong Δ_0 leads to a band inversion between CB1 and the valence band in the Zn_2Te_2 layer, the CB1 becomes topologically non-trivial. As shown in Fig.4(f) and (g), the CB1 is found to be quite flat with the band width smaller than 10 meV and has negligible spin splitting, while the winding in the Wannier center flow reveals its non-trivial band topology. In addition, for a given moiré potential strength Δ_0 , the phase transition can be tuned by the atomic gap M via external gate voltages (See Fig.S12 in Sec.D.3 of SM [77]). It should be noted that the moiré potential can be achieved by interfacing Tl_2Se_2 with another large gap insulating layer to form a hetero-bilayer or by twisting two Tl_2Se_2 layers. The heterostructure formed by twisted Tl_2Se_2 homobilayer and Zn_2Te_2 monolayer is studied in SM Sec.D.4 [77].

V. CONCLUSION AND DISCUSSION

In this work, we propose a general scheme to realize the THF model with topological flat bands using 2D moiré heterostructures with type-II band alignment. The ability to continuously tune the atomic band gap M via external gate voltages will allow us to systematically explore different regimes of the THF model discussed in Ref.[64]. The exact flat band with "ideal quantum geometry" was first theoretically discussed for the tractable "chiral" limit of the tBG model [8, 13], in analog to the Laughlin wavefunctions of the fractional quantum Hall effect, for the realization of fractional Chern insulator phases. However, the chiral limit requires zero tunneling of the AA sites in the tBG model, while the ratio of the tunneling between the AA sites and AB/BA sites in realistic tBG is around $0.7 \sim 0.8$ [60, 61], far away from the chiral limit. Our design principle of the "ideal" THF model is achievable for a variety of 2D material heterojunctions and semiconductor hetero-structures, as exemplified by our model studies of $\text{Tl}_2\text{Se}_2/\text{Zn}_2\text{Te}_2$ moiré heterojunction, and HgTe/CdTe quantum wells with patterned dielectric substrates (Sec.B, C and D in SM [77]). A systematic search of 2D material hetero-structures with type-II band alignment is beyond the scope of this

work. Although we focused on the materials with their low-energy bands around Γ in the ABZ, this scheme of forming heterostructures with type-II band alignment is also possible for other 2D materials with low-energy bands around other high symmetry momenta, such as TMD [113–115]. We note that heavy fermion physics has recently been revealed in TMD moiré systems, $\text{MoTe}_2/\text{WSe}_2$ [116], while its potential topological property [117] remains unexplored in experiments. The "ideal" topological flat band found in our THF model makes our proposed platform appealing for exploring interacting topological physics such as fractional Chern insulator phase [55], topological Kondo physics [116–121], as well as superconductivity [12, 64, 67, 122–124]. Narrow gap heterostructures with type-II band alignment also provide a platform to explore the physics of exciton insulators and exciton condensate [36, 125–127].

VI. ACKNOWLEDGMENT

We would like to acknowledge Xi Dai, Zhida Song, Jie Wang, Shuolong Yang, Jiabin Yu and Jun Zhu for the

helpful discussion. Y.L. and C.L. acknowledge the support from the Penn State Materials Research Science and Engineering Center for Nanoscale Science under National Science Foundation award DMR-2011839. B.A.B. acknowledges the support by the Gordon and Betty Moore Foundation through Grant No. GBMF8685 towards the Princeton theory program, the Gordon and Betty Moore Foundation's EPiQS Initiative (Grant No. GBMF11070), the Office of Naval Research (ONR Grant No. N00014-20-1-2303), the Global Collaborative Network Grant at Princeton University, the Simons Investigator (Grant No. 404513), the NSF-MERSEC (Grant No. MERSEC DMR 2011750), the Simons Collaboration on New Frontiers in Superconductivity, and the Schmidt Foundation at the Princeton University. H. H. was also supported by the Gordon and Betty Moore Foundation through Grant No. GBMF8685 towards the Princeton theory program, the Gordon and Betty Moore Foundation's EPiQS Initiative (Grant No. GBMF11070), Simons Collaboration on New Frontiers in Superconductivity at the Princeton University (Grant no. SFI-MPS-NFS-00006741-01). A.A., Z.F., and Q.Y. are supported by the U.S. National Science Foundation under grant No. DMR-2323469.

-
- [1] R. Bistritzer and A. H. MacDonald, Moiré bands in twisted double-layer graphene, *Proceedings of the National Academy of Sciences* **108**, 12233 (2011).
 - [2] Y. Cao, V. Fatemi, S. Fang, K. Watanabe, T. Taniguchi, E. Kaxiras, and P. Jarillo-Herrero, Unconventional superconductivity in magic-angle graphene superlattices, *Nature* **556**, 43 (2018).
 - [3] X. Lu, P. Stepanov, W. Yang, M. Xie, M. A. Aamir, I. Das, C. Urgell, K. Watanabe, T. Taniguchi, G. Zhang, *et al.*, Superconductors, orbital magnets and correlated states in magic-angle bilayer graphene, *Nature* **574**, 653 (2019).
 - [4] Y. Xie, A. T. Pierce, J. M. Park, D. E. Parker, E. Khalaf, P. Ledwith, Y. Cao, S. H. Lee, S. Chen, P. R. Forrester, *et al.*, Fractional chern insulators in magic-angle twisted bilayer graphene, *Nature* **600**, 439 (2021).
 - [5] Y. Cao, V. Fatemi, A. Demir, S. Fang, S. L. Tomarken, J. Y. Luo, J. D. Sanchez-Yamagishi, K. Watanabe, T. Taniguchi, E. Kaxiras, *et al.*, Correlated insulator behaviour at half-filling in magic-angle graphene superlattices, *Nature* **556**, 80 (2018).
 - [6] S. Lisi, X. Lu, T. Benschop, T. A. de Jong, P. Stepanov, J. R. Duran, F. Margot, I. Cucchi, E. Cappelli, A. Hunter, *et al.*, Observation of flat bands in twisted bilayer graphene, *Nature Physics* **17**, 189 (2021).
 - [7] R. Pons, A. Mielke, and T. Stauber, Flat-band ferromagnetism in twisted bilayer graphene, *Physical Review B* **102**, 235101 (2020).
 - [8] G. Tarnopolsky, A. J. Kruchkov, and A. Vishwanath, Origin of magic angles in twisted bilayer graphene, *Physical review letters* **122**, 106405 (2019).
 - [9] M. Serlin, C. Tschirhart, H. Polshyn, Y. Zhang, J. Zhu, K. Watanabe, T. Taniguchi, L. Balents, and A. Young, Intrinsic quantized anomalous hall effect in a moiré heterostructure, *Science* **367**, 900 (2020).
 - [10] Y.-H. Zhang, D. Mao, and T. Senthil, Twisted bilayer graphene aligned with hexagonal boron nitride: Anomalous hall effect and a lattice model, *Physical Review Research* **1**, 033126 (2019).
 - [11] N. Bultinck, S. Chatterjee, and M. P. Zaletel, Mechanism for anomalous hall ferromagnetism in twisted bilayer graphene, *Physical review letters* **124**, 166601 (2020).
 - [12] Z.-D. Song and B. A. Bernevig, Magic-angle twisted bilayer graphene as a topological heavy fermion problem, *Physical review letters* **129**, 047601 (2022).
 - [13] P. J. Ledwith, G. Tarnopolsky, E. Khalaf, and A. Vishwanath, Fractional chern insulator states in twisted bilayer graphene: An analytical approach, *Physical Review Research* **2**, 023237 (2020).
 - [14] C. Repellin and T. Senthil, Chern bands of twisted bilayer graphene: Fractional chern insulators and spin phase transition, *Physical Review Research* **2**, 023238 (2020).
 - [15] M. Oh, K. P. Nuckolls, D. Wong, R. L. Lee, X. Liu, K. Watanabe, T. Taniguchi, and A. Yazdani, Evidence for unconventional superconductivity in twisted bilayer graphene, *Nature* **600**, 240 (2021).
 - [16] E. Y. Andrei and A. H. MacDonald, Graphene bilayers with a twist, *Nature materials* **19**, 1265 (2020).
 - [17] T. Ohta, J. T. Robinson, P. J. Feibelman, A. Bostwick, E. Rotenberg, and T. E. Beechem, Evidence for interlayer coupling and moiré periodic potentials in twisted bilayer graphene, *Physical Review Letters* **109**, 186807 (2012).
 - [18] Y. Xie, B. Lian, B. Jäck, X. Liu, C.-L. Chiu, K. Watanabe, T. Taniguchi, B. A. Bernevig, and A. Yazdani, Spectroscopic signatures of many-body correlations in

- magic-angle twisted bilayer graphene, *Nature* **572**, 101 (2019).
- [19] F. Wu, T. Lovorn, E. Tutuc, and A. H. MacDonald, Hubbard model physics in transition metal dichalcogenide moiré bands, *Physical review letters* **121**, 026402 (2018).
- [20] H. Pan, F. Wu, and S. Das Sarma, Band topology, hubbard model, heisenberg model, and dzyaloshinskii-moriya interaction in twisted bilayer wse₂, *Physical Review Research* **2**, 033087 (2020).
- [21] Y. Xu, K. Kang, K. Watanabe, T. Taniguchi, K. F. Mak, and J. Shan, A tunable bilayer hubbard model in twisted wse₂, *Nature nanotechnology* **17**, 934 (2022).
- [22] K. F. Mak and J. Shan, Semiconductor moiré materials, *Nature Nanotechnology* **17**, 686 (2022).
- [23] F. Wu, T. Lovorn, E. Tutuc, I. Martin, and A. MacDonald, Topological insulators in twisted transition metal dichalcogenide homobilayers, *Physical review letters* **122**, 086402 (2019).
- [24] E. C. Regan, D. Wang, E. Y. Paik, Y. Zeng, L. Zhang, J. Zhu, A. H. MacDonald, H. Deng, and F. Wang, Emerging exciton physics in transition metal dichalcogenide heterobilayers, *Nature Reviews Materials* **7**, 778 (2022).
- [25] Z. Zhang, Y. Wang, K. Watanabe, T. Taniguchi, K. Ueno, E. Tutuc, and B. J. LeRoy, Flat bands in twisted bilayer transition metal dichalcogenides, *Nature Physics* **16**, 1093 (2020).
- [26] T. Devakul, V. Crépel, Y. Zhang, and L. Fu, Magic in twisted transition metal dichalcogenide bilayers, *Nature communications* **12**, 6730 (2021).
- [27] J. Cai, E. Anderson, C. Wang, X. Zhang, X. Liu, W. Holtzmann, Y. Zhang, F. Fan, T. Taniguchi, K. Watanabe, *et al.*, Signatures of fractional quantum anomalous hall states in twisted mote₂, *Nature* **622**, 63 (2023).
- [28] Y. Zeng, Z. Xia, K. Kang, J. Zhu, P. Knüppel, C. Vaswani, K. Watanabe, T. Taniguchi, K. F. Mak, and J. Shan, Thermodynamic evidence of fractional chern insulator in moiré mote₂, *Nature* **622**, 69 (2023).
- [29] F. Xu, Z. Sun, T. Jia, C. Liu, C. Xu, C. Li, Y. Gu, K. Watanabe, T. Taniguchi, B. Tong, *et al.*, Observation of integer and fractional quantum anomalous hall effects in twisted bilayer mote₂, *Physical Review X* **13**, 031037 (2023).
- [30] Y. Xia, Z. Han, K. Watanabe, T. Taniguchi, J. Shan, and K. F. Mak, Superconductivity in twisted bilayer wse₂, *Nature* **637**, 833 (2025).
- [31] N. Morales-Durán, N. Wei, J. Shi, and A. H. MacDonald, Magic angles and fractional chern insulators in twisted homobilayer transition metal dichalcogenides, *Physical Review Letters* **132**, 096602 (2024).
- [32] B. Tang, B. Che, M. Xu, Z. P. Ang, J. Di, H.-J. Gao, H. Yang, J. Zhou, and Z. Liu, Recent advances in synthesis and study of 2d twisted transition metal dichalcogenide bilayers, *Small Structures* **2**, 2000153 (2021).
- [33] K. Liu, L. Zhang, T. Cao, C. Jin, D. Qiu, Q. Zhou, A. Zettl, P. Yang, S. G. Louie, and F. Wang, Evolution of interlayer coupling in twisted molybdenum disulfide bilayers, *Nature communications* **5**, 4966 (2014).
- [34] L. Zhang, Z. Zhang, F. Wu, D. Wang, R. Gogna, S. Hou, K. Watanabe, T. Taniguchi, K. Kulkarni, T. Kuo, *et al.*, Twist-angle dependence of moiré excitons in ws₂/mose₂ heterobilayers, *Nature communications* **11**, 5888 (2020).
- [35] Y. Tang, L. Li, T. Li, Y. Xu, S. Liu, K. Barmak, K. Watanabe, T. Taniguchi, A. H. MacDonald, J. Shan, *et al.*, Simulation of hubbard model physics in wse₂/ws₂ moiré superlattices, *Nature* **579**, 353 (2020).
- [36] Y. Xu, S. Liu, D. A. Rhodes, K. Watanabe, T. Taniguchi, J. Hone, V. Elser, K. F. Mak, and J. Shan, Correlated insulating states at fractional fillings of moiré superlattices, *Nature* **587**, 214 (2020).
- [37] E. Marcellina, X. Liu, Z. Hu, A. Fieramosca, Y. Huang, W. Du, S. Liu, J. Zhao, K. Watanabe, T. Taniguchi, *et al.*, Evidence for moiré trions in twisted mose₂ homobilayers, *Nano Letters* **21**, 4461 (2021).
- [38] P. C. Adak, S. Sinha, A. Agarwal, and M. M. Deshmukh, Tunable moiré materials for probing berry physics and topology, *Nature Reviews Materials* **9**, 481 (2024).
- [39] K. P. Nuckolls and A. Yazdani, A microscopic perspective on moiré materials, *Nature Reviews Materials* **9**, 460 (2024).
- [40] E. Y. Andrei, D. K. Efetov, P. Jarillo-Herrero, A. H. MacDonald, K. F. Mak, T. Senthil, E. Tutuc, A. Yazdani, and A. F. Young, The marvels of moiré materials, *Nature Reviews Materials* **6**, 201 (2021).
- [41] A. Nimbalkar and H. Kim, Opportunities and challenges in twisted bilayer graphene: a review, *Nano-Micro Letters* **12**, 1 (2020).
- [42] S. Carr, S. Fang, and E. Kaxiras, Electronic-structure methods for twisted moiré layers, *Nature Reviews Materials* **5**, 748 (2020).
- [43] P. Törmä, S. Peotta, and B. A. Bernevig, Superconductivity, superfluidity and quantum geometry in twisted multilayer systems, *Nature Reviews Physics* **4**, 528 (2022).
- [44] Z. Song, Z. Wang, W. Shi, G. Li, C. Fang, and B. A. Bernevig, All magic angles in twisted bilayer graphene are topological, *Physical review letters* **123**, 036401 (2019).
- [45] Z.-D. Song, B. Lian, N. Regnault, and B. A. Bernevig, Twisted bilayer graphene. ii. stable symmetry anomaly, *Physical Review B* **103**, 205412 (2021).
- [46] H. C. Po, L. Zou, T. Senthil, and A. Vishwanath, Faithful tight-binding models and fragile topology of magic-angle bilayer graphene, *Physical Review B* **99**, 195455 (2019).
- [47] J. Ahn, S. Park, and B.-J. Yang, Failure of nielsen-ninomiya theorem and fragile topology in two-dimensional systems with space-time inversion symmetry: application to twisted bilayer graphene at magic angle, *Physical Review X* **9**, 021013 (2019).
- [48] J. Yu, B. A. Bernevig, R. Queiroz, E. Rossi, P. Törmä, and B.-J. Yang, Quantum geometry in quantum materials, *arXiv preprint arXiv:2501.00098* (2024).
- [49] T. Liu, X.-B. Qiang, H.-Z. Lu, and X. Xie, Quantum geometry in condensed matter, *National Science Review* **12**, nwae334 (2025).
- [50] P. Törmä, Essay: Where can quantum geometry lead us?, *Physical Review Letters* **131**, 240001 (2023).
- [51] L. Ju, A. H. MacDonald, K. F. Mak, J. Shan, and X. Xu, The fractional quantum anomalous hall effect, *Nature Reviews Materials* **9**, 455 (2024).
- [52] K. Sun, Z. Gu, H. Katsura, and S. Das Sarma, Nearly flatbands with nontrivial topology, *Physical review letters* **106**, 236803 (2011).

- [53] N. Regnault and B. A. Bernevig, Fractional chern insulator, *Physical Review X* **1**, 021014 (2011).
- [54] E. Tang, J.-W. Mei, and X.-G. Wen, High-temperature fractional quantum hall states, *Physical review letters* **106**, 236802 (2011).
- [55] J. Wang, J. Cano, A. J. Millis, Z. Liu, and B. Yang, Exact landau level description of geometry and interaction in a flatband, *Physical review letters* **127**, 246403 (2021).
- [56] J. Wang, S. Klevtsov, and Z. Liu, Origin of model fractional chern insulators in all topological ideal flatbands: Explicit color-entangled wave function and exact density algebra, *Physical Review Research* **5**, 023167 (2023).
- [57] P. J. Ledwith, A. Vishwanath, and D. E. Parker, Vortexability: A unifying criterion for ideal fractional chern insulators, *Physical Review B* **108**, 205144 (2023).
- [58] R. Roy, Band geometry of fractional topological insulators, *Physical Review B* **90**, 165139 (2014).
- [59] J. Wang and Z. Liu, Hierarchy of ideal flatbands in chiral twisted multilayer graphene models, *Physical Review Letters* **128**, 176403 (2022).
- [60] M. Koshino, N. F. Yuan, T. Koretsune, M. Ochi, K. Kuroki, and L. Fu, Maximally localized wannier orbitals and the extended hubbard model for twisted bilayer graphene, *Physical Review X* **8**, 031087 (2018).
- [61] S. Carr, S. Fang, Z. Zhu, and E. Kaxiras, Exact continuum model for low-energy electronic states of twisted bilayer graphene, *Physical Review Research* **1**, 013001 (2019).
- [62] D. Călugăru, M. Borovkov, L. L. Lau, P. Coleman, Z.-D. Song, and B. A. Bernevig, Twisted bilayer graphene as topological heavy fermion: Ii. analytical approximations of the model parameters, *Low Temperature Physics* **49**, 640 (2023).
- [63] H. Shi and X. Dai, Heavy-fermion representation for twisted bilayer graphene systems, *Physical Review B* **106**, 245129 (2022).
- [64] J. Herzog-Arbeitman, J. Yu, D. Călugăru, H. Hu, N. Regnault, C. Liu, O. Vafek, P. Coleman, A. Tsvelik, Z.-d. Song, *et al.*, Topological heavy fermion principle for flat (narrow) bands with concentrated quantum geometry, arXiv preprint arXiv:2404.07253 (2024).
- [65] L. L. Lau and P. Coleman, Topological mixed valence model for twisted bilayer graphene, *Physical Review X* **15**, 021028 (2025).
- [66] D. Călugăru, H. Hu, R. L. Merino, N. Regnault, D. K. Efetov, and B. A. Bernevig, The thermoelectric effect and its natural heavy fermion explanation in twisted bilayer and trilayer graphene, arXiv preprint arXiv:2402.14057 (2024).
- [67] C.-X. Liu, Y. Chen, A. Yazdani, and B. A. Bernevig, Electron–k-phonon interaction in twisted bilayer graphene, *Physical Review B* **110**, 045133 (2024).
- [68] Y.-J. Wang, G.-D. Zhou, B. Lian, and Z.-D. Song, Electron-phonon coupling in the topological heavy fermion model of twisted bilayer graphene, *Physical Review B* **111**, 035110 (2025).
- [69] J. Herzog-Arbeitman, J. Yu, D. Călugăru, H. Hu, N. Regnault, O. Vafek, J. Kang, and B. A. Bernevig, Heavy fermions as an efficient representation of atomistic strain and relaxation in twisted bilayer graphene, arXiv preprint arXiv:2405.13880 (2024).
- [70] H. Hu, Z.-D. Song, and B. A. Bernevig, Projected and solvable topological heavy fermion model of twisted bilayer graphene, arXiv preprint arXiv:2502.14039 (2025).
- [71] J. Yu, M. Xie, B. A. Bernevig, and S. Das Sarma, Magic-angle twisted symmetric trilayer graphene as a topological heavy-fermion problem, *Physical Review B* **108**, 035129 (2023).
- [72] A. Belabbes, C. Panse, J. Furthmüller, and F. Bechstedt, Electronic bands of iii-v semiconductor polytypes and their alignment, *Physical Review B—Condensed Matter and Materials Physics* **86**, 075208 (2012).
- [73] V. O. Özçelik, J. G. Azadani, C. Yang, S. J. Koester, and T. Low, Band alignment of two-dimensional semiconductors for designing heterostructures with momentum space matching, *Physical Review B* **94**, 035125 (2016).
- [74] J. Q. Ng, Q. Wu, L. Ang, and Y. S. Ang, Tunable electronic properties and band alignments of mosi2n4/gan and mosi2n4/zno van der waals heterostructures, *Applied Physics Letters* **120** (2022).
- [75] S. S. Lo, T. Mirkovic, C.-H. Chuang, C. Burda, and G. D. Scholes, Emergent properties resulting from type-ii band alignment in semiconductor nanoheterostructures, *Advanced Materials* **23**, 180 (2011).
- [76] X. Hong, J. Kim, S.-F. Shi, Y. Zhang, C. Jin, Y. Sun, S. Tongay, J. Wu, Y. Zhang, and F. Wang, Ultrafast charge transfer in atomically thin mos2/ws2 heterostructures, *Nature nanotechnology* **9**, 682 (2014).
- [77] Supplementary materials for "topological heavy fermion model in two-dimensional moiré heterostructures with type-ii band alignment", .
- [78] T. Tan, A. P. Reddy, L. Fu, and T. Devakul, Designing topology and fractionalization in narrow gap semiconductor films via electrostatic engineering, *Physical Review Letters* **133**, 206601 (2024).
- [79] W. Miao, A. Rashidi, and X. Dai, Artificial moiré engineering for an ideal bernevig-hughes-zhang model, *Physical Review B* **111**, 045113 (2025).
- [80] X.-L. Qi, Y.-S. Wu, and S.-C. Zhang, Topological quantization of the spin hall effect in two-dimensional paramagnetic semiconductors, *Physical Review B—Condensed Matter and Materials Physics* **74**, 085308 (2006).
- [81] X.-L. Qi and S.-C. Zhang, Topological insulators and superconductors, *Reviews of modern physics* **83**, 1057 (2011).
- [82] C.-Z. Chang, C.-X. Liu, and A. H. MacDonald, Colloquium: Quantum anomalous hall effect, *Reviews of Modern Physics* **95**, 011002 (2023).
- [83] C. Liu and S. Zhang, Chapter 3 - models and materials for topological insulators, in *Topological Insulators*, Contemporary Concepts of Condensed Matter Science, Vol. 6, edited by M. Franz and L. Molenkamp (Elsevier, 2013) pp. 59–89.
- [84] B. A. Bernevig, Z.-D. Song, N. Regnault, and B. Lian, Twisted bilayer graphene. i. matrix elements, approximations, perturbation theory, and ak·p two-band model, *Physical Review B* **103**, 205411 (2021).
- [85] C. Fang, M. J. Gilbert, and B. A. Bernevig, Bulk topological invariants in noninteracting point group symmetric insulators, *Physical Review B—Condensed Matter and Materials Physics* **86**, 115112 (2012).

- [86] G. D. Mahan, *Many-particle physics* (Springer Science & Business Media, 2013).
- [87] N. Marzari, A. A. Mostofi, J. R. Yates, I. Souza, and D. Vanderbilt, Maximally localized wannier functions: Theory and applications, *Reviews of Modern Physics* **84**, 1419 (2012).
- [88] I. Souza, N. Marzari, and D. Vanderbilt, Maximally localized wannier functions for entangled energy bands, *Physical Review B* **65**, 035109 (2001).
- [89] R. Winkler, *Spin-orbit coupling effects in two-dimensional electron and hole systems*, Vol. 191 (Springer, 2003).
- [90] D. C. Brody and L. P. Hughston, Geometric quantum mechanics, *Journal of geometry and physics* **38**, 19 (2001).
- [91] B. A. Bernevig, T. L. Hughes, and S.-C. Zhang, Quantum spin hall effect and topological phase transition in hgte quantum wells, *science* **314**, 1757 (2006).
- [92] M. König, S. Wiedmann, C. Brune, A. Roth, H. Buhmann, L. W. Molenkamp, X.-L. Qi, and S.-C. Zhang, Quantum spin hall insulator state in hgte quantum wells, *Science* **318**, 766 (2007).
- [93] M. König, H. Buhmann, L. W. Molenkamp, T. Hughes, C.-X. Liu, X.-L. Qi, and S.-C. Zhang, The quantum spin hall effect: theory and experiment, *Journal of the Physical Society of Japan* **77**, 031007 (2008).
- [94] C. Liu, T. L. Hughes, X.-L. Qi, K. Wang, and S.-C. Zhang, Quantum spin hall effect in inverted type-ii semiconductors, *Physical review letters* **100**, 236601 (2008).
- [95] I. Knez, R.-R. Du, and G. Sullivan, Evidence for helical edge modes in inverted inas/gasb quantum wells, *Physical review letters* **107**, 136603 (2011).
- [96] C.-X. Liu, X.-L. Qi, H. Zhang, X. Dai, Z. Fang, and S.-C. Zhang, Model hamiltonian for topological insulators, *Physical Review B—Condensed Matter and Materials Physics* **82**, 045122 (2010).
- [97] C.-X. Liu, H. Zhang, B. Yan, X.-L. Qi, T. Frauenheim, X. Dai, Z. Fang, and S.-C. Zhang, Oscillatory crossover from two-dimensional to three-dimensional topological insulators, *Physical Review B—Condensed Matter and Materials Physics* **81**, 041307 (2010).
- [98] A. Rashidi, S. Ahadi, S. Munyan, W. J. Mitchell, and S. Stemmer, Tuning displacement fields in a two-dimensional topological insulator using nanopatterned gates, *Nano Letters* **24**, 7366 (2024).
- [99] H. Kroemer, The 6.1 a family (inas, gasb, alsb) and its heterostructures: a selective review, *Physica E: Low-dimensional Systems and Nanostructures* **20**, 196 (2004).
- [100] Z. Wang, F. Sun, J. Liu, Y. Tian, Z. Zhang, Y. Zhang, X. Wei, T. Guo, J. Fan, L. Ni, *et al.*, Electric field and uniaxial strain tunable electronic properties of the insb/inse heterostructure, *Physical Chemistry Chemical Physics* **22**, 20712 (2020).
- [101] R. Buczko and L. Cywiński, Pbte/pbsnte heterostructures as analogs of topological insulators, *Physical Review B—Condensed Matter and Materials Physics* **85**, 205319 (2012).
- [102] C. Forsythe, X. Zhou, K. Watanabe, T. Taniguchi, A. Pasupathy, P. Moon, M. Koshino, P. Kim, and C. R. Dean, Band structure engineering of 2d materials using patterned dielectric superlattices, *Nature nanotechnology* **13**, 566 (2018).
- [103] J. H. Hinnefeld, S. T. Gill, and N. Mason, Graphene transport mediated by micropatterned substrates, *Applied Physics Letters* **112** (2018).
- [104] M. Jamalzadeh, Z. Zhang, Z. Huang, M. Manzo-Perez, K. Kisslinger, T. Taniguchi, K. Watanabe, P. Moon, G. S. Doerk, and D. Shahrjerdi, Synthetic band structure engineering of graphene using block copolymer-templated dielectric superlattices, *ACS nano* **19**, 9885 (2025).
- [105] Z. Zhan, Y. Li, and P. A. Pantaleón, Designing band structures by patterned dielectric superlattices, *Physical Review B* **111**, 045148 (2025).
- [106] N. Mounet, M. Gibertini, P. Schwaller, D. Campi, A. Merkys, A. Marrazzo, T. Sohier, I. E. Castelli, A. Cepellotti, G. Pizzi, *et al.*, Two-dimensional materials from high-throughput computational exfoliation of experimentally known compounds, *Nature nanotechnology* **13**, 246 (2018).
- [107] D. Campi, N. Mounet, M. Gibertini, G. Pizzi, and N. Marzari, Expansion of the materials cloud 2d database, *ACS nano* **17**, 11268 (2023).
- [108] S. Hastrup, M. Strange, M. Pandey, T. Deilmann, P. S. Schmidt, N. F. Hinsche, M. N. Gjerding, D. Torelli, P. M. Larsen, A. C. Riis-Jensen, *et al.*, The computational 2d materials database: high-throughput modeling and discovery of atomically thin crystals, *2D Materials* **5**, 042002 (2018).
- [109] U. Petralanda, Y. Jiang, B. A. Bernevig, N. Regnault, and L. Elcoro, Two-dimensional topological quantum chemistry and catalog of topological materials, *arXiv preprint arXiv:2411.08950* (2024).
- [110] Y. Jiang, U. Petralanda, G. Skorupskii, Q. Xu, H. Pi, D. Călugăru, H. Hu, J. Xie, R. A. Mustaf, P. Höhn, *et al.*, 2d theoretically twistable material database, *arXiv preprint arXiv:2411.09741* (2024).
- [111] J. Gao, Q. Wu, C. Persson, and Z. Wang, Irvsp: To obtain irreducible representations of electronic states in the vasp, *Computer Physics Communications* **261**, 107760 (2021).
- [112] M. Iraola, J. L. Mañes, B. Bradlyn, M. K. Horton, T. Neupert, M. G. Vergniory, and S. S. Tsirkin, Irrep: symmetry eigenvalues and irreducible representations of ab initio band structures, *Computer Physics Communications* **272**, 108226 (2022).
- [113] Q. Tong, H. Yu, Q. Zhu, Y. Wang, X. Xu, and W. Yao, Topological mosaics in moiré superlattices of van der waals heterobilayers, *Nature Physics* **13**, 356 (2017).
- [114] Q. Zhu, M. W.-Y. Tu, Q. Tong, and W. Yao, Gate tuning from exciton superfluid to quantum anomalous hall in van der waals heterobilayer, *Science advances* **5**, eaau6120 (2019).
- [115] H. Zhang, W. Xu, Y. Xiao, F. M. Peeters, and M. V. Milošević, Electronic band structure of high-symmetry homobilayers of transition metal dichalcogenides, *Physical Review B* **110**, 115410 (2024).
- [116] W. Zhao, B. Shen, Z. Tao, Z. Han, K. Kang, K. Watanabe, T. Taniguchi, K. F. Mak, and J. Shan, Gate-tunable heavy fermions in a moiré kondo lattice, *Nature* **616**, 61 (2023).
- [117] D. Guerci, K. P. Lucht, V. Crépel, J. Cano, J. Pixley, and A. Millis, Topological kondo semimetal and insulator in ab-stacked heterobilayer transition metal dichalcogenides, *Physical Review B* **110**, 165128 (2024).

- [118] M. Dzero, J. Xia, V. Galitski, and P. Coleman, Topological kondo insulators, *Annual Review of Condensed Matter Physics* **7**, 249 (2016).
- [119] M. Dzero, K. Sun, V. Galitski, and P. Coleman, Topological kondo insulators, *Physical review letters* **104**, 106408 (2010).
- [120] J. G. Checkelsky, B. A. Bernevig, P. Coleman, Q. Si, and S. Paschen, Flat bands, strange metals and the kondo effect, *Nature Reviews Materials* **9**, 509 (2024).
- [121] M. Neupane, N. Alidoust, S. Xu, T. Kondo, Y. Ishida, D.-J. Kim, C. Liu, I. Belopolski, Y. Jo, T.-R. Chang, *et al.*, Surface electronic structure of the topological kondo-insulator candidate correlated electron system *smb6*, *Nature communications* **4**, 2991 (2013).
- [122] S. G. Stewart, Heavy-fermion systems, *Reviews of Modern Physics* **56**, 755 (1984).
- [123] C.-X. Liu and B. A. Bernevig, Nodal nematic superconductivity in multiple flat-band systems, *Physical Review B* **111**, L020502 (2025).
- [124] Y.-J. Wang, G.-D. Zhou, S.-Y. Peng, B. Lian, and Z.-D. Song, Molecular pairing in twisted bilayer graphene superconductivity, *Physical Review Letters* **133**, 146001 (2024).
- [125] L. Ma, P. X. Nguyen, Z. Wang, Y. Zeng, K. Watanabe, T. Taniguchi, A. H. MacDonald, K. F. Mak, and J. Shan, Strongly correlated excitonic insulator in atomic double layers, *Nature* **598**, 585 (2021).
- [126] J. Gu, L. Ma, S. Liu, K. Watanabe, T. Taniguchi, J. C. Hone, J. Shan, and K. F. Mak, Dipolar excitonic insulator in a moiré lattice, *Nature physics* **18**, 395 (2022).
- [127] P. X. Nguyen, R. Chaturvedi, B. Zou, K. Watanabe, T. Taniguchi, A. H. MacDonald, K. F. Mak, and J. Shan, Quantum oscillations in a dipolar excitonic insulator, *arXiv preprint arXiv:2501.17829* (2025).

Supplementary Materials for “Ideal Topological Heavy Fermion Model in Two-dimensional Moiré Heterostructures with Type-II Band Alignment”

Yunzhe Liu,¹ Anoj Aryal,² Dumitru Calugaru,³ Zhenyao Fang,² Kaijie Yang,⁴
Haoyu Hu,⁵ Qimin Yan,² B. Andrei Bernevig,^{3,5,6} and Chao-xing Liu*¹

¹*Department of Physics, The Pennsylvania State University, University Park, Pennsylvania 16802, USA*

²*Department of Physics, Northeastern University, MA 02115*

³*Department of Physics, Princeton University, Princeton, NJ 08544*

⁴*Department of Materials Science and Engineering,*

University of Washington, Seattle, Washington 98195, USA

⁵*Donostia International Physics Center, P. Manuel de Lardizabal 4, 20018 Donostia-San Sebastian, Spain*

⁶*IKERBASQUE, Basque Foundation for Science, Bilbao, Spain*

A. Moiré Chern-band model

This section introduces the moiré Chern-band model and demonstrates how it captures the essential physics of the Bernevig-Hughes-Zhang (BHZ) model under moiré superlattice potentials.

The Chern-band model can be written as

$$\hat{H}_C = \sum_{\mathbf{k}\alpha\beta} a_{\alpha\mathbf{k}}^\dagger [H_C(\mathbf{k})]_{\alpha\beta} a_{\beta\mathbf{k}}, \quad (\text{S.A1})$$

$$H_C(\mathbf{k}) = \epsilon(\mathbf{k})I_{2\times 2} + \begin{pmatrix} \mathcal{M}(\mathbf{k}) & Ak_+ \\ Ak_- & -\mathcal{M}(\mathbf{k}) \end{pmatrix}, \quad (\text{S.A2})$$

where $a_{\alpha\mathbf{k}}$ ($a_{\alpha\mathbf{k}}^\dagger$) is a fermion annihilation (creation) operator with $\alpha = 1, 2$ indexing orbital basis of H_C , \mathbf{k} is the momentum in the atomic Brillouin zone (ABZ), $k_\pm = k_x \pm ik_y$, $\mathcal{M}(\mathbf{k}) = M + B\mathbf{k}^2$, $\epsilon(\mathbf{k}) = D\mathbf{k}^2$, and $I_{2\times 2}$ is a 2-by-2 identity matrix [1, 2]. The lattice version of this two-band model has been well studied in Ref. [3, 4]. A topological phase transition can be induced by changing the sign of the atomic band gap parameter M . This model is in the quantum anomalous Hall state with the Chern number $C = \pm 1$ when $MB < 0$ and in the trivial insulator state with $C = 0$ when $MB > 0$.

In addition to H_C , we also consider a superlattice potential, which can be generated either by moiré pattern [5–7] or by patterning hole arrays in dielectric materials [8, 9]. We denote the superlattice potential as $H_m(\mathbf{r})$, which satisfies $H_m(\mathbf{r} + \mathbf{R}) = H_m(\mathbf{r})$, where \mathbf{R} is the moiré superlattice vector. Here we consider hexagonal moiré potential for illustration, so that $\mathbf{R} = n_1\mathbf{a}_1^M + n_2\mathbf{a}_2^M$ with $n_1, n_2 \in \mathcal{Z}$ and $\mathbf{a}_1^M = (1, 0)a_0^M$, $\mathbf{a}_2^M = (\frac{1}{2}, \frac{\sqrt{3}}{2})a_0^M$, where a_0^M is the moiré primitive lattice constant and chosen to be $|a_0^M| = 11.46\text{nm}$ in the BHZ model calculation below. The choice of moiré lattice constant will only affect the size of moiré Brillouin zone (mBZ), but will not change any essential physics discussed below. The moiré potential Hamiltonian $H_m(\mathbf{r})$ is generally given by

$$\hat{H}_m = \int d^2r a_{\alpha\mathbf{r}}^\dagger H_m^{\alpha\alpha}(\mathbf{r}) a_{\alpha\mathbf{r}}, \quad (\text{S.A3})$$

and can be expanded in the moiré reciprocal space as

$$H_m^{\alpha\alpha}(\mathbf{r}) = \sum_{\mathbf{g} \in \mathbf{G}_M} \Delta_\alpha(\mathbf{g}) e^{i\mathbf{g}\cdot\mathbf{r}}, \quad (\text{S.A4})$$

where $a_{\alpha\mathbf{r}} = \frac{1}{\sqrt{\Omega_V}} \int d^2k a_{\alpha\mathbf{k}} e^{i\mathbf{k}\cdot\mathbf{r}}$ with the integral over the momentum \mathbf{k} in the ABZ and the system area Ω_V . $\mathbf{G}_M = \{n_1\mathbf{b}_1^M + n_2\mathbf{b}_2^M | n_1, n_2 \in \mathcal{Z}\}$ labels the group of the moiré reciprocal lattice vectors. The primitive moiré reciprocal lattice vectors are $\mathbf{b}_1^M = (2\pi, -\frac{2\pi}{\sqrt{3}})\frac{1}{a_0^M}$, $\mathbf{b}_2^M = (0, \frac{4\pi}{\sqrt{3}})\frac{1}{a_0^M}$.

The full Hamiltonian of our moiré Chern-band model is given by

$$\hat{H}_{mC} = \hat{H}_C + \hat{H}_m. \quad (\text{S.A5})$$

This model Hamiltonian serves as our starting point for the construction of the topological heavy fermion model. The symmetry group G of H_{mC} is determined by $G = G^M \cap G_C^0$, where G^M is the space symmetry group of moiré

superlattice potential (\hat{H}_m), and G_C^0 is the space symmetry group of the atomic model (H_C). The Chern-band model (S.A2) possesses continuous translation symmetry and full z-directional rotation symmetry (C_θ) with the representation matrix

$$D(C_\theta) = \begin{pmatrix} e^{-i\frac{\theta}{2}} & 0 \\ 0 & e^{-i\frac{3\theta}{2}} \end{pmatrix} \quad (\text{S.A6})$$

on the basis of Chern-band model, where θ is the rotation angle. This basis corresponds to the angular momentum $\frac{1}{2}$ and $\frac{3}{2}$ for $\alpha = 1$ and 2 orbitals. The moiré potential \hat{H}_m in Eq.(S.A4) breaks the continuous translation symmetry down to the discrete translation symmetry with the lattice vectors set by \mathbf{R} , and lowers the full rotation symmetry down to the six-fold rotation symmetry C_{6z} .

It should be noted that the moiré Chern-band model breaks time reversal (TR) symmetry and thus in a TR-invariant system, it should only describe one block of the full Hamiltonian. As we will show below, the moiré Chern-band model can describe the spin-up block of the BHZ model under moiré superlattice potentials while the spin-down block is its TR partner.

1. Bernevig-Hughes-Zhang model with moiré superlattice potential

We first consider the BHZ model with Moiré superlattice potential. The BHZ model was first discussed to describe a class of semiconductor quantum wells (QWs), e.g. HgTe/CdTe QWs [3] and InAs/GaSb QWs [10]. In Sec.D, we will also demonstrate that the BHZ model with additional off-diagonal terms is also applicable to 2D material heterostructures featuring low-energy bands around the Γ point and type-II band alignment, where the conduction and valence bands spatially reside in distinct material layers.

The BHZ model with the spin $U(1)$ symmetry or out-of-plane mirror symmetry is two copies of the Chern-band models that are related by time reversal (TR) symmetry and can be written as

$$\hat{H}_{BHZ} = \sum_{\mathbf{k}\alpha\beta} a_{\alpha\mathbf{k}}^\dagger H_{BHZ}^{\alpha\beta}(\mathbf{k}) a_{\beta\mathbf{k}}, \quad (\text{S.A7})$$

$$H_{BHZ}(\mathbf{k}) = \begin{pmatrix} H_C(\mathbf{k}) & 0 \\ 0 & H_C^*(-\mathbf{k}) \end{pmatrix}, \quad (\text{S.A8})$$

where $a_{\alpha\mathbf{k}}$ ($a_{\alpha\mathbf{k}}^\dagger$) is a fermion annihilation (creation) operator with $\alpha, \beta = 1, \dots, 4$ indexing four basis of H_{BHZ} and $H_C(\mathbf{k})$ is the Chern-band model Hamiltonian (S.A2). The basis indices $\alpha, \beta = 1, \dots, 4$ of the BHZ Hamiltonian correspond to the wavefunctions $|S, \uparrow\rangle, |P_+, \uparrow\rangle, |S, \downarrow\rangle$ and $|-P_-, \downarrow\rangle$, where P_\pm and S represent $P_x \pm iP_y$ (with orbital angular momentum ± 1) and S orbitals (with orbital angular momentum 0) while the arrows \uparrow, \downarrow represent spin up and spin down, respectively. The Hamiltonian $H_{BHZ}(\mathbf{k})$ has a block diagonal form due to spin $U(1)$ symmetry or the out-of-plane mirror symmetry M_z . The basis wave functions $|S, \uparrow\rangle$ and $|P_+, \uparrow\rangle$ of the upper block $H_C(\mathbf{k})$ are for the basis with $\alpha, \beta = 1, 2$ and possess the M_z eigenvalue $+i$, while the wave functions $|S, \downarrow\rangle$ and $|-P_-, \downarrow\rangle$ of the lower block $H_C^*(\mathbf{k})$ are for the basis with $\alpha, \beta = 3, 4$ and possess the M_z eigenvalue $-i$. These two blocks are connected to each other by TR symmetry. In the numerical calculations below, we adopt the material dependent parameters for the HgTe/CdTe quantum wells as $A = 0.365 \text{ nm}\cdot\text{eV}$, $B = 0.706 \text{ nm}^2\cdot\text{eV}$, and $D = 0.532 \text{ nm}^2\cdot\text{eV}$ [11].

The moiré potential also has the diagonal form

$$\hat{H}_m = \int d^2r a_{\alpha\mathbf{r}}^\dagger H_m^{\alpha\alpha}(\mathbf{r}) a_{\alpha\mathbf{r}}, \quad (\text{S.A9})$$

with $H_m^{\alpha\alpha}(\mathbf{r})$ given by Eq.(S.A4) and $\alpha = 1, 2, 3, 4$. The full Hamiltonian of moiré BHZ model is given by

$$\hat{H}_{mBHZ} = \hat{H}_{BHZ} + \hat{H}_m. \quad (\text{S.A10})$$

We notice that the H_{mBHZ} is block-diagonal with its upper block for spin up state ($M_z = +i$) equivalent to the moiré Chern-band Hamiltonian \hat{H}_{mC} in Eq.(S.A5), while its lower block for spin down state ($M_z = -i$) is the TR partner of \hat{H}_{mC} .

The crystalline symmetry group G of H_{mBHZ} is determined by $G = G^M \cap G^0$, where G^M is the space symmetry group of moiré superlattice potential (H_m), and G^0 is the space symmetry group of the atomic model (H_{BHZ}). For the effective Hamiltonian H_{BHZ} of the BHZ model, we denote $G^0 = D_{\infty h} \otimes G^T$, where G^T is the continuous translation group and $D_{\infty h}$ includes the rotation group about the z-axis, in-plane mirrors, and inversion. To be concrete, we consider a hexagonal moiré potential and, for the illustrative purpose, choose the symmetry group G^M of \hat{H}_m to be $P6/mmm$, giving rise to $G = G^M \cap G^0 = P6/mmm$ for the whole system. It should be noted that choosing different types of moiré potential will not change the main physics discussed below.

B. Moiré superlattice potential with the first-shell approximation

In this section, we will discuss the emergence of the topological flat bands in the Chern-band model and the BHZ model with moiré superlattice potential under the first-shell approximation. We here mainly use the parameter set from HgTe/CdTe quantum wells [11].

1. Topological flat mini-bands and Phase diagram of moiré BHZ model

In this section, we consider the Moiré superlattice potential within the first-shell potential approximation, namely the summation of \mathbf{g} in Eq.(S.A4) which is limited to the first shell, defined by

$$\mathbf{G}_M^{\parallel} = \{\mathbf{b}_2^M, \mathbf{b}_1^M, -\mathbf{b}_2^M, -\mathbf{b}_1^M, \mathbf{b}_2^M + \mathbf{b}_1^M, -\mathbf{b}_2^M - \mathbf{b}_1^M\}. \quad (\text{S.B1})$$

These six momenta in \mathbf{G}_M^{\parallel} can be connected by six-fold rotation symmetry C_{6z} around the z axis in the space group $P6/mmm$. Furthermore, we consider the moiré potential existing only for the valence band, as discussed in Fig.1 in the main text, and thus only a single real parameter, $\Delta_2(\mathbf{g}) = \Delta_4(\mathbf{g}) = \Delta_0$ for $\mathbf{g} \in \mathbf{G}_M^{\parallel}$ and $\Delta_1 = \Delta_3 = 0$, can characterize the moiré potential strength within the first shell approximation.

The full Hamiltonian H_{mBHZ} described by Eqs.(S.A7), (S.A9) and (S.A10) can be written in the momentum space as

$$\hat{H}_{BHZ} = \sum_{\mathbf{k}\mathbf{g}} \sum_{\alpha\beta=1}^4 a_{\alpha\mathbf{k}\mathbf{g}}^{\dagger} H_{BHZ}^{\alpha\beta}(\mathbf{k} + \mathbf{g}) a_{\beta\mathbf{k}\mathbf{g}} \quad (\text{S.B2})$$

$$\hat{H}_m = \Delta_0 \sum_{\mathbf{k}\mathbf{g}\mathbf{g}'\alpha} \sum_{\mathbf{q} \in \mathbf{G}_M^{\parallel}} \delta(\mathbf{g}' - \mathbf{g} - \mathbf{q}) a_{\alpha\mathbf{k}\mathbf{g}}^{\dagger} a_{\alpha\mathbf{k}\mathbf{g}'} (\delta_{\alpha,2} + \delta_{\alpha,4}), \quad (\text{S.B3})$$

where $a_{\alpha\mathbf{k}\mathbf{g}}$ is a fermion annihilation operator defined in Eq.(S.A7) with α and $\beta = 1, \dots, 4$, \mathbf{k} is the momentum in the first mBZ, $\mathbf{g}, \mathbf{g}' \in \mathbf{G}_M$ (\mathbf{G}_M is the group of moiré reciprocal lattice vectors) and $\mathbf{q} \in \mathbf{G}_M^{\parallel}$ are the moiré reciprocal vectors within the first momentum shell. Here we only consider the moiré potential acting on the $\alpha = 2, 4$ components for the valence bands. To diagonalize the above moiré Hamiltonian in the momentum space numerically, we set the cut-off $G_{\Lambda} = 6|\mathbf{b}_1^M|$ for the summation of $\mathbf{g}, \mathbf{g}' \in \mathbf{G}_M$ in Eq.(S.B2) and Eq.(S.B3).

As discussed in Sec.A1, the BHZ model is block-diagonal, with each block characterized by the eigenvalue of the M_z symmetry and representing a moiré Chern-band model. We may consider the $M_z = +i$ block, and in momentum space, the corresponding moiré Chern-band model is written as

$$\begin{aligned} \hat{H}_{mC} &= \sum_{\mathbf{k}\mathbf{g}\mathbf{g}'} \sum_{\alpha,\beta=1}^2 a_{\alpha\mathbf{k}\mathbf{g}'}^{\dagger} H_{mC}^{\alpha\beta,\mathbf{g}'\mathbf{g}}(\mathbf{k}) a_{\beta\mathbf{k}\mathbf{g}} = \hat{H}_C + \hat{H}_m, \\ \hat{H}_C &= \sum_{\mathbf{k}\mathbf{g}} \sum_{\alpha,\beta=1}^2 a_{\alpha\mathbf{k}\mathbf{g}}^{\dagger} H_{BHZ}^{\alpha\beta}(\mathbf{k} + \mathbf{g}) a_{\beta\mathbf{k}\mathbf{g}}, \\ \hat{H}_m &= \Delta_0 \sum_{\mathbf{k}\mathbf{g}\mathbf{g}'} \sum_{\mathbf{q} \in \mathbf{G}_M^{\parallel}} \delta(\mathbf{g}' - \mathbf{g} - \mathbf{q}) a_{2\mathbf{k}\mathbf{g}}^{\dagger} a_{2\mathbf{k}\mathbf{g}'}. \end{aligned} \quad (\text{S.B4})$$

We can numerically diagonalize the Hamiltonian of moiré Chern-band model Hamiltonian in Eq.(S.B4) and calculate the energy dispersion. The moiré BHZ model in Eq.(S.B2) shows exactly the same energy dispersion but with each band doubly degenerate because of the combination of inversion and TR. Therefore, the band dispersion of flat bands and phase diagram are identical to the discussion of the moiré Chern-band model in the main text. Here, we focus on the parameter sets for the flat band region and show the energy dispersions in Fig.S1(a)-(c) for three different sets of values for Δ_0 and M . The top valence mini-bands, denoted as the VB1 highlighted by the red color in Fig.S1(a)-(c), can be quite flat with the bandwidth smaller than 10 meV.

We further follow the method in Ref.[12, 13] to analyze the band irreducible representation (irreps) of the VB1 in Fig.S1 at high symmetry momenta. The symmetry group of \hat{H}_{mC} in Eq.(S.B4) is described by the space group $P6$, with the wave-vector groups at high symmetry momenta Γ , \mathbf{K} , \mathbf{M} to be the point groups C_6 , C_3 and C_2 , respectively. The character tables for these wave-vector groups are shown in Tab.SI. The six-fold rotation C_{6z} acts on fermion operators as

$$C_{6z} a_{\alpha,\mathbf{k},\mathbf{g}}^{\dagger} C_{6z}^{-1} = \sum_{\alpha',\mathbf{g}'} a_{\alpha',C_{6z}\mathbf{k},\mathbf{g}'}^{\dagger} D_{\alpha'\mathbf{g}',\alpha\mathbf{g}}(C_{6z}). \quad (\text{S.B5})$$

with

$$D_{\alpha\mathbf{g}',\alpha\mathbf{g}}(C_{6z}) = \delta_{\mathbf{g}',C_{6z}\mathbf{g}}\delta_{\alpha',\alpha}e^{-i\frac{(2\alpha-1)\pi}{6}}. \quad (\text{S.B6})$$

Under C_{6z} , $H_{mC}(\mathbf{k})$ is invariant

$$D(C_{6z})H_{mC}(\mathbf{k})D^{-1}(C_{6z}) = H_{mC}(C_{6z}\mathbf{k}). \quad (\text{S.B7})$$

Based on the $D(C_{6z})$, we can get the representation matrix of two-fold rotation C_{2z} and three-fold rotation C_{3z} given by

$$D(C_{2z}) = [D(C_{6z})]^3; D(C_{3z}) = [D(C_{6z})]^2. \quad (\text{S.B8})$$

For the eigenstates of $H_{mC}(\mathbf{k})$, the band irreps at Γ , \mathbf{K} , and \mathbf{M} can be determined from the eigenvalues of the C_{6z} , C_{3z} , and C_{2z} . In Fig.S1(a)-(c), the C_{6z} , C_{3z} , and C_{2z} eigenvalues of VB1 at the high symmetry momenta in mBZ can be calculated as $\eta(\Gamma) = e^{-i\frac{\pi}{6}}$, $\theta(\mathbf{K}) = -1$, and $\epsilon(\mathbf{M}) = i$, respectively, and thus, the band irreps of VB1 is $(\bar{\Gamma}_{10}, \bar{\mathbf{K}}_4, \bar{\mathbf{M}}_3)$. Due to the C_{6z} symmetry, the Chern number of the VB1 can be related to the rotation eigenvalues [14] via

$$e^{iC\pi/3} = -\eta(\Gamma)\theta(\mathbf{K})\epsilon(\mathbf{M}) = e^{i\pi/3}, \quad (\text{S.B9})$$

leading to $C = 1 \pmod{6}$, which is consistent with the direct calculations of the Chern number for VB1.

Based on the character table in Tab.SI, the band irreps of VB1, $(\bar{\Gamma}_{10}, \bar{\mathbf{K}}_4, \bar{\mathbf{M}}_3)$, do not belong to any elementary band representation (EBR) from the Bilbao Crystallographic Server [15–17], implying the topological nature of the flat mini-band VB1. We notice that if the irreps of VB1 $(\bar{\Gamma}_{10})$ and CB1 $(\bar{\Gamma}_7)$ at Γ point exchange, the VB1 with irreps $(\bar{\Gamma}_7, \bar{\mathbf{K}}_4, \bar{\mathbf{M}}_3)$ can form an EBR ${}^2\bar{E}_1 \uparrow G(1)@1a$ as shown in Tab.SII, which means a one-dimensional induced representation of space group $P6$ induced from the representation ${}^2\bar{E}_1$ of site-symmetry group C_6 at the Wyckoff position $1a$ (the center of moiré unit cell). Here the site-symmetry group describes all the symmetry operations in the space group that leave a certain site invariant. This EBR corresponds to the orbital with the z-directional total angular momentum $J_z = \frac{3}{2}$ at the $1a$ position, schematically shown in Fig.S4(b).

In addition, the energy of the flat band can be tuned by the values of Δ_0 and M . For a small Δ_0 and negative M , the VB1 band lies close to the second valence miniband, denoted as VB2 in Fig. S1(c). VB1 moves to the bottom of the conduction mini-bands, denoted as the CB1 in Fig.S1(a), with a large Δ_0 and positive M . The Berry curvature distribution Ω_{xy} and the trace of the quantum metric $Tr(g)$ of the VB1 in the mBZ are depicted in Fig.S1(d)-(f) and (g)-(i), respectively. When the VB1 is close to the VB2, $Tr(g)$ is concentrated around the \mathbf{M} point, while the Ω_{xy} is more uniform in mBZ, as shown in Fig.S1(f) and (i). For a large Δ_0 , the VB1 moves close to the bottom of the CB1, and both Ω_{xy} and $Tr(g)$ are concentrated around the Γ point, as shown in Fig.S1(d),(e) and (g),(h). Fig.S1(j)-(l) show the ratio $\Omega_{xy}/Tr(g)$. When the VB1 is close to the CB1 bottom, we find $\Omega_{xy}/Tr(g)$ close to 1 near the Γ point of mBZ, as shown in Fig.S1(j) and (k). In this work, we focus on the large Δ_0 regime, where both $Tr(g)$ and Ω_{xy} of the topological flat band VB1 are concentrated around the Γ point, shown in Fig.S1(a), (d) and (g).

	$\bar{\Gamma}_7$	$\bar{\Gamma}_8$	$\bar{\Gamma}_9$	$\bar{\Gamma}_{10}$	$\bar{\Gamma}_{11}$	$\bar{\Gamma}_{12}$	$\bar{\mathbf{K}}_4$	$\bar{\mathbf{K}}_5$	$\bar{\mathbf{K}}_6$	$\bar{\mathbf{M}}_3$	$\bar{\mathbf{M}}_4$		
E	1	1	1	1	1	1	E	1	1	E	1	1	
C_{3z}	-1	-1	$e^{-i\frac{\pi}{3}}$	$e^{-i\frac{\pi}{3}}$	$e^{i\frac{\pi}{3}}$	$e^{i\frac{\pi}{3}}$	C_{3z}	-1	$e^{-i\frac{\pi}{3}}$	$e^{i\frac{\pi}{3}}$	C_{2z}	i	$-i$
C_{3z}^{-1}	-1	-1	$e^{i\frac{\pi}{3}}$	$e^{i\frac{\pi}{3}}$	$e^{-i\frac{\pi}{3}}$	$e^{-i\frac{\pi}{3}}$	C_{3z}^{-1}	-1	$e^{-i\frac{\pi}{3}}$	$e^{-i\frac{\pi}{3}}$			
C_{2z}	i	$-i$	i	$-i$	i	$-i$							
C_{6z}^{-1}	i	$-i$	$e^{-i\frac{5\pi}{6}}$	$e^{i\frac{\pi}{6}}$	$e^{-i\frac{\pi}{6}}$	$e^{i\frac{5\pi}{6}}$							
C_{6z}	$-i$	i	$e^{i\frac{5\pi}{6}}$	$e^{-i\frac{\pi}{6}}$	$e^{i\frac{\pi}{6}}$	$e^{-i\frac{5\pi}{6}}$							

TABLE SI: Character tables for the wave-vector group of high symmetry momenta for $P6$ space group. The wave-vector groups at Γ , \mathbf{K} and \mathbf{M} are the point groups C_6 , C_3 and C_2 , respectively.

The overall topological phase diagram and the band flatness for VB1 are discussed in Fig.1(f) of the main text. Below we will provide more information about the evolution of the band dispersion for VB1 with increasing moiré potential strength Δ_0 with a fixed atomic band gap M in Fig.S2(a)-(f). For $\Delta_0 = 0.08\text{eV}$ in Fig.S2(a), prior to the band inversion, the VB1 is topologically trivial and forms a localized Wannier orbital according to the band irreps $(\bar{\Gamma}_7, \bar{\mathbf{K}}_4, \bar{\mathbf{M}}_3)$ at high symmetry momenta, belonging to the EBR ${}^2\bar{E}_1 \uparrow G(1)$, similar to the discussion of Fig.2(a) in the main text. With increasing Δ_0 to a critical value $\Delta_{0,c1} = 0.088\text{ eV}$, we find a Dirac type of transition between the

Wyckoff position	1a	1a	1a	1a	1a	1a
Band representation	${}^2\bar{E}_1 \uparrow G(1)$	${}^1\bar{E}_1 \uparrow G(1)$	${}^2\bar{E}_2 \uparrow G(1)$	${}^1\bar{E}_3 \uparrow G(1)$	${}^2\bar{E}_3 \uparrow G(1)$	${}^1\bar{E}_2 \uparrow G(1)$
Γ	$\bar{\Gamma}_7(1)$	$\bar{\Gamma}_8(1)$	$\bar{\Gamma}_9(1)$	$\bar{\Gamma}_{10}(1)$	$\bar{\Gamma}_{11}(1)$	$\bar{\Gamma}_{12}(1)$
K	$\bar{K}_4(1)$	$\bar{K}_4(1)$	$\bar{K}_5(1)$	$\bar{K}_5(1)$	$\bar{K}_6(1)$	$\bar{K}_6(1)$
M	$\bar{M}_3(1)$	$\bar{M}_4(1)$	$\bar{M}_3(1)$	$\bar{M}_4(1)$	$\bar{M}_3(1)$	$\bar{M}_4(1)$

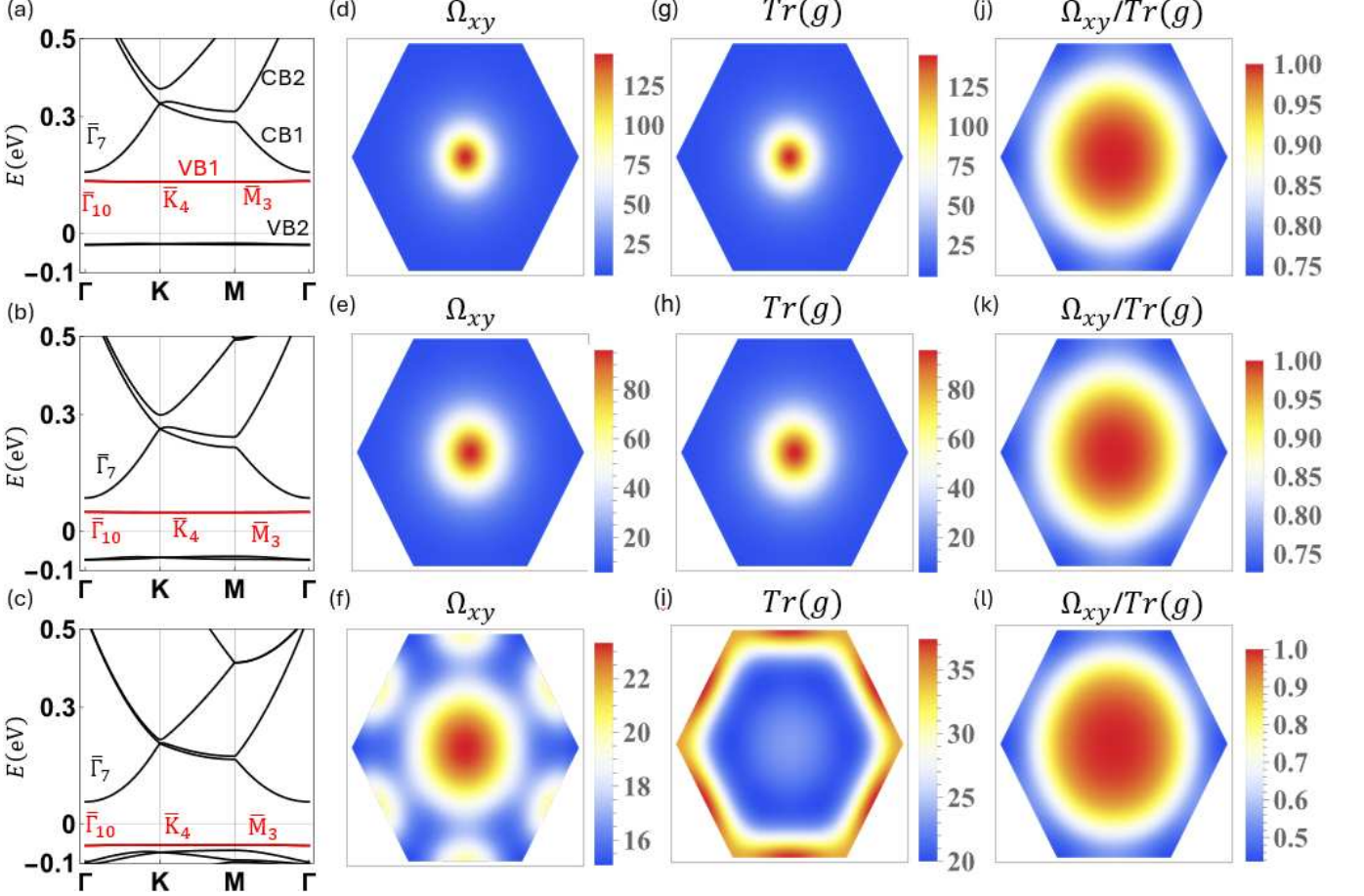
TABLE II: One dimension spinful EBR table for the $P6$ group without TR

FIG. S1: (a)-(c) Band dispersions of the moiré Chern-band model computed with the parameter sets: (a) $M = 0.135$ eV, $\Delta_0 = 0.094$ eV, (b) $M = 0.05$ eV, $\Delta_0 = 0.059$ eV, and (c) $M = -0.05$ eV, $\Delta_0 = 0.011$ eV. All parameters are along the red dashed lines in the phase diagram of Fig.1(f) in the main text. (d)-(h) The berry curvature Ω_{xy} of VB1 in the (a)-(c). (g)-(i) The trace of quantum metric $Tr(g)$ of VB1 in the (a)-(c). (j)-(l) $\Omega_{xy}/Tr(g)$ of VB1 in the (a)-(c).

VB1 and CB1 at Γ in mBZ in Fig.S2(b). With further increasing Δ_0 , the mini-band VB1 becomes topologically non-trivial due to the exchange of the irreps $\bar{\Gamma}_7$ and $\bar{\Gamma}_{10}$ at Γ between the CB1 and VB1. In this regime (Fig.S2(c)-(f)), the dispersion of the VB1 mainly comes from the band repulsion with the CB1 around Γ , and thus the VB1 is dispersive only around Γ , but flat for the momenta away from Γ in the mBZ. For $\Delta_0 = 0.091$ eV in Fig.S2(c), the dispersion of the VB1 around Γ bends down (like a hole band with negative effective mass around Γ), while with increasing Δ_0 to a larger value ($\Delta_0 = 0.1$ eV, 0.11 eV) in Fig.S2(e) and (f), the dispersion of the VB1 around Γ bends up (like an electron band with positive effective mass around Γ). For a "magic" value of Δ_0 in between ($\Delta_0 = \Delta_{0,c2} \approx 0.094$ eV), we find the VB1 is very flat with bandwidth around 5 meV and remains topological, as shown in Fig.S2(d). Although we tune Δ_0 in Fig.S2 to realize topological flat bands for a fixed M , the flatness and topology of VB1 can also be tuned by the atomic band gap M for a fixed Δ_0 , as shown in Fig.S3(a)-(c). This can be achieved via electric gating

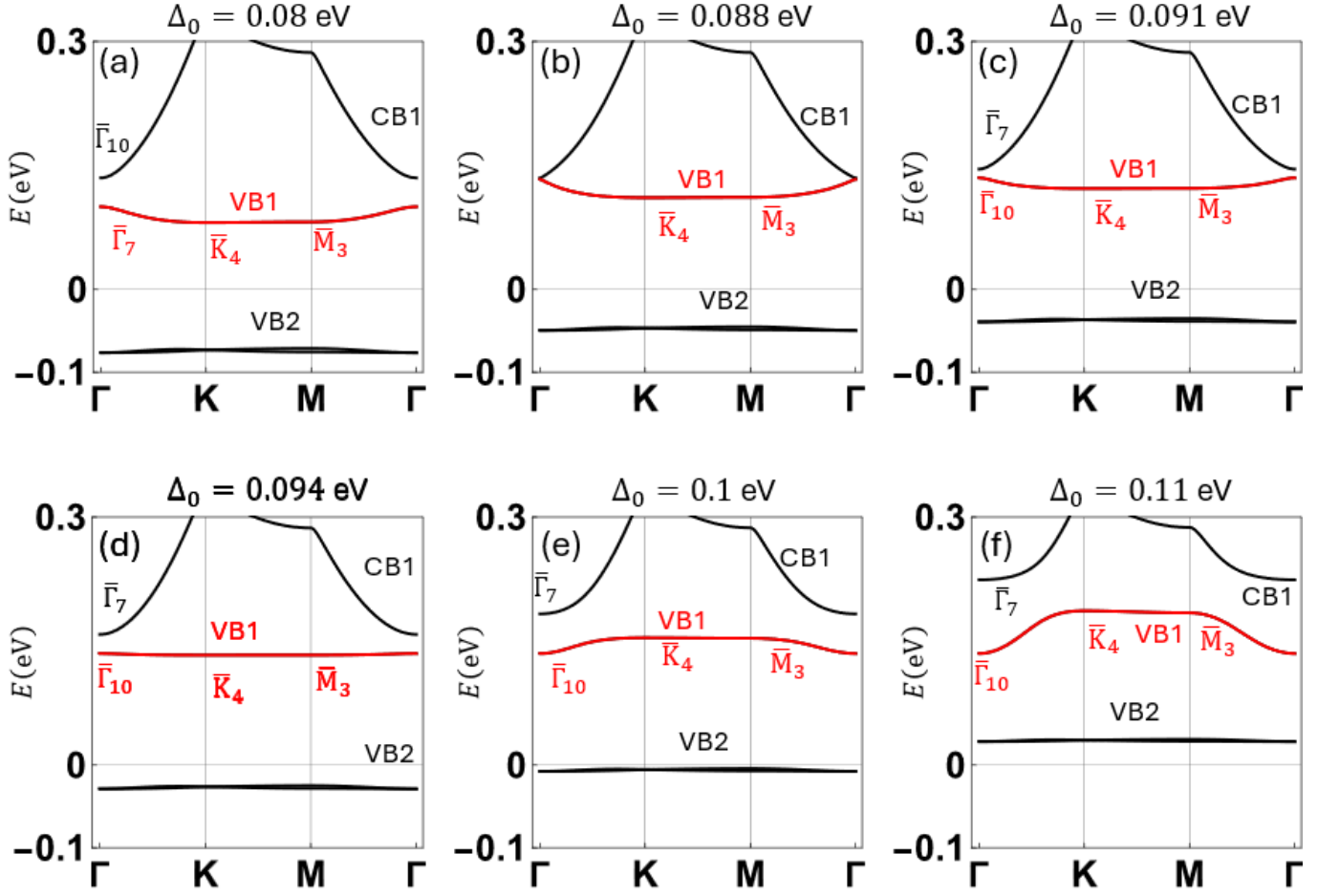


FIG. S2: (a)-(f) illustrate band dispersion of the moiré Chern-band model for different values of Δ_0 for a fixed $M = 0.135\text{eV}$. The VB1 is trivial for $\Delta_0 = 0.08\text{eV}$ in (a). A band touching between the VB1 and CB1 at Γ occurs at $\Delta_0 = 0.088\text{eV}$ in (b). From (c)-(f), the VB1 is topologically nontrivial for $\Delta_0 = 0.091, 0.094, 0.1, 0.11\text{eV}$. The VB1 becomes very flat at $\Delta_0 = 0.094\text{eV}$ in (d).

experimentally.

2. Topological heavy fermion model of moiré Chern-band Hamiltonian

In this section, we will show that the topological flat mini-bands in the strong moiré potential limit, as discussed in Fig.S1(a) and Fig.S2(d), can be well described by a topological heavy fermion (THF) model. We will first illustrate the underlying logic and the physical picture for the emergence of the heavy fermion (HF) picture for the moiré Chern-band model under strong moiré potential. Let us start from the normal bulk band gap case with $M > 0$ for the moiré Chern band model. Based on the symmetry analysis in Sec.B 1, the valence bands are mainly from the $J_z = \frac{3}{2}$ orbitals, which is composed of the atomic P_+ orbital with spin \uparrow , denoted as $|P_+, \uparrow\rangle$, where $|P_+\rangle = \frac{1}{\sqrt{2}}(|P_x\rangle + i|P_y\rangle)$, while the conduction bands are from the $J_z = \frac{1}{2}$ orbitals (without moiré potential). When increasing a moiré superlattice potential Δ_0 , the valence bands with $J_z = \frac{3}{2}$ orbitals in the moiré Chern-band model (also called heavy hole band in the semiconductor literature [18–20]) become highly localized due to the large effective mass, leading to the flat bands of VB1 (depicted by the red color in Fig.2(a) in the main text). This type of localized orbitals corresponds to the f-orbitals in HF materials [21, 22], and thus we follow this terminology to call them "f-electron" below. In contrast, due to the small effective mass and zero moiré potential on conduction bands, the conduction bands remain dispersive as shown by CB1 in Fig.S2(d). Therefore, these dispersive conduction bands play the role of metallic conducting electrons in the HF materials and thus are dubbed "c-electron" below.

The above physical scenario can be formulated into a HF model based on the Wannier function (WF) methods. To

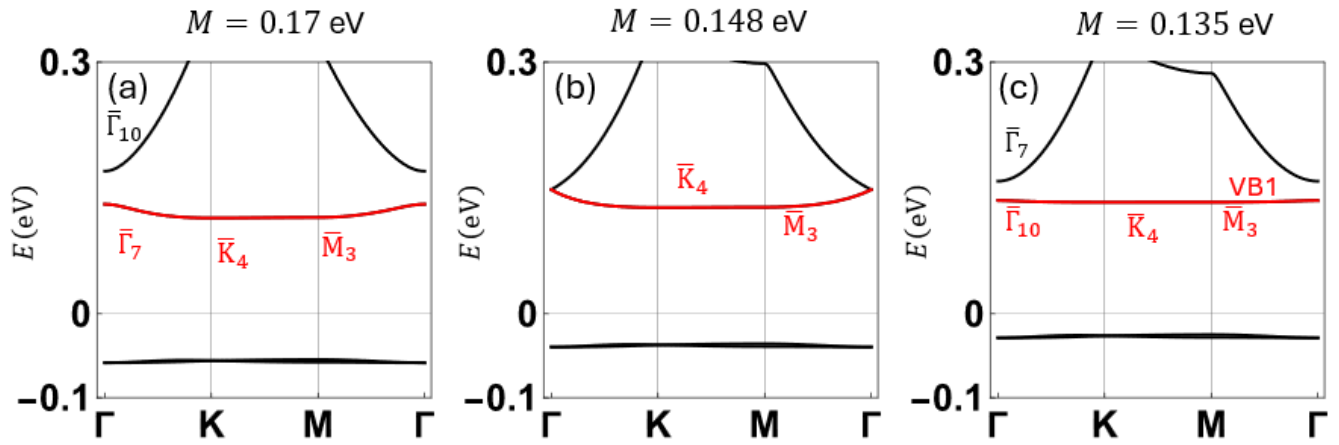


FIG. S3: (a)-(c) illustrate band dispersion of the moiré Chern-band model for different values of M for a fixed $\Delta_0 = 0.094\text{eV}$. The VB1 is trivial for $M = 0.17\text{eV}$ in (a). A band touching between the VB1 and CB1 at Γ occurs at $M = 0.148\text{eV}$ in (b). From (c), the VB1 is topologically nontrivial at $M = 0.135\text{eV}$.

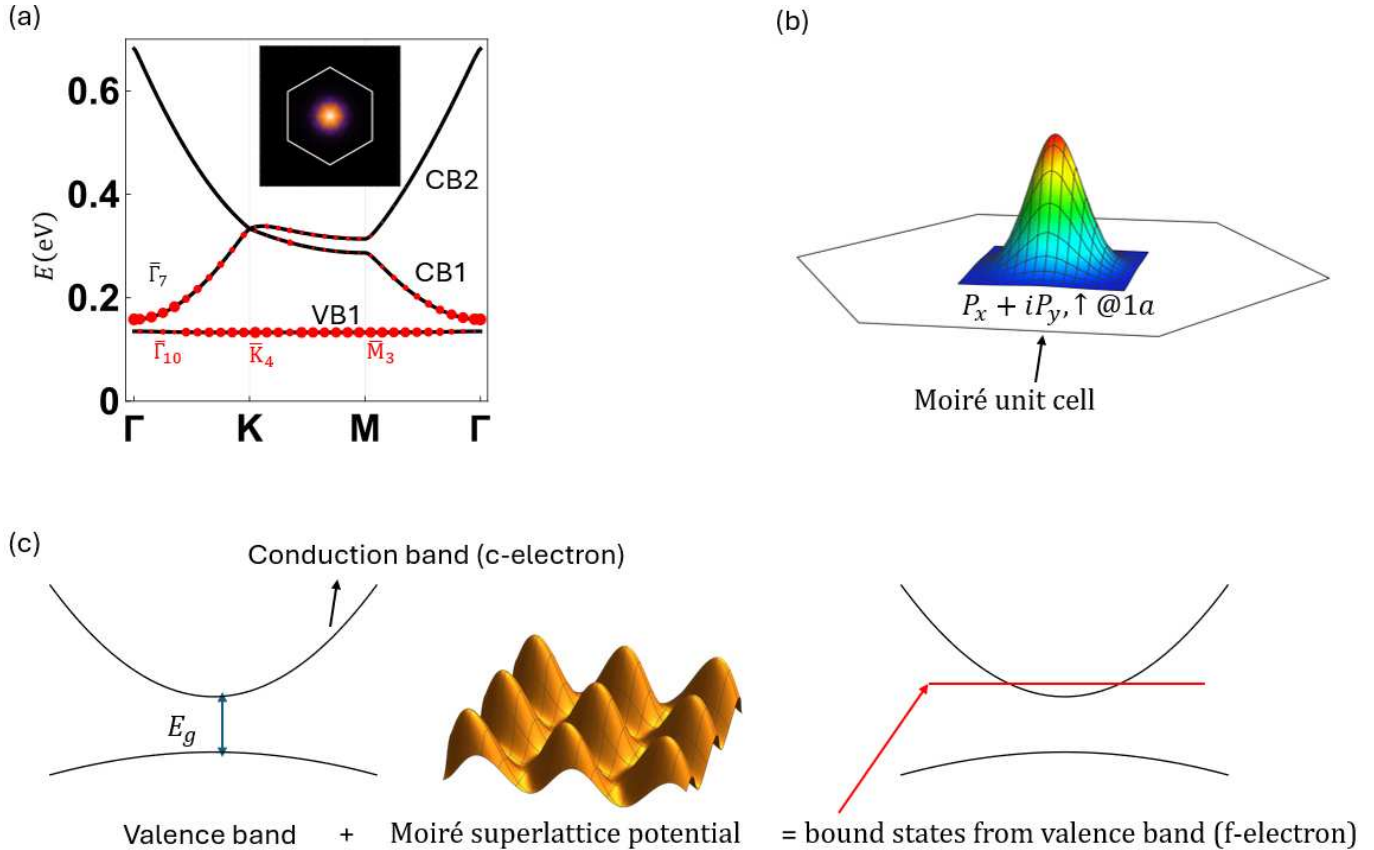


FIG. S4: (a) Energy dispersion of the moiré Chern-band model with topological flat mini-bands. The overlaps between the Bloch states and localized WF are represented by red dots with their sizes representing the overlap magnitude. Inset depicts the localized WF in one moiré unit cell. (b) depicts the WF with the $p_x + ip_y, \uparrow$ orbital localized at the Wyckoff position $1a$. (c) Schematics for the mechanism of nontrivial flat mini-band. The band inversion between the periodic localized states that originate from the valence band and conduction band leads to the nontrivial flat mini-band, which can be describe by the THF model.

achieve that, we take the same method in Ref.[12] to resolve the Wannier obstruction originating from the topological property of the VB1. We consider three mini-bands CB1, CB2 and VB1 for the moiré Chern-band model Hamiltonian (S.A5) (or the Hamiltonian (S.B4)) and construct the corresponding WF which is localized at the Wyckoff position $1a$ based on Wannier 90[23, 24]. We denote the basis wavefunctions as $|\alpha, \mathbf{k}, \mathbf{g}\rangle = a_{\alpha\mathbf{k}\mathbf{g}}^\dagger |0\rangle$ and $|\alpha, \mathbf{r}\rangle = a_{\alpha\mathbf{r}}^\dagger |0\rangle$, where the index α is chosen to be 1, 2 for the basis of the Hamiltonian (S.B4). The trial Wannier function is defined as

$$|W_{0,\mathbf{R}}\rangle = \frac{1}{\sqrt{N}} \sum_{\mathbf{k} \in mBZ} \sum_{\mathbf{g} \in \mathbf{G}_M} e^{-i\mathbf{k}\cdot\mathbf{R}} e^{-i(\mathbf{k}+\mathbf{g})\cdot\tau_a} |2, \mathbf{k}, \mathbf{g}\rangle, \quad (\text{S.B10})$$

where N is the number of moiré unit cells, \mathbf{R} is the moiré lattice vector, $\tau_a = (0, 0)$ labels the Wyckoff position $1a$ in the moiré unit cell. According to the EBR ${}^2\bar{E}_1 \uparrow G(1)$, we expect the WF from the basis with $\alpha = 2$, corresponding to the $J_z = \frac{3}{2}$ orbital. We denote the eigen-wave functions of the VB1, CB1 and CB2 as $|\phi_{n,\mathbf{k}}\rangle$, where $n = \text{VB1, CB1 or CB2}$ labels the band index.

We take the overlap $U_{0,\mathbf{k}}^n = \langle \phi_{n,\mathbf{k}} | W_{0,\mathbf{R}=0} \rangle$ as an input for the Wannier 90 codes [23, 24], which will minimize the spread $\bar{\Omega}$ of the Wannier function, defined by $\bar{\Omega} = (\langle W_{\mathbf{R}=0} | \mathbf{r}^2 | W_{\mathbf{R}=0} \rangle - |\langle W_{\mathbf{R}=0} | \mathbf{r} | W_{\mathbf{R}=0} \rangle|^2)$. The output of the Wannier 90 is a matrix $U_{\mathbf{k}}^m$, from which the WF with the maximal localization can be read out as

$$|W_{\mathbf{R}}\rangle = \frac{1}{\sqrt{N}} \sum_{\mathbf{k}, m} e^{-i\mathbf{k}\cdot\mathbf{R}} U_{\mathbf{k}}^m |\phi_{m,\mathbf{k}}\rangle. \quad (\text{S.B11})$$

The WF $|W_{\mathbf{R}}\rangle$ can be projected to the real space by defining $\mathbf{w}_{\mathbf{R}}^\alpha(\mathbf{r}) = \langle \mathbf{r}, \alpha | W_{\mathbf{R}} \rangle$ where $\mathbf{r} = (x, y)$ and $\alpha = 1, 2$ label $J_z = \frac{1}{2}$ and $\frac{3}{2}$ orbitals, respectively. The real space density distribution of the WF is given by $|\mathbf{w}_{\mathbf{R}}(\mathbf{r})|^2 = |\mathbf{w}_{\mathbf{R}}^1(\mathbf{r})|^2 + |\mathbf{w}_{\mathbf{R}}^2(\mathbf{r})|^2$. The inset of Fig.S4(a) shows $|\mathbf{w}_{\mathbf{R}=0}(\mathbf{r})|^2$ for the WF at $\mathbf{R} = 0$, which is localized at $1a$ position. The red dots in the mini-band dispersion of Fig.S4(a) show the overlap amplitude $|U_{\mathbf{k}}^m| = |\langle \phi_{m,\mathbf{k}} | W_{\mathbf{R}=0} \rangle|$ for different mini-bands labeled by the index m , from which one can see that a strong overlap between the VB1 and the WF $|W_{\mathbf{R}=0}\rangle$ occurs for most momenta away from Γ , while around Γ , the WF $|W_{\mathbf{R}=0}\rangle$ is mainly mixed into the band bottom of CB1 due to the band inversion. This suggests that the WF $|W_{\mathbf{R}=0}\rangle$ plays the role of the localized f-electron in the THF model.

Given the importance of the f-electron in constructing the THF model, we next verify that the WF $|W_{\mathbf{R}=0}\rangle$ behaves similarly as the P_+ orbital with spin \uparrow under six-fold rotation C_{6z} . Fig.S5(a)-(c) show $\mathbf{w}_{\mathbf{R}=0}^2(\mathbf{r})$, the imaginary part and the real part of $\mathbf{w}_{\mathbf{R}=0}^1(\mathbf{r})$. We can approximate them by the Gaussian function form

$$\tilde{\mathbf{w}}_{\mathbf{R}=0}^2(\mathbf{r}) = \mathcal{W}_2 e^{-r/\lambda_2}; \quad \tilde{\mathbf{w}}_{\mathbf{R}=0}^1(\mathbf{r}) = \mathcal{W}_1 (y - ix) e^{-r/\lambda_1}, \quad (\text{S.B12})$$

with $r = |\mathbf{r}|$. Fig.S5(d)-(f) show $\tilde{\mathbf{w}}_{\mathbf{R}}^2$, the imaginary part and the real part of $\tilde{\mathbf{w}}_{\mathbf{R}}^1$ with parameters $\mathcal{W}_2 = 3.84$, $\lambda_2 = 0.168a_0^M$, $\mathcal{W}_1 = 10.85/a_0^M$ and $\lambda_1 = 0.148a_0^M$. $\tilde{\mathbf{w}}_{\mathbf{R}=0}^2(\mathbf{r})$ and $\tilde{\mathbf{w}}_{\mathbf{R}=0}^1(\mathbf{r})$ satisfy the following relations

$$\tilde{\mathbf{w}}_{\mathbf{R}=0}^2(\mathbf{r}) = \tilde{\mathbf{w}}_{\mathbf{R}=0}^2(C_{6z}^{-1}\mathbf{r}); \quad \tilde{\mathbf{w}}_{\mathbf{R}=0}^1(\mathbf{r}) = e^{i\frac{\pi}{3}} \tilde{\mathbf{w}}_{\mathbf{R}=0}^1(C_{6z}^{-1}\mathbf{r}). \quad (\text{S.B13})$$

From Eq.(S.B13), we see that $\tilde{\mathbf{w}}_{\mathbf{R}=0}^1(\mathbf{r})$ has the P_+ orbital character, while $\tilde{\mathbf{w}}_{\mathbf{R}=0}^2(\mathbf{r})$ possesses P_z orbital character. Under C_{6z} , $|\mathbf{r}, \alpha\rangle$ transforms as

$$C_{6z} |\mathbf{r}, 1\rangle = e^{-i\frac{\pi}{6}} |C_{6z}\mathbf{r}, 1\rangle; \quad C_{6z} |\mathbf{r}, 2\rangle = e^{-i\frac{\pi}{2}} |C_{6z}\mathbf{r}, 2\rangle. \quad (\text{S.B14})$$

Based on Eqs.(S.B13) and (S.B14), we can get

$$\begin{aligned} C_{6z} |W_{\mathbf{R}=0}\rangle &= \sum_{\alpha} \int d\mathbf{r} C_{6z} |\mathbf{r}, \alpha\rangle \langle \mathbf{r}, \alpha | W_{\mathbf{R}=0} \rangle \\ &\approx \int d\mathbf{r} e^{-i\frac{\pi}{6}} |C_{6z}\mathbf{r}, 1\rangle \tilde{\mathbf{w}}_{\mathbf{R}=0}^1(\mathbf{r}) + e^{-i\frac{\pi}{2}} |C_{6z}\mathbf{r}, 2\rangle \tilde{\mathbf{w}}_{\mathbf{R}=0}^2(\mathbf{r}) \\ &= \int d\mathbf{r} e^{-i\frac{\pi}{2}} |\mathbf{r}, 1\rangle \tilde{\mathbf{w}}_{\mathbf{R}=0}^1(\mathbf{r}) + e^{-i\frac{\pi}{2}} |\mathbf{r}, 2\rangle \tilde{\mathbf{w}}_{\mathbf{R}=0}^2(\mathbf{r}) = e^{-i\frac{\pi}{2}} |W_{\mathbf{R}=0}\rangle. \end{aligned} \quad (\text{S.B15})$$

Eq.(S.B15) shows the WF $|W_{\mathbf{R}=0}\rangle$ carries the total angular momentum $J_z = \frac{3}{2}$, corresponding to the P_+ orbital with spin \uparrow .

Since $|\mathbf{w}_{\mathbf{R}}(\mathbf{r})|^2$ is localized near $1a$ position, as shown in the inset of Fig.S4(a), topological flat band VB1 mainly comes from the WF $|W_{\mathbf{R}}\rangle$ that is composed of the P_+ orbital with spin \uparrow at the $1a$ position, and its band character exchanges with that of the CB1, described by the eigen wave function $|\phi_{CB1,\mathbf{k}}\rangle$, around the Γ point. Thus, we

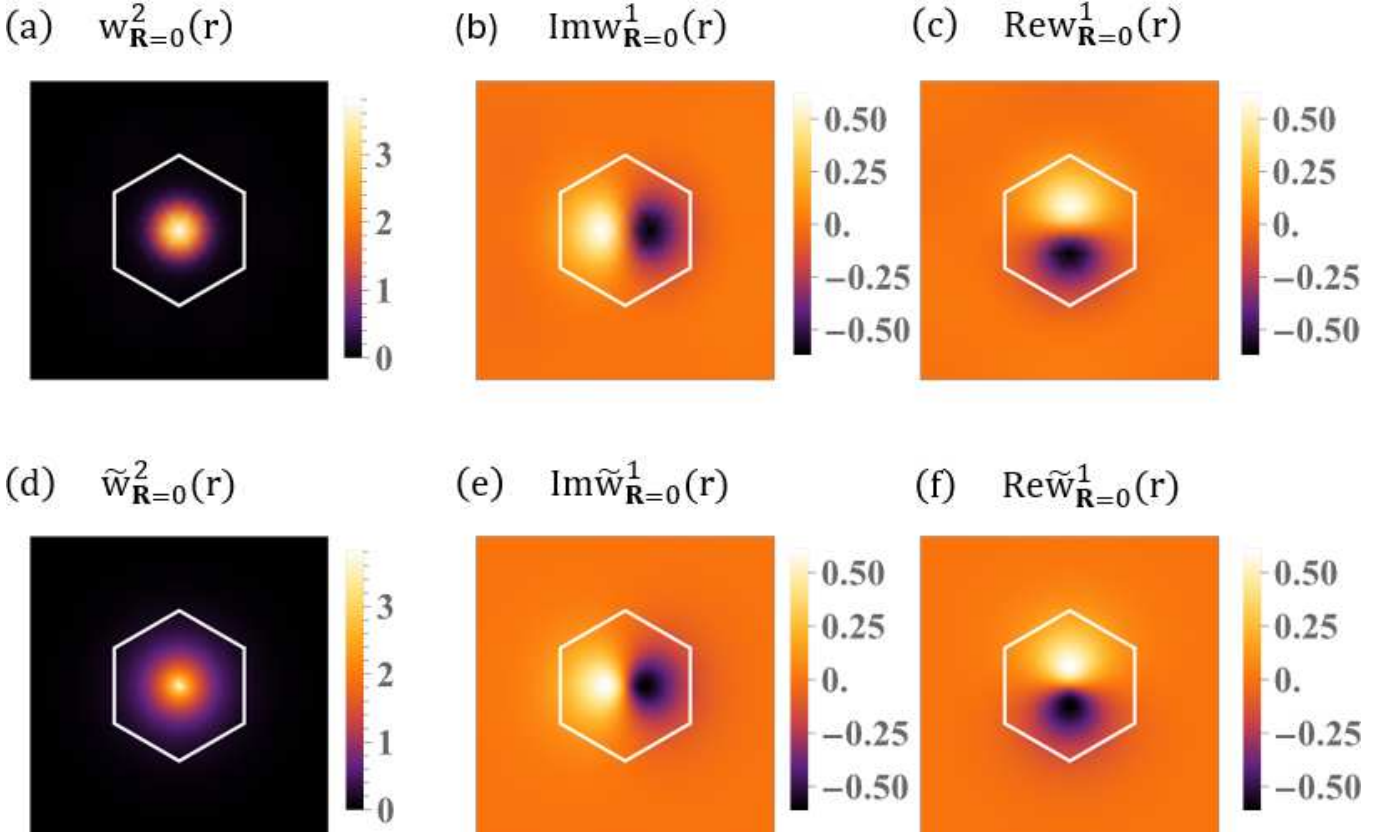


FIG. S5: (a) The real-space distribution of $\mathbf{w}_{\mathbf{R}=0}^2(\mathbf{r})$ in one moiré unit cell. (b) and (c) show the imaginary and real parts of $\mathbf{w}_{\mathbf{R}=0}^1(\mathbf{r})$ in one moiré unit cell. (d) The real-space distribution of $\tilde{\mathbf{w}}_{\mathbf{R}=0}^2(\mathbf{r})$ in moiré unit cell. (e) and (f) show the imaginary and real parts of $\tilde{\mathbf{w}}_{\mathbf{R}=0}^1(\mathbf{r})$.

introduce the annihilation operator $f_{\mathbf{R}}$ for the localized orbital $|W_{\mathbf{R}}\rangle$, called f-electron below, where \mathbf{R} denotes the moiré superlattice vector, and the annihilation operator $c_{\mathbf{k}}$ for the conduction mini-band CB1, called c-electron below, with the moiré momentum \mathbf{k} . Here we use the terminology of f-electron and c-electron in analog to the HF materials[21, 25].

With the above consideration, the single particle effective Hamiltonian preserving all symmetries in group $P6/mmm$ to the lowest order can be constructed as

$$\hat{H}_{HF}^0 = \sum_{|\mathbf{k}| < \Lambda_c} (E_c + \alpha \mathbf{k}^2) c_{\mathbf{k}}^\dagger c_{\mathbf{k}} + \sum_{\mathbf{R}} E_f f_{\mathbf{R}}^\dagger f_{\mathbf{R}} + \frac{\beta}{\sqrt{N}} \sum_{|\mathbf{k}| < \Lambda_c, \mathbf{R}} [e^{-i\mathbf{k} \cdot \mathbf{R}} (k_x + ik_y) c_{\mathbf{k}}^\dagger f_{\mathbf{R}} + h.c.], \quad (\text{S.B16})$$

where $\Lambda_c = |\phi_{B1}|$ is the momentum cutoff, and E_c, α, β, E_f are the parameters that can be computed from the WF projection as

$$E_c = \langle \phi_{VB1, \mathbf{k}=0} | H_{mC}(\mathbf{k}=0) | \phi_{VB1, \mathbf{k}=0} \rangle; \alpha = \left. \frac{\partial^2}{\partial k_x^2} \langle \phi_{VB1, \mathbf{k}} | H_{mC}(\mathbf{k}) | \phi_{VB1, \mathbf{k}} \rangle \right|_{\mathbf{k} \rightarrow 0},$$

$$E_f = \langle W_{\mathbf{R}=0} | H_{mC} | W_{\mathbf{R}=0} \rangle; \frac{\beta}{\sqrt{N}} = \left. \frac{\partial \langle \phi_{VB1, \mathbf{k}=0} | H_{mC} | W_{\mathbf{R}=0}^{(1)} \rangle}{\partial k_x} \right|_{\mathbf{k} \rightarrow 0}, \quad (\text{S.B17})$$

where the WF $|W_{\mathbf{R}=0}\rangle$ is defined in Eq.(S.B11) and $|\phi_{VB1, \mathbf{k}}\rangle$ denotes the eigen wavefunction of VB1.

Fig.S6(a) shows the comparison of the energy dispersion between the moiré Chern-band model H_{mC} in Eq.(S.B4) and the THF model H_{HF} in Eq.(S.B16) for the parameters evaluated from Eq.(S.B17), given by $E_c = 0.135$ eV, $\alpha = 1.238$ nm²· eV, $\beta = 0.195$ nm· eV and $E_f = 0.158$ eV, respectively. We further show the Berry curvature Ω_{xy} and the trace of the quantum metric $Tr(g)$ distribution of the VB1 band of \hat{H}_{HF}^0 in the mBZ, both of which are localized around the Γ point, as shown in Fig.S6(d) and (e). They compare well with Ω_{xy} and $Tr(g)$ of the VB1 band calculated from H_{mC} , shown in Fig.S6(b)-(c).

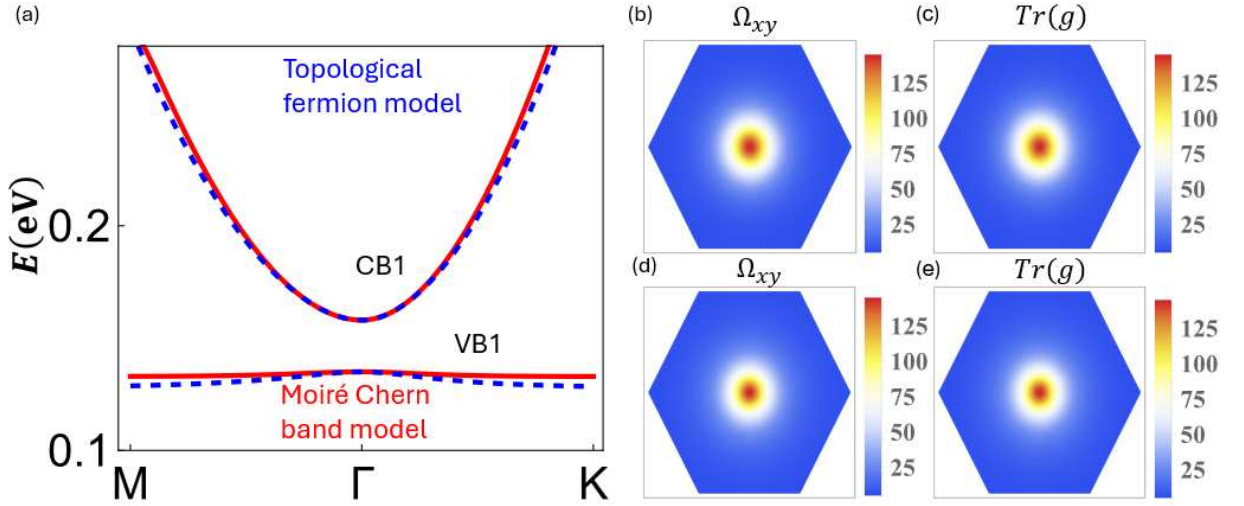


FIG. S6: (a) comparison between band dispersion of effective heavy Fermion model and that of continuum model with $M = 0.135$ eV and $\Delta_0 = 0.094$ eV. (b)-(c) The Berry curvature and the trace of quantum metric of the VB1 in the moiré Chern-band model. (d)-(e) shows the distribution of the Berry curvature and the trace of quantum metric of VB1 as a function of the momentum for the THF model.

3. Ideal Quantum Geometry in the moiré Chern-band model

Fig. S1(d)-(l) show the Berry curvature Ω_{xy} and the trace of the quantum metric $Tr(g)$, as well as their ratio, defined as $\frac{\Omega_{xy}}{Tr(g)}$, in the momentum space. We see that in the heavy fermion limit, both Ω_{xy} and $Tr(g)$ reveal peaks around Γ , and the ratio λ is close to 1 around Γ . We now study the quantum geometry property of THF model in Eq.(S.B16).

First, we rewrite Eq.(S.B16) in momentum space as

$$\begin{aligned} \hat{H}_{HF}^0 &= \sum_{|\mathbf{k}| < \Lambda_c} \left[(E_c + \alpha k^2) c_{\mathbf{k}}^\dagger c_{\mathbf{k}} + E_f f_{\mathbf{k}}^\dagger f_{\mathbf{k}} + \beta(k_x + ik_y) c_{\mathbf{k}}^\dagger f_{\mathbf{k}} + h.c. \right] \\ &= \sum_{|\mathbf{k}| < \Lambda_c} \begin{pmatrix} c_{\mathbf{k}}^\dagger & f_{\mathbf{k}}^\dagger \end{pmatrix} H_{HF}^0(\mathbf{k}) \begin{pmatrix} c_{\mathbf{k}} \\ f_{\mathbf{k}} \end{pmatrix}; \quad H_{HF}^0(\mathbf{k}) = \begin{pmatrix} E_c + \alpha k^2 & \beta k_+ \\ \beta k_- & E_f \end{pmatrix}, \end{aligned} \quad (\text{S.B18})$$

where the Fourier transform of f_R is defined as

$$f_{\mathbf{R}} = \frac{1}{\sqrt{N}} \sum_{\mathbf{k}} e^{i\mathbf{k}\cdot\mathbf{R}} f_{\mathbf{k}}. \quad (\text{S.B19})$$

We further denote $E_f = E_c + \Delta E$ and choose $\Delta E > 0$ which has the same sign as $\alpha > 0$, corresponding to the topological band region.

The eigenstates of $H_{HF}^0(k)$ are defined as

$$H_{HF}^0(\mathbf{k}) |u_{\pm}(\mathbf{k})\rangle = \mathcal{E}_{\pm}(\mathbf{k}) |u_{\pm}(\mathbf{k})\rangle, \quad (\text{S.B20})$$

where

$$\mathcal{E}_{\pm}(\mathbf{k}) = \frac{1}{2} (2E_c + \Delta E + \alpha k^2 \pm \sqrt{4\beta^2 k^2 + (\Delta E - \alpha k^2)^2}), \quad (\text{S.B21})$$

$$|u_{\pm}(k)\rangle = \frac{1}{N_{\pm}} (-\Delta E + \alpha k^2 \pm \sqrt{4\beta^2 k^2 + (\Delta E - \alpha k^2)^2}, 2\beta k_-)^T, \quad (\text{S.B22})$$

and $N_{\pm} = \sqrt{4\beta^2 k^2 + (-\Delta E + \alpha k^2 \pm \sqrt{4\beta^2 k^2 + (\Delta E - \alpha k^2)^2})^2}$ is the normalization factor. With this band dispersion, we find that when

$$\Delta E = \beta^2 / \alpha, \quad (\text{S.B23})$$

the lower energy branch has

$$\mathcal{E}_- = \frac{1}{2}(2E_c + \Delta E + \alpha k^2 - \sqrt{(\Delta E + \alpha k^2)^2}) = E_c, \quad (\text{S.B24})$$

which is an exact flat band. Therefore, we identify Eq.(S.B23) as the condition for the flat band in the THF model.

The Berry curvature and quantum metric of the lower-energy branch $|u_-(\mathbf{k})\rangle$ can be calculated as

$$\begin{aligned} \Omega_{xy} &= -2\text{Im}(\langle \partial_{k_x} u_-(\mathbf{k}) | \partial_{k_y} u_-(\mathbf{k}) \rangle) = i \frac{\langle u_-(\mathbf{k}) | \partial_{k_x} H_{HF}^0 | u_+(\mathbf{k}) \rangle \langle u_+(\mathbf{k}) | \partial_{k_y} H_{HF}^0 | u_-(\mathbf{k}) \rangle - h.c.}{(\mathcal{E}_- - \mathcal{E}_+)^2} \\ &= \frac{2\beta^2(\Delta E + \alpha k^2)}{[4\beta^2 k^2 + (\Delta E - \alpha k^2)^2]^{3/2}}, \end{aligned} \quad (\text{S.B25})$$

$$\begin{aligned} \text{Tr}(g) &= \sum_{i=x,y} \text{Re}(\langle \partial_{k_i} u_-(\mathbf{k}) | \partial_{k_i} u_-(\mathbf{k}) \rangle - \langle \partial_{k_i} u_-(\mathbf{k}) | u_-(\mathbf{k}) \rangle \langle u_-(\mathbf{k}) | \partial_{k_i} u_-(\mathbf{k}) \rangle) \\ &= \sum_{i=x,y} \frac{\langle u_-(\mathbf{k}) | \partial_{k_i} H_{HF}^0 | u_+(\mathbf{k}) \rangle \langle u_+(\mathbf{k}) | \partial_{k_i} H_{HF}^0 | u_-(\mathbf{k}) \rangle}{(\mathcal{E}_- - \mathcal{E}_+)^2} \\ &= \frac{2\beta^2((\Delta E)^2 + 2\beta^2 k^2 + \alpha^2 k^4)}{[4\beta^2 k^2 + (\Delta E - \alpha k^2)^2]^2}. \end{aligned} \quad (\text{S.B26})$$

Using the above results, we find the ratio

$$\lambda = \frac{\Omega_{xy}(\mathbf{k})}{\text{Tr}(g(\mathbf{k}))} = \frac{(\Delta E + \alpha k^2) \sqrt{4\beta^2 k^2 + (\Delta E - \alpha k^2)^2}}{\Delta E^2 + 2\beta^2 k^2 + \alpha^2 k^4}. \quad (\text{S.B27})$$

When the exact flat band condition in Eq.(S.B23) is satisfied, we also find $\lambda = 1$ for any momentum \mathbf{k} , corresponding to the "ideal quantum geometry" condition.

Therefore, we conclude that the exact flat band with ideal quantum geometry can be realized in our THF model when the condition (S.B23) is satisfied.

To understand the above result, we choose $E_c = 0$ and note that when $\Delta E = \beta^2/\alpha$, the matrix H_{HF}^0 can be written as

$$H_{HF}^0(\mathbf{k}) = \begin{pmatrix} \alpha k^2 & \beta k_+ \\ \beta k_- & \beta^2/\alpha \end{pmatrix} = \mathcal{D}^\dagger \mathcal{D}, \quad (\text{S.B28})$$

where the matrix \mathcal{D} is given by

$$\mathcal{D}^\dagger = \begin{pmatrix} \sqrt{\alpha} k_+ & 0 \\ \frac{\beta}{\sqrt{\alpha}} & 0 \end{pmatrix}; \quad \mathcal{D} = \begin{pmatrix} \sqrt{\alpha} k_- & \frac{\beta}{\sqrt{\alpha}} \\ 0 & 0 \end{pmatrix}. \quad (\text{S.B29})$$

Thus, we can consider the equation

$$\mathcal{D} \mathbf{u}_0 = 0, \quad (\text{S.B30})$$

where $\mathbf{u}_0 = (x, y)^T$ is a two-component vector. From Eq.(S.B30), it is clear that $H_{HF}^0 \mathbf{u}_0 = \mathcal{D}^\dagger \mathcal{D} \mathbf{u}_0 = 0$. Due to the form of \mathcal{D} , Eq.(S.B30) gives

$$\sqrt{\alpha} k_- x + \frac{\beta}{\sqrt{\alpha}} y = 0 \rightarrow \frac{x}{y} = -\frac{\beta}{\alpha k_-} \rightarrow \mathbf{u}_0 = \frac{1}{\sqrt{\beta^2 + \alpha^2 k^2}} \begin{pmatrix} -\beta \\ \alpha k_- \end{pmatrix}, \quad (\text{S.B31})$$

which gives the wavefunction of the zero mode. Furthermore, we notice that beside the normalization factor $\frac{1}{\sqrt{\beta^2 + \alpha^2 k^2}}$, $\begin{pmatrix} -\beta \\ \alpha k_- \end{pmatrix}$ is a holomorphic function, implying its ideal quantum geometry property [26, 27].

C. Moiré superlattice with the periodic δ -function-like potential

In this section, we will discuss the moiré superlattice potential that takes the form of periodic δ -function potential. In real space, the $H_M(\mathbf{r})$ takes the form

$$\hat{H}_m = \sum_{\mathbf{R}, \mathbf{r}} \Delta_0 \Omega_0 \delta(\mathbf{r} - \mathbf{R}) a_{\alpha\mathbf{r}}^\dagger a_{\alpha\mathbf{r}}, \quad (\text{S.C1})$$

where $\Omega_0 = \frac{\sqrt{3}}{2}a_0^2$ is the area of the unit cell for the moiré superlattice potential. In the momentum space, the moiré potential Hamiltonian takes a simple form

$$\hat{H}_m = \Delta_0 \sum_{\mathbf{k}\alpha} \sum_{\mathbf{g}, \mathbf{g}' \in \mathbf{G}_M} a_{\alpha\mathbf{k}\mathbf{g}}^\dagger a_{\alpha\mathbf{k}\mathbf{g}'}. \quad (\text{S.C2})$$

For the first shell approximation, the moiré potential Eq.(S.B3) only couples two states with their momentum difference in a short range within the first shell \mathbf{G}_M^1 . In contrast, the δ -function potential is a long range coupling in the momentum space, and the coupling between any two momenta related by a moiré reciprocal lattice vector has an equal strength.

1. Review of parabolic bands in a periodic δ -function-like potential

In this section, we will first provide a review of the free electron gas with the parabolic band in a periodic δ -function potential. We are mostly interested in the strong bound state due to the confining δ -function potential and its binding energy and localized wave function, which depend on the approximation that we made for the δ -function potential [28].

We start with the two-dimensional free electron gas in a periodic δ -function potential with the Hamiltonian

$$H_{2D} = H_0 + H_m = -\frac{\hbar^2}{2m_e} \nabla^2 + \sum_{\mathbf{R}} \Delta_0 \Omega_0 \delta(\mathbf{r} - \mathbf{R}), \quad (\text{S.C3})$$

where m_e is the electron effective mass, $\mathbf{r} = (x, y)$ and \mathbf{R} are the superlattice vectors. We may regularize the length and the energy scale of this Hamiltonian by the moiré superlattice length a_0 , and the energy unit is set as $E_0 = \frac{\hbar^2}{2m_e a_0^2}$. By defining $\tilde{\Delta}_0 = \frac{\Delta_0}{E_0}$, $(\tilde{x}, \tilde{y}) = (\frac{x}{a_0}, \frac{y}{a_0})$, $\tilde{\mathbf{R}} = \frac{\mathbf{R}}{a_0}$, and $\tilde{\Omega}_0 = \frac{\Omega_0}{a_0^2}$, we find

$$\tilde{H}_{2D} = \frac{H_{2D}}{E_0} = -\tilde{\nabla}^2 + \sum_{\mathbf{R}_M} \tilde{\Delta}_0 \tilde{\Omega}_0 \delta(\tilde{\mathbf{r}} - \tilde{\mathbf{R}}), \quad (\text{S.C4})$$

so all the terms in \tilde{H}_{2D} become dimensionless. Below we drop the notation \sim for all the symbols.

Next we transform this Hamiltonian into the momentum space by considering the basis of plane wave functions $|\mathbf{k} + \mathbf{g}\rangle$, which is defined as $\langle \mathbf{r} | \mathbf{k} + \mathbf{g} \rangle = e^{i(\mathbf{k} + \mathbf{g}) \cdot \mathbf{r}}$ and the Hamiltonian matrix element reads

$$\langle \mathbf{k} + \mathbf{g} | H_{2D} | \mathbf{k} + \mathbf{g}' \rangle = |\mathbf{k} + \mathbf{g}|^2 \delta_{\mathbf{g}, \mathbf{g}'} + \Delta_0, \quad (\text{S.C5})$$

for any \mathbf{g}, \mathbf{g}' . As we will discuss below, the binding energy of the bound state for the Hamiltonian (S.C5) diverges for a 2D periodic δ -function potential, and thus we need to impose a momentum cut-off G_Λ , e.g. $|\mathbf{g}| \leq G_\Lambda$, for the moiré reciprocal lattice vectors. With the momentum cut-off, the Hamiltonian H_{2D} can be re-written into a matrix form as

$$H_{2D}(\mathbf{k}) = H_0(\mathbf{k}) + N_g \Delta_0 P_0, \quad H_0(\mathbf{k}) = \begin{pmatrix} E_1(\mathbf{k}) & 0 & \dots & 0 \\ 0 & E_2(\mathbf{k}) & \dots & 0 \\ \vdots & \vdots & \ddots & \vdots \\ 0 & 0 & \dots & E_{N_g}(\mathbf{k}) \end{pmatrix}, \quad (\text{S.C6})$$

where N_g is the number of \mathbf{g} within the momentum cut-off G_Λ , $E_j(\mathbf{k}) = |\mathbf{k} + \mathbf{g}_j|^2$ with $j = 1, 2, \dots, N_g$ labels all possible values of \mathbf{g} , and the projection operator P_0 is

$$P_0 = |\phi_0\rangle \langle \phi_0|; \quad |\phi_0\rangle = \frac{1}{\sqrt{N_g}} \begin{pmatrix} 1 \\ 1 \\ \vdots \\ 1 \end{pmatrix}. \quad (\text{S.C7})$$

We call this form of moiré potential with a cut-off in the momentum space as the periodic δ -function-like potential.

Below we will use the form of the full Green's function to solve the eigen-energies and eigen-wave functions of the Hamiltonian H_{2D} . The eigen-energies of H_{2D} can be extracted from the poles of the full Green's function, $G = (E - H_{2D})^{-1}$ of H_{2D} , or equivalently, the trace of G ,

$$\text{Tr}(G) = \text{Tr}[(E - H_{2D}(\mathbf{k}))^{-1}] = \sum_j \langle j | (E - H_{2D}(\mathbf{k}))^{-1} | j \rangle, \quad (\text{S.C8})$$

which can be written on the eigenstate basis $|j\rangle$ of H_0 in Eq.(S.C6) with the eigen-energy E_j , e.g. $H_0(\mathbf{k}) |j\rangle = E_j(\mathbf{k}) |j\rangle$, where j labels the wavefunction components for the reciprocal lattice vectors \mathbf{g}_j . Since $H_0(\mathbf{k})$ is already diagonal in the momentum space, $|j\rangle$ is independent of the momentum \mathbf{k} . Our aim is to find the analytical form of $\text{Tr}(G)$. To achieve that, we first can show the matrix element of the bare Green's function, defined as $\hat{g}(\mathbf{k}) = (E - H_0(\mathbf{k}))^{-1}$, connecting the state $|\phi_0\rangle$ is given by

$$\mathbf{g}(\mathbf{k}, E) = N_g \langle \phi_0 | \hat{g}(\mathbf{k}) | \phi_0 \rangle = N_g \langle \phi_0 | (E - H_0(\mathbf{k}))^{-1} | \phi_0 \rangle = \sum_{j=1}^{N_g} \frac{1}{E - E_j(\mathbf{k})}, \quad (\text{S.C9})$$

where we have used the explicit expression of $|\phi_0\rangle$ in Eq.(S.C7) and included an additional factor N_g in the definition of $\mathbf{g}(\mathbf{k}, E)$. The full Green's function connecting the state $|\phi_0\rangle$ is given by

$$\begin{aligned} N_g \langle \phi_0 | G | \phi_0 \rangle &= N_g \langle \phi_0 | (E - H_0(\mathbf{k}) - N_g \Delta_0 P_0)^{-1} | \phi_0 \rangle \\ &= N_g \langle \phi_0 | (1 - (E - H_0(\mathbf{k}))^{-1} N_g \Delta_0 P_0)^{-1} (E - H_0(\mathbf{k}))^{-1} | \phi_0 \rangle \\ &= N_g \langle \phi_0 | \sum_{n=0}^{\infty} (\hat{g}(\mathbf{k}) N_g \Delta_0 P_0)^n \hat{g}(\mathbf{k}) | \phi_0 \rangle \\ &= \sum_{n=0}^{\infty} \sum_i \langle \phi_0 | (\hat{g}(\mathbf{k}) N_g \Delta_0 P_0)^n | \phi_i \rangle \langle \phi_i | N_g \hat{g}(\mathbf{k}) | \phi_0 \rangle. \end{aligned} \quad (\text{S.C10})$$

In the last step, we insert a complete set of basis functions $\{|\phi_i\rangle\}$ that satisfies $\langle \phi_i | \phi_j \rangle = \delta_{i,j}$ and $\sum_{i=0}^{N_g-1} |\phi_i\rangle \langle \phi_i| = 1$, and $|\phi_{i=0}\rangle$ is just the wavefunction defined in Eq.(S.C7). The first factor in Eq.(S.C10) can be calculated as

$$\begin{aligned} \langle \phi_0 | (\hat{g}(\mathbf{k}) N_g \Delta_0 P_0)^n | \phi_i \rangle &= \langle \phi_0 | \hat{g}(\mathbf{k}) N_g \Delta_0 P_0 N_g \Delta_0 P_0 \dots \hat{g}(\mathbf{k}) N_g \Delta_0 P_0 | \phi_i \rangle \\ &= \langle \phi_0 | \hat{g}(\mathbf{k}) N_g \Delta_0 | \phi_0 \rangle \langle \phi_0 | \dots | \phi_0 \rangle \langle \phi_0 | \hat{g}(\mathbf{k}) N_g \Delta_0 | \phi_0 \rangle \langle \phi_0 | \phi_i \rangle \\ &= (\Delta_0 \mathbf{g}(\mathbf{k}, E))^n \delta_{i,0}, \end{aligned} \quad (\text{S.C11})$$

where we have used the definition of the projection operator P_0 in Eq.(S.C7) in the second line of the above derivation. Substituting Eq.(S.C11) into Eq.(S.C10), we find

$$\begin{aligned} N_g \langle \phi_0 | G | \phi_0 \rangle &= \sum_{n=0}^{\infty} (\Delta_0 \mathbf{g}(\mathbf{k}, E))^n \mathbf{g}(\mathbf{k}, E) \\ &= \frac{\mathbf{g}(\mathbf{k}, E)}{1 - \Delta_0 \mathbf{g}(\mathbf{k}, E)}. \end{aligned} \quad (\text{S.C12})$$

We next consider the identity

$$[E - H_0 - N_g \Delta_0 P_0](E - H_{2D})^{-1} = (E - H_{2D})^{-1}[E - H_0 - N_g \Delta_0 P_0] = \mathcal{I}, \quad (\text{S.C13})$$

where \mathcal{I} is an identity matrix. Now we act on the wave functions $|j\rangle$ and $|\phi_0\rangle$ on the identity (S.C13) and obtain

$$\langle \phi_0 | (E - H_{2D})^{-1} [E - H_0 - N_g \Delta_0 P_0] | j \rangle = \langle \phi_0 | j \rangle, \quad (\text{S.C14})$$

where $\langle \phi_0 | j \rangle = \frac{1}{\sqrt{N_g}}$ according to the wavefunction form in Eq.(S.C7). We can rearrange the terms in Eq.(S.C14) and obtain

$$\begin{aligned} (E - E_j) \langle \phi_0 | (E - H_{2D})^{-1} | j \rangle - \langle \phi_0 | (E - H_{2D})^{-1} N_g \Delta_0 | \phi_0 \rangle \langle \phi_0 | j \rangle &= \langle \phi_0 | j \rangle \\ \langle \phi_0 | (E - H_{2D})^{-1} | j \rangle &= \frac{\langle \phi_0 | j \rangle}{E - E_j} (1 + N_g \Delta_0 \langle \phi_0 | (E - H_{2D})^{-1} | \phi_0 \rangle) = \frac{1}{\sqrt{N_g} (E - E_j(\mathbf{k}))} \frac{1}{1 - \Delta_0 \mathbf{g}(\mathbf{k}, E)} \end{aligned} \quad (\text{S.C15})$$

where we have used Eq.(S.C12).

We also act the wave function $|j\rangle$ on both sides of the equality (S.C13), leading to

$$\begin{aligned} \langle j| [E - H_0 - N_g \Delta_0 P_0] (E - H_{2D})^{-1} |j\rangle &= 1 \rightarrow \\ (E - E_j) \langle j| (E - H_{2D})^{-1} |j\rangle &= 1 + N_g \Delta_0 \langle j| \phi_0 \rangle \langle \phi_0| (E - H_{2D})^{-1} |j\rangle \end{aligned} \quad (\text{S.C16})$$

Combined Eq.(S.C16) and Eq.(S.C15) give rise to

$$\langle j| (E - H_{2D})^{-1} |j\rangle = \frac{1}{E - E_j(\mathbf{k})} + \frac{\Delta_0}{(E - E_j(\mathbf{k}))^2} \frac{1}{1 - \Delta_0 \mathbf{g}(\mathbf{k}, E)}, \quad (\text{S.C17})$$

which leads to the analytical form of $Tr(G)$,

$$Tr(G) = \sum_j \langle j| (E - H_{2D})^{-1} |j\rangle = \mathbf{g}(\mathbf{k}, E) + \sum_j \frac{\Delta_0}{(E - E_j)^2} \frac{1}{1 - \Delta_0 \mathbf{g}(\mathbf{k}, E)}. \quad (\text{S.C18})$$

With Eq.(S.C18), we can determine the energy spectrum from the poles of $Tr(G)$. At first sight, it seems that the poles of the free Green's function trace $\mathbf{g}(\mathbf{k}, E)$, namely $E = E_j(\mathbf{k})$, should also be the poles of $Tr(G)$. However, this is *not* true. In the limit $E \rightarrow E_j$, Eq.(S.C18) is approximated by

$$\lim_{E \rightarrow E_j} [Tr(G)] \approx \lim_{E \rightarrow E_j} \left[\frac{1}{(E - E_j)} + \frac{\Delta_0}{(E - E_j)^2} \frac{1}{1 - \Delta_0 \frac{1}{(E - E_j)}} \right] = -\frac{1}{\Delta_0}, \quad (\text{S.C19})$$

from which we find $Tr(G)$ is a constant but does not diverge so that $E = E_j$ is *not* a pole of $Tr(G)$ for any finite value of Δ_0 .

From the second term in Eq.(S.C18), we can see $Tr(G)$ diverges when the condition

$$1 = \Delta_0 \mathbf{g}(\mathbf{k}, E) \quad (\text{S.C20})$$

is satisfied, which determines all poles of $Tr(G)$ in Eq.(S.C18) and gives the energy dispersion of the full Hamiltonian H_{2D} . Fig.S7(b) shows $\mathbf{g}(\mathbf{k} = \mathbf{\Gamma}, E)$ as a function of E . In this plot, the intersections between the function $\mathbf{g}(\mathbf{\Gamma}, E)$ and the horizontal line $1/\Delta_0$ are the solutions of Eq.(S.C20), and thus determine the eigen-energy spectrum of $H_{2D}(\mathbf{k} = \mathbf{\Gamma})$, e.g. $\mathcal{E}_n(\mathbf{k} = \mathbf{\Gamma})$. One can see the energy spectrum is very different for $\Delta_0 > 0$ and $\Delta_0 < 0$. For $\Delta_0 \rightarrow 0^\pm$ (or $1/\Delta_0 \rightarrow \pm\infty$), all the curves of the function $\mathbf{g}(\mathbf{\Gamma}, E)$ merge to the energy values of a parabolic band after band folding at $\mathbf{\Gamma}$ in the mBZ. Here the momentum cutoff is chosen to be $G_\Lambda = 23|b_1^M|$. For $\Delta_0 > 0$, we notice in Fig.S7(b) all the eigen-energies remain positive, so there is no bound state with negative energy, and the lowest eigen-energy has the value of ~ 0.008 for $\Delta_0 = 0.015$ and ~ 0.01 for $\Delta_0 = 0.03$, thus remaining close to zero. Fig.S7(d), (e) and (f) show the energy dispersion of H_{2D} for $\Delta_0=0$, $\Delta_0=0.015$ and $\Delta_0=0.03$, respectively. One can see the energy dispersion of the lowest conduction band remains almost unchanged for these different Δ_0 values. For $\Delta_0 < 0$, a bound state with negative eigen-energy appears, as shown by the intersection between the dashed green horizontal line and the function $\mathbf{g}(\mathbf{k} = \mathbf{\Gamma}, E)$ in Fig.S7(b) for $\Delta_0=-0.015$. The corresponding energy dispersion for $\Delta_0=-0.015$ is shown in Fig.S7(c), where all the low-energy bands are substantially influenced by moiré potential, in sharp contrast to the almost unchanged low-energy band dispersion for $\Delta_0 \geq 0$ in Fig.S7(d)-(f).

We emphasize that the binding energy of the bound state, denoted as \mathcal{E}_0 , depends on the momentum cut-off G_Λ (or equivalently N_g), and \mathcal{E}_0 diverges as $G_\Lambda \rightarrow \infty$. To see that, we can consider $\mathbf{g}(\mathbf{k}, E)$ at $\mathbf{k} = \mathbf{\Gamma}$ and change the summation of the index j to the integral over the momentum as

$$\mathbf{g}(\mathbf{\Gamma}, E) = \sum_j \frac{1}{E - g_j^2} = \frac{1}{\Omega_B} \int_0^{G_\Lambda} \frac{2\pi g}{E - g^2} dg = -\frac{\pi}{\Omega_B} \ln \left(\frac{E - G_\Lambda^2}{E} \right), \quad (\text{S.C21})$$

where Ω_B is the area of mBZ. Combining Eq.(S.C22) with Eq.(S.C20) yields

$$\mathbf{g}(\mathbf{\Gamma}, E = \mathcal{E}_0) = \frac{1}{\Delta_0} \rightarrow \mathcal{E}_0 = -\frac{G_\Lambda^2}{-1 + e^{-\frac{\Omega_B}{\Delta_0 \pi}}}. \quad (\text{S.C22})$$

This divergence originates from the mathematical simplification of the δ -function. In the numerical calculations, we always choose a cutoff, so that the moiré potential is written as

$$H_m(\mathbf{r}) = \sum_{\mathbf{g} \leq |G_\Lambda|} \Delta_0 e^{i\mathbf{g} \cdot \mathbf{r}}$$

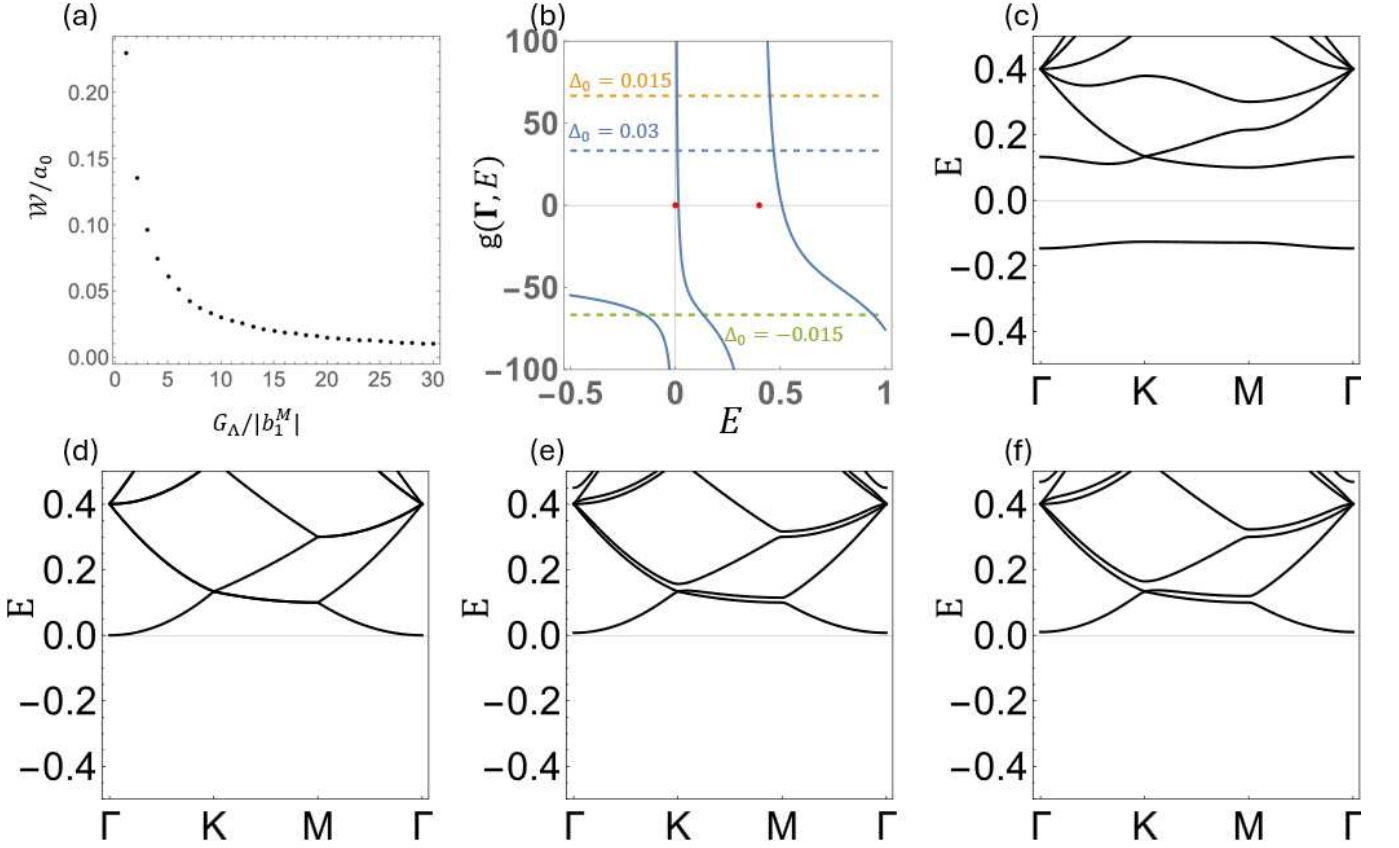


FIG. S7: (a) The broadening \mathcal{W} of δ -function-like potential for different values of G_Λ . (b) $g(\Gamma, E)$ as function of E . The yellow, blue and green dashed lines represent $1/\Delta_0$ for $\Delta_0=0.015$, $\Delta_0=0.03$ and $\Delta_0=-0.015$, respectively. The red dots represent the eigenvalue of $H_{2D}(\mathbf{k})$ at the zero moiré potential $\Delta_0 = 0$. (c)-(f) show the band dispersion for $\Delta_0=-0.015$, $\Delta_0=0$, $\Delta_0=0.015$ and $\Delta_0=0.03$, respectively. Here the momentum cutoff is chosen as $G_\Lambda = 23|b_1^M|$.

in the real space. When $|G_\Lambda| \rightarrow \infty$, the potential recovers the periodic δ potential. For a finite $|G_\Lambda|$, the potential $H_m(\mathbf{r})$ decays as a function of r and we define the broadening parameter \mathcal{W} as the distance at which $H_m(\mathcal{W}, 0)$ is half of $H_m(\mathbf{r} = 0)$, $\frac{H_m(\mathcal{W}, 0)}{H_m(\mathbf{r} = 0)} = 0.5$. Fig.S7(a) shows \mathcal{W} as a function of G_Λ , from which one can see that the broadening parameter \mathcal{W} decays rapidly when increasing the cut-off G_Λ . For a realistic periodic δ -potential-like $H_m(\mathbf{r})$, the cut-off G_Λ can be determined by the spatial broadening of $H_m(\mathbf{r})$.

Furthermore, we can also extract the eigen wavefunction form of the bound state from the above formalism. We denote the eigen wave function of H_{2D} as $|n\rangle$, namely $H_{2D}|n, \mathbf{k}\rangle = \mathcal{E}_n(\mathbf{k})|n, \mathbf{k}\rangle$ with $\mathcal{E}_n(\mathbf{k})$ determined from Eq.(S.C20). One can show

$$\begin{aligned} \lim_{E \rightarrow \mathcal{E}_n(\mathbf{k})} \langle j | (E - H_{2D})^{-1} | \phi_0 \rangle &= \sum_{n'} \lim_{E \rightarrow \mathcal{E}_n(\mathbf{k})} \langle j | (E - H_{2D})^{-1} | n', \mathbf{k} \rangle \langle n', \mathbf{k} | \phi_0 \rangle \\ &\approx \lim_{E \rightarrow \mathcal{E}_n(\mathbf{k})} (E - \mathcal{E}_n(\mathbf{k}))^{-1} \langle j | n, \mathbf{k} \rangle \langle n, \mathbf{k} | \phi_0 \rangle. \end{aligned} \quad (\text{S.C23})$$

From Eq.(S.C23), we have

$$\begin{aligned} \langle j | n, \mathbf{k} \rangle \langle n, \mathbf{k} | \phi_0 \rangle &= \lim_{E \rightarrow \mathcal{E}_n(\mathbf{k})} (E - \mathcal{E}_n(\mathbf{k})) \langle j | (E - H_{2D})^{-1} | \phi_0 \rangle \\ &= \lim_{E \rightarrow \mathcal{E}_n(\mathbf{k})} \frac{1}{\sqrt{N_g}} \frac{E - \mathcal{E}_n(\mathbf{k})}{1 - \Delta_0 \mathbf{g}(\mathbf{k}, E)} \frac{1}{E - E_j(\mathbf{k})}, \end{aligned} \quad (\text{S.C24})$$

where we have used Eq.(S.C15) in the last step. When $E \rightarrow \mathcal{E}_n$, Eq.(S.C20) should be satisfied so both the numerator $E - \mathcal{E}_n(\mathbf{k})$ and the denominator $1 - \Delta_0 \mathbf{g}(\mathbf{k}, E)$ in Eq.(S.C24) are approaching zero. This limit can be evaluated via the L'Hospital's rule as

$$\lim_{E \rightarrow \mathcal{E}_n(\mathbf{k})} \frac{E - \mathcal{E}_n(\mathbf{k})}{1 - \Delta_0 \mathbf{g}(\mathbf{k}, E)} = - \frac{1}{\Delta_0 \partial \mathbf{g}(\mathbf{k}, E) / \partial E} \Big|_{E = \mathcal{E}_n(\mathbf{k})} = \frac{1}{\Delta_0 \sum_{j'} (\mathcal{E}_n(\mathbf{k}) - E_{j'}(\mathbf{k}))^{-2}}. \quad (\text{S.C25})$$

Although some $\mathcal{E}_n(\mathbf{k})$ are very close to $E_j(\mathbf{k})$, they are not equal, i.e., $\mathcal{E}_n(\mathbf{k}) \neq E_j(\mathbf{k})$, as proven in Eq. (S.C19). Therefore, the limit in Eq.(S.C25) converges and

$$\langle j|n, \mathbf{k}\rangle \langle n, \mathbf{k}|\phi_0\rangle = \frac{1}{\sqrt{N_g}} \frac{1}{\Delta_0 \sum_{j'} (\mathcal{E}_n(\mathbf{k}) - E_{j'}(\mathbf{k}))^{-2}} \frac{1}{\mathcal{E}_n(\mathbf{k}) - E_j(\mathbf{k})}. \quad (\text{S.C26})$$

$$\langle j|n, \mathbf{k}\rangle = \frac{1}{\sqrt{N_g} \langle n, \mathbf{k}|\phi_0\rangle} \frac{1}{\Delta_0 \sum_{j'} (\mathcal{E}_n(\mathbf{k}) - E_{j'}(\mathbf{k}))^{-2}} \frac{1}{\mathcal{E}_n(\mathbf{k}) - E_j(\mathbf{k})}. \quad (\text{S.C27})$$

In the last step, we divide $\langle n, \mathbf{k}|\phi_0\rangle$ in both sides, which requires $\langle n, \mathbf{k}|\phi_0\rangle \neq 0$. Supposing $\langle n, \mathbf{k}|\phi_0\rangle = 0$, we will have $H_{2D}|n, \mathbf{k}\rangle = (H_0(\mathbf{k}) + P_0)|n, \mathbf{k}\rangle = H_0(\mathbf{k})|n, \mathbf{k}\rangle$ using the form of P_0 in Eq.(S.C7). Since $|n, \mathbf{k}\rangle$ is an eigenstate of $H_{2D}(\mathbf{k})$, e.g. $H_{2D}(\mathbf{k})|n, \mathbf{k}\rangle = \mathcal{E}(k)|n, \mathbf{k}\rangle$, we find $\mathcal{E}(k)$ has also to be an eigenstate of $H_0(\mathbf{k})$. However, we have previously proven any eigen-energy $E_j(\mathbf{k})$ of $H_0(\mathbf{k})$ is *not* a pole of $Tr(G)$ and thus cannot be an eigenstate of H_{2D} , and thus we find a contradiction, which means $\langle n, \mathbf{k}|\phi_0\rangle$ cannot be zero, $\langle n, \mathbf{k}|\phi_0\rangle \neq 0$. We note that only $\frac{1}{\mathcal{E}_n(\mathbf{k}) - E_j}$ depends on the index j , while the whole factor $\frac{1}{\sqrt{N_g} \langle n, \mathbf{k}|\phi_0\rangle} \frac{1}{\Delta_0 \sum_{j'} (\mathcal{E}_n(\mathbf{k}) - E_{j'}(\mathbf{k}))^{-2}}$ in front of $\frac{1}{\mathcal{E}_n(\mathbf{k}) - E_j}$ in Eq.(S.C27) is independent of j and thus just the normalization factor. Therefore, we can write the wavefunction as

$$\langle j|n, \mathbf{k}\rangle = N_{2D} \frac{1}{\mathcal{E}_n(\mathbf{k}) - E_j(\mathbf{k})} \quad (\text{S.C28})$$

where $N_{2D} = \frac{1}{\sqrt{N_g} \langle n, \mathbf{k}|\phi_0\rangle} \frac{1}{\Delta_0 \sum_{j'} (\mathcal{E}_n(\mathbf{k}) - E_{j'}(\mathbf{k}))^{-2}}$ is regarded as the normalization factor.

We denote the localized eigen-wavefunction of the Hamiltonian in Eq.(S.C6) of bounded state as $|0, \mathbf{k}\rangle$. For the wavefunction at Γ , namely $|0, \Gamma\rangle$, its real space form can be approximated as

$$\langle \mathbf{r}|0, \Gamma\rangle = \sum_j \langle j|0, \Gamma\rangle e^{i\mathbf{g}_j \cdot \mathbf{r}} \approx \frac{1}{\Omega_B} \int d\mathbf{g} e^{i\mathbf{g} \cdot \mathbf{r}} \langle \mathbf{g}|0, \Gamma\rangle, \quad (\text{S.C29})$$

where we change the summation over the discrete \mathbf{g}_j to the integral over the continuous variable \mathbf{g} . Using Eq.(S.C27), we find

$$\langle \mathbf{r}|0, \Gamma\rangle = \frac{N_{2D}}{(2\pi)^2} \int \frac{1}{\mathcal{E}_0(\Gamma) - \mathbf{g}^2} e^{i\mathbf{g} \cdot \mathbf{r}} d\mathbf{g} = -N_{2D} K_0(\sqrt{-\mathcal{E}_0(\Gamma)}|\mathbf{r}|), \quad (\text{S.C30})$$

where $K_0(\mathbf{r})$ is the modified Bessel function of the second kind. In the limit $|\mathbf{r}| \gg 1$, the asymptotic behavior of $K_0(\mathbf{r})$ is given by $K_0(\mathbf{r}) \approx \sqrt{\frac{\pi}{2|\mathbf{r}|}} e^{-\sqrt{-\mathcal{E}_0(\Gamma)}|\mathbf{r}|}$, thus corresponding to an exponentially localized wavefunction in periodic δ -like-function.

From the above form (S.C27) of the eigen wavefunction, we also numerically examine the localized wavefunction form of the bound state, denoted as $|0, \mathbf{k}\rangle$, for different values of the cut-off G_Λ in Fig.S8. Fig.S8(a)-(c) shows the moiré superlattice potential form for different cut-off values of G_Λ , from which one can see the confining potential becomes more and more similar to a δ -function potential as G_Λ is increased. At the same time, the real space form of the bound state eigen wavefunction, denoted by $|\langle \mathbf{r}|0, \Gamma\rangle|^2$, also becomes more and more localized around 1a Wyckoff position of moiré unit cell with increasing G_Λ in Fig.S8(d)-(f). Here we keep $\Delta_0 = -0.05$.

2. Moiré Chern-band model with a periodic δ -function potential

Now we apply the periodic δ -function potential to the Chern-band model, and the full Hamiltonian is H_{mC} in Eq.(S.A5) with the Chern-band Hamiltonian H_C in Eq.(S.A2). In the Sec.C1, we have shown that for a small positive Δ_0 , the band dispersion around the conduction band bottom remains almost unchanged. Therefore, for the convenience of deriving a compact formalism, we apply the periodic δ -function-like potential to both the conduction and valence bands with $\Delta_0 > 0$. H_m is given by the periodic δ -function-like potential in Eq.(S.C2). In the momentum space, the full Hamiltonian reads

$$H_{mC}(\mathbf{k}) = H_0(\mathbf{k}) + H_m = H_0(\mathbf{k}) + N_g \Delta_0 P_0 \quad (\text{S.C31})$$

$$H_0(\mathbf{k}) = \begin{pmatrix} H_C(\mathbf{k} + \mathbf{g}_1) & 0 & \dots & 0 \\ 0 & H_C(\mathbf{k} + \mathbf{g}_2) & \dots & 0 \\ \vdots & \vdots & \ddots & \vdots \\ 0 & 0 & \dots & H_C(\mathbf{k} + \mathbf{g}_{N_g}) \end{pmatrix}, \quad (\text{S.C32})$$

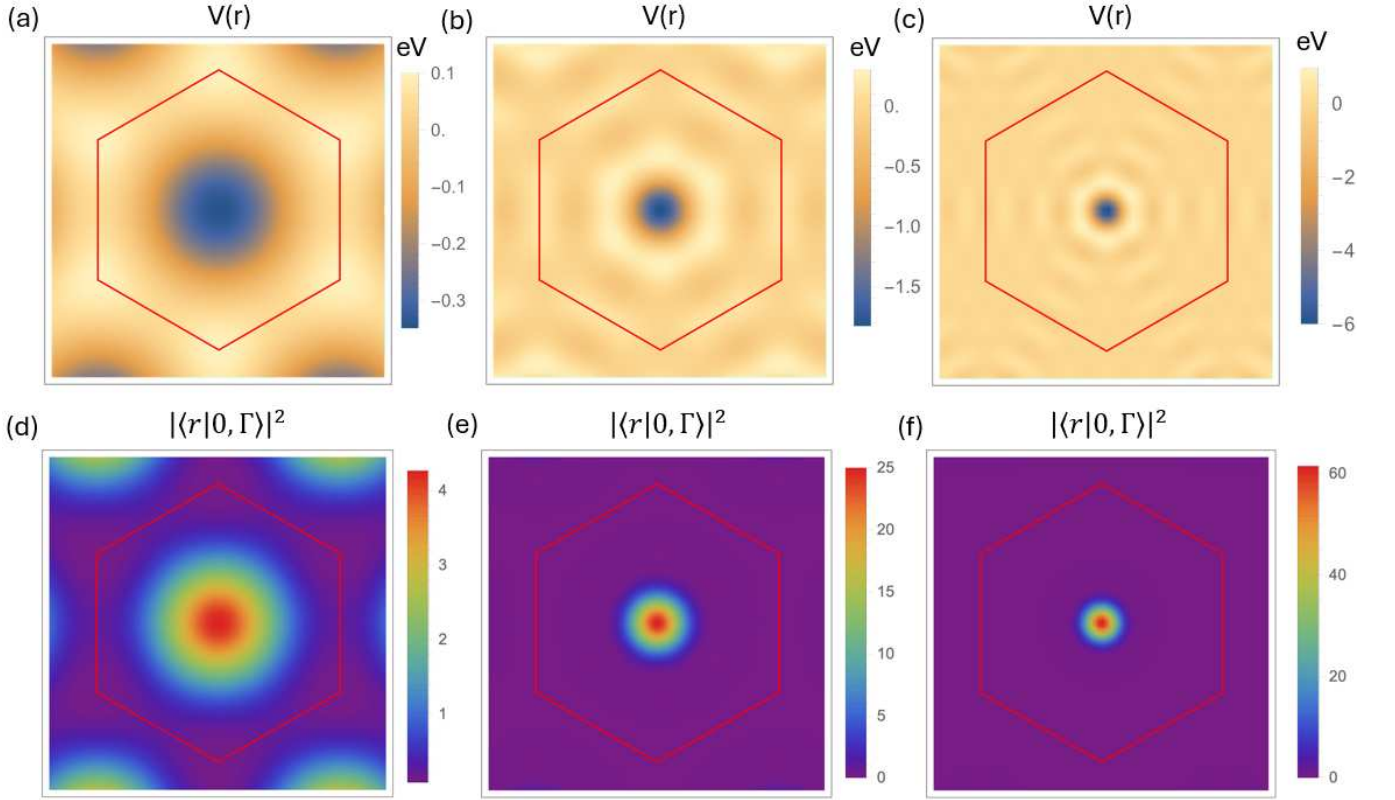


FIG. S8: (a)-(c) $V(r)$ with $\Delta_0 = -0.05$ at $G_\Lambda = |b_1^M|$, $3|b_1^M|$ and $6|b_1^M|$. (d)-(f) $|\langle r|0, \Gamma\rangle|^2$ with $\Delta_0 = -0.05$ at $G_\Lambda = |b_1^M|$, $3|b_1^M|$ and $6|b_1^M|$.

where $H_C(\mathbf{k})$ is a 2×2 matrix defined in Eq.(S.A2), \mathbf{g}_j is the moiré reciprocal lattice vectors within the momentum cut-off G_Λ ($j = 1, 2, \dots, N_g$), and

$$P_0 = |\phi_0\rangle \langle \phi_0| \otimes 1_{2 \times 2} \quad (\text{S.C33})$$

is the projection operator with $|\phi_0\rangle$ defined in Eq.(S.C7) and $1_{2 \times 2}$ is the 2-by-2 identity matrix.

Below we define $|\phi_0, \alpha\rangle = |\phi_0\rangle \otimes |\alpha\rangle$, with $\alpha = 1, 2$ indexing two orbital basis of H_C . The Moiré term can be written as $H_m = N_g \Delta_0 (|\phi_0, 1\rangle \langle \phi_0, 1| + |\phi_0, 2\rangle \langle \phi_0, 2|)$. For the derivation below, we define $|j, \alpha\rangle$ as $|j, \alpha\rangle = |j\rangle \otimes |\alpha\rangle$ for j indexing the moiré reciprocal lattice vector, so that we have $\langle j, \alpha| H_0(\mathbf{k}) |j', \beta\rangle = H_C^{\alpha\beta}(\mathbf{k} + \mathbf{g}_j) \delta_{j'j}$. $|j, \alpha\rangle$ is independent of the momentum \mathbf{k} .

The bare Green's function is defined by the matrix inverse

$$\hat{g}(\mathbf{k}) = (E 1_{2N_g \times 2N_g} - H_0(\mathbf{k}))^{-1} \quad (\text{S.C34})$$

and its component connecting the state $|\phi_0, \alpha\rangle$ and $|\phi_0, \beta\rangle$ is given by

$$\mathbf{g}_{\alpha, \beta}^0(\mathbf{k}, E) = N_g \langle \phi_0, \alpha | \hat{g} | \phi_0, \beta \rangle = N_g \langle \phi_0, \alpha | (E 1_{2N_g \times 2N_g} - H_0(\mathbf{k}))^{-1} | \phi_0, \beta \rangle. \quad (\text{S.C35})$$

By using the form of $|\phi_0\rangle$ in Eq.(S.C7), we can further define the matrix form $\mathbf{g}(k, E)$ as

$$\mathbf{g}(\mathbf{k}, E) = \sum_j \mathbf{g}^0(\mathbf{k} + \mathbf{g}_j, E), \quad (\text{S.C36})$$

where

$$\mathbf{g}^0(\mathbf{k} + \mathbf{g}_j, E) = \frac{1}{E 1_{2 \times 2} - H_C(\mathbf{k} + \mathbf{g}_j)} \quad (\text{S.C37})$$

is a 2×2 matrix. The full Green's function is defined as

$$G = (E 1_{2N_g \times 2N_g} - H_{mC}(\mathbf{k}))^{-1} \quad (\text{S.C38})$$

and its component connecting the state $|\phi_0, \alpha\rangle$ and $|\phi_0, \beta\rangle$ is given by

$$\begin{aligned}
N_g \langle \phi_0, \alpha | G | \phi_0, \beta \rangle &= N_g \langle \phi_0, \alpha | (E1_{2N_g \times 2N_g} - H_0(\mathbf{k}) - H_m)^{-1} | \phi_0, \beta \rangle \\
&= N_g \langle \phi_0, \alpha | (1_{2N_g \times 2N_g} - (E1_{2N_g \times 2N_g} - H_0(\mathbf{k}))^{-1} H_m)^{-1} (E1_{2N_g \times 2N_g} - H_0(\mathbf{k}))^{-1} | \phi_0, \alpha \rangle \\
&= N_g \langle \phi_0, \alpha | \sum_{n=0}^{\infty} (\hat{g}(\mathbf{k}) H_m)^n \hat{g}(\mathbf{k}) | \phi_0, \beta \rangle \\
&= N_g \sum_{n=0}^{\infty} \sum_{i, \gamma} \langle \phi_0, \alpha | (\hat{g}(\mathbf{k}) H_m)^n | \phi_i, \gamma \rangle \langle \phi_i, \gamma | \hat{g}(\mathbf{k}) | \phi_0, \beta \rangle,
\end{aligned} \tag{S.C39}$$

where $\alpha, \beta, \gamma = 1, 2$ and ϕ_i indexing a complete set of basis wavefunction with $\phi_{i=0}$ given by Eq.(S.C7). In Eq.(S.C39), we have

$$\begin{aligned}
\langle \phi_0, \alpha | (\hat{g}(k) H_m)^n | \phi_i, \gamma \rangle &= \sum_j \sum_{\gamma'} \cdots \sum_k \sum_{\gamma''} \langle \phi_0, \alpha | \hat{g}(\mathbf{k}) H_m | \phi_j, \gamma' \rangle \langle \phi_j, \gamma' | \cdots | \phi_k, \gamma'' \rangle \langle \phi_k, \gamma'' | \hat{g}(\mathbf{k}) H_m | \phi_i, \gamma \rangle \\
&= \Delta_0^n [\mathbf{g}^n(\mathbf{k}, E)]_{\alpha, \gamma} \delta_{i, 0},
\end{aligned} \tag{S.C40}$$

where we have used the form $H_m = N_g \Delta_0 P_0$ with P_0 given by Eq.(S.C33) in deriving the last step. Substituting Eq.(S.C40) into Eq.(S.C39), we get

$$\begin{aligned}
N_g \langle \phi_0, \alpha | G | \phi_0, \beta \rangle &= \sum_{n=0}^{\infty} \sum_{\gamma} \Delta_1^n [\mathbf{g}^n(\mathbf{k}, E)]_{\alpha, \gamma} \mathbf{g}(\mathbf{k}, E)_{\gamma, \beta} \\
&= \sum_{\gamma} (1_{2 \times 2} - \Delta_0 \mathbf{g}(\mathbf{k}, E))_{\alpha, \gamma}^{-1} [\mathbf{g}(\mathbf{k}, E)]_{\gamma, \beta}
\end{aligned} \tag{S.C41}$$

The corresponding 2×2 matrix form can be written as

$$\begin{aligned}
N_g \langle \phi_0 | G | \phi_0 \rangle &= \sum_{n=0}^{\infty} \Delta_0^n \mathbf{g}^n(\mathbf{k}, E) \mathbf{g}(\mathbf{k}, E) \\
&= (1_{2 \times 2} - \Delta_0 \mathbf{g}(\mathbf{k}, E))^{-1} \mathbf{g}(\mathbf{k}, E).
\end{aligned} \tag{S.C42}$$

Eq.(S.C42) is the generalization of Eq.(S.C12) to the moiré Chern-band model.

We further introduce the projection operator

$$\mathbf{P}_{\mathbf{k} + \mathbf{g}_j, \eta} = |\mathbf{k} + \mathbf{g}_j, \eta\rangle \langle \mathbf{k} + \mathbf{g}_j, \eta|, \tag{S.C43}$$

where $|\mathbf{k} + \mathbf{g}_j, \eta\rangle$ is the eigenstate of $H_C(\mathbf{k} + \mathbf{g}_j)$,

$$H_C(\mathbf{k} + \mathbf{g}_j) |\mathbf{k} + \mathbf{g}_j, \eta\rangle = E_{\eta}(\mathbf{k} + \mathbf{g}_j) |\mathbf{k} + \mathbf{g}_j, \eta\rangle \tag{S.C44}$$

with $\eta = 1, 2$ labelling two eigenstates. The project operator can be written in the Pauli matrix form,

$$\begin{aligned}
\mathbf{P}_{\mathbf{k}, \eta} &= \sum_{i=0}^3 d_{i, \mathbf{k}}^{\eta} \sigma_i \\
d_{0, \mathbf{k}}^{\eta} &= \frac{1}{2}; d_{1, \mathbf{k}}^{\eta} = \frac{\eta A k_x}{2D_{0\mathbf{k}}}; d_{2, \mathbf{k}}^{\eta} = \frac{-\eta A k_y}{2D_{0\mathbf{k}}}; d_{3, \mathbf{k}}^{\eta} = \frac{\eta \mathcal{M}(\mathbf{k})}{2D_{0\mathbf{k}}}, \\
D_{0\mathbf{k}} &= \sqrt{\mathcal{M}^2(\mathbf{k}) + A^2 k^2}
\end{aligned} \tag{S.C45}$$

for the Chern-band model Hamiltonian H_C in Eq.(S.A2). With the projection operator, we can rewrite

$$\mathbf{g}^0(\mathbf{k} + \mathbf{g}_j, E) = \sum_{\eta} \frac{\mathbf{P}_{\mathbf{k} + \mathbf{g}_j, \eta}}{E - E_{\eta}(\mathbf{k} + \mathbf{g}_j)}; \quad \mathbf{g}(\mathbf{k}, E) = \sum_j \mathbf{g}^0(\mathbf{k} + \mathbf{g}_j, E). \tag{S.C46}$$

We next need to find the trace of the full Green's function. We start with

$$\begin{aligned}
[E1_{2N_g \times 2N_g} - H_0 - N_g \Delta_0 P_0] (E1_{2N_g \times 2N_g} - H_m C)^{-1} &= (E1_{2N_g \times 2N_g} - H_m C)^{-1} [E1_{2N_g \times 2N_g} - H_0 - N_g \Delta_0 P_0] \\
&= 1_{2N_g \times 2N_g}
\end{aligned} \tag{S.C47}$$

Using Eq.(S.C47), we have

$$\begin{aligned} & \langle \phi_0, \alpha | (E1_{2N_g \times 2N_g} - H_{mC})^{-1} (E1_{2N_g \times 2N_g} - H_0) | j, \beta \rangle - \sum_{\gamma=1}^2 N_g \Delta_0 \langle \phi_0, \alpha | (E1_{2N_g \times 2N_g} - H_{mC})^{-1} | \phi_0, \gamma \rangle \langle \phi_0, \gamma | j, \beta \rangle \\ & = \langle \phi_0, \alpha | j, \beta \rangle. \end{aligned} \quad (\text{S.C48})$$

We insert the identity $1 = \sum_{j', \gamma} | j', \gamma \rangle \langle j', \gamma |$ into the first term of Eq.(S.C48) and obtain

$$\begin{aligned} & \sum_{j', \gamma} \langle \phi_0, \alpha | (E1_{2N_g \times 2N_g} - H_{mC})^{-1} | j', \gamma \rangle \langle j', \gamma | (E1_{2N_g \times 2N_g} - H_0) | j, \beta \rangle \\ & = \sum_{\gamma=1}^2 \langle \phi_0, \alpha | (E1_{2N_g \times 2N_g} - H_{mC})^{-1} | j, \gamma \rangle (E\delta_{\beta\gamma} - H_C^{\gamma\beta}(\mathbf{k} + \mathbf{g}_j)). \end{aligned} \quad (\text{S.C49})$$

Therefore, Eq.(S.C48) changes to

$$\begin{aligned} & \sum_{\gamma=1}^2 \langle \phi_0, \alpha | (E1_{2N_g \times 2N_g} - H_{mC})^{-1} | j, \gamma \rangle (E\delta_{\beta\gamma} - H_C^{\gamma\beta}(\mathbf{k} + \mathbf{g}_j)) = \\ & \langle \phi_0, \alpha | j, \beta \rangle + \sum_{\gamma=1}^2 N_g \Delta_0 \langle \phi_0, \alpha | (E1_{2N_g \times 2N_g} - H_{mC})^{-1} | \phi_0, \gamma \rangle \langle \phi_0, \gamma | j, \beta \rangle. \end{aligned} \quad (\text{S.C50})$$

We can further simplify Eq.(S.C50) by the matrix inverse,

$$\begin{aligned} & \sum_{\beta, \gamma=1}^2 \langle \phi_0, \alpha | (E1_{2N_g \times 2N_g} - H_{mC})^{-1} | j, \gamma \rangle (E1_{2 \times 2} - H_C(\mathbf{k} + \mathbf{g}_j))_{\gamma, \beta} (E1_{2 \times 2} - H_C(\mathbf{k} + \mathbf{g}_j))_{\beta, \eta}^{-1} \\ & = \sum_{\beta=1}^2 \left(\frac{\delta_{\alpha, \beta}}{\sqrt{N_g}} + \sum_{\gamma=1}^2 N_g \Delta_0 \langle \phi_0, \alpha | (E1_{2N_g \times 2N_g} - H_{mC})^{-1} | \phi_0, \gamma \rangle \frac{\delta_{\gamma, \beta}}{\sqrt{N_g}} \right) (E1_{2 \times 2} - H_C(\mathbf{k} + \mathbf{g}_j))_{\beta, \eta}^{-1}, \end{aligned}$$

so that

$$\begin{aligned} \langle \phi_0, \alpha | (E1_{2N_g \times 2N_g} - H_{mC})^{-1} | j, \eta \rangle & = \frac{1}{\sqrt{N_g}} \sum_{\beta=1}^2 (\delta_{\alpha, \beta} + N_g \Delta_0 \langle \phi_0, \alpha | G | \phi_0, \beta \rangle) (E1_{2 \times 2} - H_C(\mathbf{k} + \mathbf{g}_j))_{\beta, \eta}^{-1} \\ & = \frac{1}{\sqrt{N_g}} \sum_{\beta=1}^2 (\delta_{\alpha, \beta} + \sum_{\gamma} (1_{2 \times 2} - \Delta_0 \mathbf{g}(\mathbf{k}, E))_{\alpha, \gamma}^{-1} [\Delta_0 \mathbf{g}(\mathbf{k}, E)]_{\gamma, \beta}) (E1_{2 \times 2} - H_C(\mathbf{k} + \mathbf{g}_j))_{\beta, \eta}^{-1} \\ & = \frac{1}{\sqrt{N_g}} \sum_{\beta=1}^2 (1_{2 \times 2} - \Delta_0 \mathbf{g}(\mathbf{k}, E))_{\alpha, \beta}^{-1} (E1_{2 \times 2} - H_C(\mathbf{k} + \mathbf{g}_j))_{\beta, \eta}^{-1}, \end{aligned} \quad (\text{S.C51})$$

where we have used $\langle \phi_0, \alpha | j, \beta \rangle = \frac{1}{\sqrt{N_g}} \delta_{\alpha\beta}$ and Eq.(S.C42). The above expression can be rewritten into a 2×2 matrix form

$$\langle \phi_0 | (E1_{2N_g \times 2N_g} - H_{mC})^{-1} | j \rangle = \frac{1}{\sqrt{N_g}} (1_{2 \times 2} - \Delta_0 \mathbf{g}(\mathbf{k}, E))^{-1} (E1_{2 \times 2} - H_C(\mathbf{k} + \mathbf{g}_j))^{-1}. \quad (\text{S.C52})$$

Eq.(S.C51) can be regarded as a generalization of Eq.(S.C15) to the moiré Chern-band model.

We next generalize Eq.(S.C16) as

$$\langle j, \alpha | \left[E1_{2N_g \times 2N_g} - H_0 - \sum_{\gamma=1}^2 N_g \Delta_0 | \phi_0, \gamma \rangle \langle \phi_0, \gamma | \right] (E1_{2N_g \times 2N_g} - H_{mC})^{-1} | j, \beta \rangle = \delta_{\alpha, \beta} \quad (\text{S.C53})$$

which can be simplified as

$$\begin{aligned}
& \sum_{\gamma=1}^2 \sum_{j'} \langle j, \alpha | (E1_{2N_g \times 2N_g} - H_0) | j', \gamma \rangle \langle j', \gamma | (E1_{2N_g \times 2N_g} - H_{mC})^{-1} | j, \beta \rangle = \\
& \delta_{\alpha, \beta} + \sum_{\gamma=1}^2 N_g \Delta_0 \langle j, \alpha | \phi_0, \gamma \rangle \langle \phi_0, \gamma | (E1_{2N_g \times 2N_g} - H_{mC})^{-1} | j, \beta \rangle, \\
& \sum_{\gamma} (E1_{2 \times 2} - H_C(\mathbf{k} + \mathbf{g}_j))_{\alpha\gamma} \langle j, \gamma | (E1_{2N_g \times 2N_g} - H_{mC})^{-1} | j, \beta \rangle = \\
& \delta_{\alpha, \beta} + \sum_{\eta} \Delta_0 (1_{2 \times 2} - \Delta_0 \mathbf{g}(\mathbf{k}, E))_{\alpha\eta}^{-1} (E1_{2 \times 2} - H_C(\mathbf{k} + \mathbf{g}_j))_{\eta\beta}^{-1}, \tag{S.C54}
\end{aligned}$$

where we have used Eq.(S.C51) to simplify the right side of the first equation in Eq.(S.C54). With matrix inversion, we find

$$\begin{aligned}
& \langle j, \gamma | (E1_{2N_g \times 2N_g} - H_{mC})^{-1} | j, \beta \rangle = (E1_{2 \times 2} - H_C(\mathbf{k} + \mathbf{g}_j))_{\gamma\beta}^{-1} + \\
& \sum_{\eta, \alpha} (E1_{2 \times 2} - H_C(\mathbf{k} + \mathbf{g}_j))_{\gamma\alpha}^{-1} \Delta_0 (1_{2 \times 2} - \Delta_0 \mathbf{g}(\mathbf{k}, E))_{\alpha\eta}^{-1} (E - H_C(\mathbf{k} + \mathbf{g}_j))_{\eta\beta}^{-1}. \tag{S.C55}
\end{aligned}$$

The matrix form of Eq.(S.C55) is

$$\langle j | (E1_{2N_g \times 2N_g} - H_{mC}(\mathbf{k}))^{-1} | j \rangle = \frac{1}{E1_{2 \times 2} - H_C(\mathbf{k} + \mathbf{g}_j)} + \frac{\Delta_0}{E1_{2 \times 2} - H_C(\mathbf{k} + \mathbf{g}_j)} \frac{1}{1_{2 \times 2} - \Delta_0 \mathbf{g}(\mathbf{k}, E)} \frac{1}{E1_{2 \times 2} - H_C(\mathbf{k} + \mathbf{g}_j)}. \tag{S.C56}$$

By summing over j on both sides, we get the trace of the full Green's function

$$\begin{aligned}
Tr(G) &= Tr_{\sigma} \left(\sum_j \langle j | (E1_{2N_g \times 2N_g} - H_{mC}(\mathbf{k}))^{-1} | j \rangle \right) \\
&= Tr_{\sigma} \left(\mathbf{g}(\mathbf{k}, E) + \sum_j \frac{\Delta_0}{E1_{2 \times 2} - H_C(\mathbf{k} + \mathbf{g}_j)} \frac{1}{1_{2 \times 2} - \Delta_0 \mathbf{g}(\mathbf{k}, E)} \frac{1}{E1_{2 \times 2} - H_C(\mathbf{k} + \mathbf{g}_j)} \right) \\
&= Tr_{\sigma} \left(\mathbf{g}(\mathbf{k}, E) + \Delta_0 \sum_j \mathbf{g}^0(\mathbf{k} + \mathbf{g}_j, E) \frac{1}{1_{2 \times 2} - \Delta_0 \mathbf{g}(\mathbf{k}, E)} \mathbf{g}^0(\mathbf{k} + \mathbf{g}_j, E) \right), \tag{S.C57}
\end{aligned}$$

where Tr_{σ} is taken for the 2×2 matrices. Eq.(S.C57) can be viewed as the generalization of Eq.(S.C18).

We next would like to identify the poles of $Tr(G)$. We will first show the poles of $\mathbf{g}(\mathbf{k}, E)$ are *not* the poles of $Tr(G)$. From Eq.(S.C46), the pole of $\mathbf{g}(\mathbf{k}, E)$ is given by $E = E_{\eta}(\mathbf{k} + \mathbf{g}_j)$. When $E = E_{\eta}(\mathbf{k} + \mathbf{g}_j) + \delta E$ with $\delta E \rightarrow 0$, we only need to keep the divergent terms so that

$$\mathbf{g}(\mathbf{k}, E) \approx \mathbf{g}^0(\mathbf{k} + \mathbf{g}_j, E) \approx \frac{\mathbf{P}_{\mathbf{k} + \mathbf{g}_j, \eta}}{\delta E} \tag{S.C58}$$

and $Tr(G)$ is approximated by

$$\begin{aligned}
\lim_{E \rightarrow E_{\eta}(\mathbf{k} + \mathbf{g}_j)} Tr_{\sigma}(G) &\approx \lim_{\delta E \rightarrow 0} Tr_{\sigma} \left[\frac{\mathbf{P}_{\mathbf{k} + \mathbf{g}_j, \eta}}{\delta E} + \Delta_0 \frac{\mathbf{P}_{\mathbf{k} + \mathbf{g}_j, \eta}}{\delta E} (1_{2 \times 2} - \Delta_0 \frac{\mathbf{P}_{\mathbf{k} + \mathbf{g}_j, \eta}}{\delta E})^{-1} \frac{\mathbf{P}_{\mathbf{k} + \mathbf{g}_j, \eta}}{\delta E} \right] \\
&= \lim_{\delta E \rightarrow 0} Tr_{\sigma} \left[\frac{\mathbf{P}_{\mathbf{k} + \mathbf{g}_j, \eta}}{\delta E} \cdot \left(1_{2 \times 2} + (\delta E 1_{2 \times 2} - \Delta_0 \mathbf{P}_{\mathbf{k} + \mathbf{g}_j, \eta})^{-1} \Delta_0 \mathbf{P}_{\mathbf{k} + \mathbf{g}_j, \eta} \right) \right] \\
&= \lim_{\delta E \rightarrow 0} Tr_{\sigma} \left[\mathbf{P}_{\mathbf{k} + \mathbf{g}_j, \eta} \cdot (\delta E 1_{2 \times 2} - \Delta_0 \mathbf{P}_{\mathbf{k} + \mathbf{g}_j, \eta})^{-1} \right] \\
&= \lim_{\delta E \rightarrow 0} Tr_{\sigma} \left[\frac{(\sum_{i=0}^3 d_{i, \mathbf{k} + \mathbf{g}_j}^{\eta} \sigma_i) [(\delta E - \Delta_0 d_{0, \mathbf{k} + \mathbf{g}_j}^{\eta}) \sigma_0 + \sum_{i=1}^3 \Delta_0 d_{i, \mathbf{k} + \mathbf{g}_j}^{\eta} \sigma_i]}{(\delta E - \Delta_0 d_{0, \mathbf{k} + \mathbf{g}_j}^{\eta})^2 - \sum_{i=1}^3 (\Delta_0 d_{i, \mathbf{k} + \mathbf{g}_j}^{\eta})^2} \right] \\
&= \lim_{\delta E \rightarrow 0} 2 \frac{d_{0, \mathbf{k} + \mathbf{g}_j}^{\eta} (\delta E - \Delta_0 d_{0, \mathbf{k} + \mathbf{g}_j}^{\eta}) + \sum_{i=1}^3 \Delta_0 (d_{i, \mathbf{k} + \mathbf{g}_j}^{\eta})^2}{(\delta E - \Delta_0 d_{0, \mathbf{k} + \mathbf{g}_j}^{\eta})^2 - \sum_{i=1}^3 (\Delta_0 d_{i, \mathbf{k} + \mathbf{g}_j}^{\eta})^2}. \tag{S.C59}
\end{aligned}$$

From Eq.(S.C45), we know $(d_{0,\mathbf{k}+\mathbf{g}_j}^\eta)^2 - \sum_{i=1}^3 (d_{i,\mathbf{k}+\mathbf{g}_j}^\eta)^2 = 0$, so that

$$\lim_{E \rightarrow E_\eta(\mathbf{k}+\mathbf{g}_j)} Tr(G) \approx \lim_{\delta E \rightarrow 0} \frac{2d_{0,\mathbf{k}+\mathbf{g}_j}^\eta \delta E}{-2d_{0,\mathbf{k}+\mathbf{g}_j}^\eta \Delta_0 \delta E + (\delta E)^2} \approx -\frac{1}{\Delta_0}. \quad (\text{S.C60})$$

Thus, we have proven that the pole of $\mathbf{g}(\mathbf{k}, E)$ is *not* the pole of $Tr(G)$ for any finite Δ_0 . Eq.(S.C60) is the generalization of Eq.(S.C19), and we get the same conclusion as that in 2D free electron gas with periodic δ -function potential. Since we can always choose any complete set of basis wavefunction for the computation of the trace, we have $Tr(\mathbf{P}_{\mathbf{k}+\mathbf{g}_j,\eta}) = 1$ and

$$\begin{aligned} Tr(G) &= Tr(\mathbf{g}(\mathbf{k}, E)) + \Delta_0 \sum_j Tr \left(\mathbf{g}^0(\mathbf{k} + \mathbf{g}_j, E) \frac{1}{1_{2 \times 2} - \Delta_0 \mathbf{g}(\mathbf{k}, E)} \mathbf{g}^0(\mathbf{k} + \mathbf{g}_j, E) \right) \\ &= \sum_{j,\eta} \frac{1}{E - E_\eta(\mathbf{k} + \mathbf{g}_j)} + \Delta_0 \sum_{j,\eta} \frac{1}{(E - E_\eta(\mathbf{k} + \mathbf{g}_j))^2} \langle \mathbf{k} + \mathbf{g}_j, \eta | \frac{1}{1_{2 \times 2} - \Delta_0 \mathbf{g}(\mathbf{k}, E)} | \mathbf{k} + \mathbf{g}_j, \eta \rangle, \end{aligned} \quad (\text{S.C61})$$

in which we use the basis function $|\mathbf{k} + \mathbf{g}_j, \eta\rangle$ defined in Eq.(S.C44).

As $E_\eta(\mathbf{k} + \mathbf{g}_j)$ is not a pole of $Tr(G)$, the poles of $Tr(G)$ can only come from $\langle \mathbf{k} + \mathbf{g}_j, \eta | \frac{1}{1_{2 \times 2} - \Delta_0 \mathbf{g}(\mathbf{k}, E)} | \mathbf{k} + \mathbf{g}_j, \eta \rangle$. Without losing generality, $1_{2 \times 2} - \Delta_0 \mathbf{g}(\mathbf{k}, E)$ and $\frac{1}{1_{2 \times 2} - \Delta_0 \mathbf{g}(\mathbf{k}, E)}$ can be expressed as

$$1_{2 \times 2} - \Delta_0 \mathbf{g}(\mathbf{k}, E) = \sum_{i=0}^3 \hat{\mathbf{g}}^i(\mathbf{k}, E) \sigma_i; \quad \frac{1}{1_{2 \times 2} - \Delta_0 \mathbf{g}(\mathbf{k}, E)} = \frac{\hat{\mathbf{g}}^0(\mathbf{k}, E) \sigma_0 - \sum_{i=1}^3 \hat{\mathbf{g}}^i(\mathbf{k}, E) \sigma_i}{Det(1_{2 \times 2} - \Delta_0 \mathbf{g}(\mathbf{k}, E))}. \quad (\text{S.C62})$$

Here we expand the 2-by-2 matrix of the expression $1_{2 \times 2} - \Delta_0 \mathbf{g}(\mathbf{k}, E)$ into the basis of identity matrix and Pauli matrices with the expansion coefficients defined as $\hat{\mathbf{g}}^i(\mathbf{k}, E)$. Therefore, the poles of $Tr(G)$ is given by

$$Det(1_{2 \times 2} - \Delta_0 \mathbf{g}(\mathbf{k}, \mathcal{E}_n)) = 0, \quad (\text{S.C63})$$

from which we can solve the full energy spectrum $\mathcal{E}_n(\mathbf{k})$ of our model.

Finally, we will generalize the derivation of Eq.(S.C24) to solve the eigen-wavefunctions. For the eigen-energy $\mathcal{E}_n(\mathbf{k})$, we consider

$$\lim_{E \rightarrow \mathcal{E}_n(\mathbf{k})} \langle j, \beta | (E 1_{2N_g \times 2N_g} - H_{mC})^{-1} | \phi_0, \alpha \rangle = \lim_{E \rightarrow \mathcal{E}_n(\mathbf{k})} (E - \mathcal{E}_n(\mathbf{k}))^{-1} \langle j, \beta | n, \mathbf{k} \rangle \langle n, \mathbf{k} | \phi_0, \alpha \rangle, \quad (\text{S.C64})$$

where $|n, \mathbf{k}\rangle$ is the eigenstate of H_{mC} defined as $H_{mC}(\mathbf{k}) |n, \mathbf{k}\rangle = \mathcal{E}_n(\mathbf{k}) |n, \mathbf{k}\rangle$.

On the other hand, the Hermitian conjugation of Eq.(S.C52) gives

$$\langle j, \beta | (E 1_{2N_g \times 2N_g} - H_{mC})^{-1} | \phi_0, \alpha \rangle = \frac{1}{\sqrt{N_g}} \sum_{\eta=1}^2 (E 1_{2 \times 2} - H_C(\mathbf{k} + \mathbf{g}_j))_{\beta,\eta}^{-1} (1_{2 \times 2} - \Delta_0 \mathbf{g}(\mathbf{k}, E))_{\eta,\alpha}^{-1}. \quad (\text{S.C65})$$

Comparing Eq.(S.C64) with Eq.(S.C65), we find

$$\begin{aligned} \langle j, \beta | n, \mathbf{k} \rangle \langle n, \mathbf{k} | \phi_0, \alpha \rangle &= \lim_{E \rightarrow \mathcal{E}_n(\mathbf{k})} (E - \mathcal{E}_n(\mathbf{k})) \langle j, \beta | (E 1_{2N_g \times 2N_g} - H_{mC})^{-1} | \phi_0, \alpha \rangle \\ &= \lim_{E \rightarrow \mathcal{E}_n(\mathbf{k})} (E - \mathcal{E}_n(\mathbf{k})) \frac{1}{\sqrt{N_g}} \sum_{\eta=1}^2 (E 1_{2 \times 2} - H_C(\mathbf{k} + \mathbf{g}_j))_{\beta,\eta}^{-1} (1_{2 \times 2} - \Delta_0 \mathbf{g}(\mathbf{k}, E))_{\eta,\alpha}^{-1} \end{aligned} \quad (\text{S.C66})$$

In the limit $E \rightarrow \mathcal{E}_n(\mathbf{k})$, both $E - \mathcal{E}_n(\mathbf{k})$ and $Det(1_{2 \times 2} - \Delta_0 \mathbf{g}(\mathbf{k}, E))$ equal to zero, so we need to use the L'Hospital's rule to take the limit as

$$\begin{aligned} \langle j, \beta | n, \mathbf{k} \rangle \langle n, \mathbf{k} | \phi_0, \alpha \rangle &= \lim_{E \rightarrow \mathcal{E}_n(\mathbf{k})} (E - \mathcal{E}_n(\mathbf{k})) \frac{1}{\sqrt{N_g}} \sum_{\eta=1}^2 (E 1_{2 \times 2} - H_C(\mathbf{k} + \mathbf{g}_j))_{\beta,\eta}^{-1} \left[\frac{\hat{\mathbf{g}}^0(\mathbf{k}, E) \sigma_0 - \sum_{i=1}^3 \hat{\mathbf{g}}^i(\mathbf{k}, E) \sigma_i}{Det(1_{2 \times 2} - \Delta_0 \mathbf{g}(\mathbf{k}, E))} \right]_{\eta,\alpha} \\ &= \frac{1}{\sqrt{N_g}} \left[\frac{1}{\partial_E Det(1_{2 \times 2} - \Delta_0 \mathbf{g}(\mathbf{k}, E))} \right]_{E \rightarrow \mathcal{E}_n(\mathbf{k})} \left[(\mathcal{E}_n(\mathbf{k}) 1_{2 \times 2} - H_C(\mathbf{k} + \mathbf{g}_j))^{-1} (\hat{\mathbf{g}}^0(\mathbf{k}, \mathcal{E}_n(\mathbf{k})) \sigma_0 - \sum_{i=1}^3 \hat{\mathbf{g}}^i(\mathbf{k}, \mathcal{E}_n(\mathbf{k})) \sigma_i) \right]_{\beta,\alpha} \\ &= \frac{1}{\sqrt{N_g}} \left[\frac{1}{\partial_E Det(1_{2 \times 2} - \Delta_0 \mathbf{g}(\mathbf{k}, E))} \right]_{E \rightarrow \mathcal{E}_n(\mathbf{k})} \sum_{\eta} \left[\frac{\mathbf{P}_{\mathbf{k}+\mathbf{g}_j,\eta} (\hat{\mathbf{g}}^0(\mathbf{k}, \mathcal{E}_n(\mathbf{k})) \sigma_0 - \sum_{i=1}^3 \hat{\mathbf{g}}^i(\mathbf{k}, \mathcal{E}_n(\mathbf{k})) \sigma_i)}{\mathcal{E}_n(\mathbf{k}) - E_\eta(\mathbf{k} + \mathbf{g}_j)} \right]_{\beta,\alpha} \\ &= \frac{1}{\sqrt{N_g}} \left[\frac{1}{\partial_E Det(1_{2 \times 2} - \Delta_0 \mathbf{g}(\mathbf{k}, E))} \right]_{E \rightarrow \mathcal{E}_n(\mathbf{k})} \mathcal{F}^{\beta,\alpha}(\mathbf{k}, \mathbf{g}_j), \end{aligned} \quad (\text{S.C67})$$

where $\mathcal{F}^{\beta,\alpha}(\mathbf{k}, \mathbf{g}_j) = \sum_{\eta} \frac{[\mathbf{P}_{\mathbf{k}+\mathbf{g}_j, \eta}(\hat{\mathbf{g}}^0(\mathbf{k}, \mathcal{E}_n(\mathbf{k}))\sigma_0 - \sum_{i=1}^3 \hat{\mathbf{g}}^i(\mathbf{k}, \mathcal{E}_n(\mathbf{k}))\sigma_i)]_{\beta, \alpha}}{\mathcal{E}_n(\mathbf{k}) - E_{\eta}(\mathbf{k}+\mathbf{g}_j)}$.

Since $\langle n, \mathbf{k} | \phi_0, \alpha \rangle$ at the left side of Eq.(S.C67) is independent of j, β and the states $|j, \beta\rangle$ form a complete set of basis wavefunctions, we can take the norm for both sides and the sum over both j and β and obtain

$$\sum_{j, \beta} |\langle j, \beta | n, \mathbf{k} \rangle|^2 |\langle n, \mathbf{k} | \phi_0, \alpha \rangle|^2 = \frac{1}{N_g} \left[\frac{1}{\partial_E \text{Det}(1_{2 \times 2} - \Delta_0 \mathbf{g}(\mathbf{k}, E))} \right]_{E \rightarrow \mathcal{E}_n(\mathbf{k})}^2 \sum_{j, \beta} |\mathcal{F}^{\beta, \alpha}(\mathbf{k}, \mathbf{g}_j)|^2 \quad (\text{S.C68})$$

$$|\langle n, \mathbf{k} | \phi_0, \alpha \rangle| = \frac{1}{\sqrt{N_g}} \left| \frac{1}{\partial_E \text{Det}(1_{2 \times 2} - \Delta_0 \mathbf{g}(\mathbf{k}, E))} \right|_{E \rightarrow \mathcal{E}_n(\mathbf{k})} \sqrt{\sum_{j, \beta} |\mathcal{F}^{\beta, \alpha}(\mathbf{k}, \mathbf{g}_j)|^2}, \quad (\text{S.C69})$$

where we use $\sum_{j, \beta} |\langle j, \beta | n, \mathbf{k} \rangle|^2 = 1$ as $|j, \beta\rangle$ is a complete set of basis.

With Eqs.(S.C67) and (S.C69), we can derive the form of $\langle j, \beta | n, \mathbf{k} \rangle$ up to a phase factor for any j, β once $\langle n, \mathbf{k} | \phi_0, \alpha \rangle \neq 0$. Below we will show that there must exist at least one α to satisfy $\langle n, \mathbf{k} | \phi_0, \alpha \rangle \neq 0$. To see that we can assume $\langle n, \mathbf{k} | \phi_0, \alpha \rangle = 0$ for both $\alpha = 1, 2$, and from Eq.(S.C33), we have

$$H_{mC}(\mathbf{k}) |n, \mathbf{k}\rangle = H_0(\mathbf{k}) |n, \mathbf{k}\rangle = \mathcal{E}_n(\mathbf{k}) |n, \mathbf{k}\rangle. \quad (\text{S.C70})$$

Eq.(S.C70) indicates that $\mathcal{E}_n(\mathbf{k})$ is the eigenvalue of $H_0(\mathbf{k})$. However, we have proven that the pole of $\mathbf{g}(\mathbf{k}, E)$ is *not* the pole of $\text{Tr}(G)$ for any finite Δ_0 in the above and thus we find a contradiction, which means there must be one α with non-zero $\langle n, \mathbf{k} | \phi_0, \alpha \rangle$. By substituting Eq.(S.C69) into Eq.(S.C67), we find

$$\langle j, \beta | n, \mathbf{k} \rangle = \frac{\mathcal{F}^{\beta, \alpha}(\mathbf{k}, \mathbf{g}_j)}{\sqrt{\sum_{j, \beta} |\mathcal{F}^{\beta, \alpha}(\mathbf{k}, \mathbf{g}_j)|^2}} \quad (\text{S.C71})$$

for any j, β , thus solving the form of the eigen-wavefunction $|n, \mathbf{k}\rangle$. Here, we have chosen the phase factor of $\langle n, \mathbf{k} | \phi_0, \alpha \rangle$ to be zero. For $H_{mC}(\mathbf{k})$ in Eq.(S.C31), we denote the wave function of the VB1 band at the Γ point as $|VB1, \Gamma\rangle$ and the spatial distribution, namely $|\langle \mathbf{r} | VB1, \Gamma \rangle|^2$. Under the δ -function-like potential shown in Fig.S9(a) and (b) for different values of G_{Λ} can be computed and shown in Fig.S9(c) and (d). We find that, similar to the case of a free electron gas in a δ -function-like potential, the wave function $|VB1, \Gamma\rangle$ is highly localized near the Wyckoff position 1a for a large G_{Λ} .

Finally, the spectrum function $\mathcal{A}(\mathbf{k}, E)$ of the moiré Chern-band model with a periodic δ -function-like potential is defined as

$$\mathcal{A}(\mathbf{k}, E) = -\Im(\text{Tr}(G(\mathbf{k}, E + i\xi^+)))/\pi \quad (\text{S.C72})$$

with the broadening parameter ξ^+ chosen to be 5 meV for our calculations. The peak of the spectrum function $\mathcal{A}(\mathbf{k}, E)$ describes the eigen-energy spectrum of H_{mC} , which is shown in Fig.3(a) and (b) of the main text with the cutoff $G_{\Lambda} = 23|b_1^M|$.

3. Mapping to Topological heavy fermion model

The numerical calculations in Sec.C2 have demonstrated that the topological flat bands can also emerge in the Chen-band model with the periodic δ -function-like potential. Intuitively, the strong periodic δ -function-like potential induces a periodic lattice formed by the localized bound state in each moiré unit cell for the Chern-band model. Below we will numerically show this localized bound state originating from the valence band of the Chern-band model. To see that, we examine the wavefunctions of the trivial flat VB1 in Fig. 3(a) of the main text, which can be expanded as $|VB1, \mathbf{k}\rangle = \sum_{\mathbf{g}, \alpha} u_{\alpha, \mathbf{k}, \mathbf{g}} |\alpha, \mathbf{k}, \mathbf{g}\rangle$, where $u_{\alpha, \mathbf{k}, \mathbf{g}}$ is a coefficient. Recall that for $|\alpha, \mathbf{k}, \mathbf{g}\rangle$, $\alpha = 1, 2$ represents the basis functions of the Hamiltonian given in Eq.(S.C31). We project the VB1 band into the $\alpha = 2$ component, which corresponds to the valence band in the Chern-band model. The projection is defined as $P_V(\mathbf{k}) = \sum_{\mathbf{g}} |u_{2, \mathbf{k}, \mathbf{g}}|^2$. The distribution of $P_V(\mathbf{k})$ over the entire mBZ is shown in Fig.S10(b), where it exceeds 0.9 throughout. This confirms the origin of the VB1 from the valence band of the Chern-band model. These bound states will form a trivial flat band. With increasing periodic δ -function-like potential strength, the energy of this flat band is increased and can be higher than the conduction band bottom at Γ , leading to band inversion due to the different irreps of the states between the valence band top and conduction band bottom of the Chern-band model. In this section, we will first provide an approximate analytical solution for the bound states of the valence band due to the periodic δ -function-like

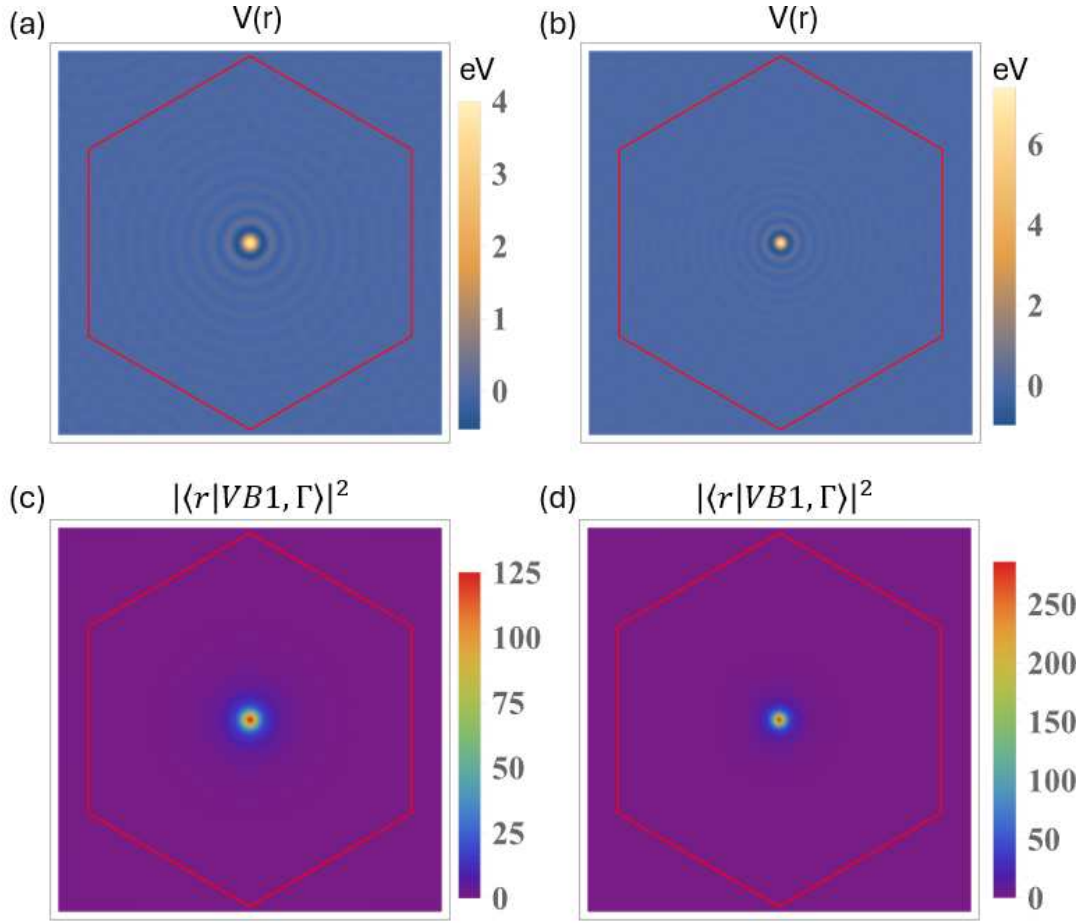


FIG. S9: (a)-(b) $V(r)$ with $\Delta_0=3.85$ meV at $G_\Lambda=17|b_1^M|$ and $23|b_1^M|$. (c)-(d) $|\langle r|VB1, \Gamma \rangle|^2$ with $\Delta_0=3.85$ meV at $G_\Lambda=17|b_1^M|$ and $23|b_1^M|$.

potential and then construct the THF model based on this analytical solution and the conduction band of the moiré Chern-band model.

We start from the moiré Chern-band Hamiltonian H_{mC} with periodic δ -function-like potential and the Hamiltonian form in the momentum space is given in Eq.(S.C31). For convenience of implementing the perturbation theory, we first rewrite H_{mC} into the form

$$H_{mC}(\mathbf{k}) = \begin{pmatrix} H_+(\mathbf{k}) & H_{+-}(\mathbf{k}) \\ H_{+-}^\dagger(\mathbf{k}) & H_-(\mathbf{k}) \end{pmatrix}, \quad (\text{S.C73})$$

where

$$H_\pm(\mathbf{k}) = \begin{pmatrix} F_\pm(\mathbf{k} + \mathbf{g}_1) & 0 & \dots & 0 \\ 0 & F_\pm(\mathbf{k} + \mathbf{g}_2) & \dots & 0 \\ \vdots & \vdots & \ddots & \vdots \\ 0 & 0 & \dots & F_\pm(\mathbf{k} + \mathbf{g}_{N_g}) \end{pmatrix} + N_g \Delta_0 P_0 \quad (\text{S.C74})$$

with $F_\pm(\mathbf{k}) = \epsilon(\mathbf{k}) \pm \mathcal{M}(\mathbf{k})$, $\mathcal{M}(\mathbf{k}) = M + Bk^2$, $\epsilon(\mathbf{k}) = Dk^2$ and the projection operator P_0 is given in Eq.(S.C7). The first term in $H_\pm(\mathbf{k})$ is diagonal. The Hamiltonian matrix $H_{+-}(\mathbf{k})$ is given by

$$H_{+-}(\mathbf{k}) = \begin{pmatrix} A(k_+ + (\mathbf{g}_1)_+) & 0 & \dots & 0 \\ 0 & A(k_+ + (\mathbf{g}_2)_+) & \dots & 0 \\ \vdots & \vdots & \ddots & \vdots \\ 0 & 0 & \dots & A(k_+ + (\mathbf{g}_{N_g})_+) \end{pmatrix} \quad (\text{S.C75})$$

with $k_{\pm} = k_x \pm ik_y$ and $(\mathbf{g}_j)_{\pm} = g_{j,x} \pm ig_{j,y}$ for different j values. Below, we will set the moiré reciprocal lattice vector $\mathbf{g}_1 = \mathbf{0}$.

From the above numerical calculations of the wave function from Eq.(S.C69), we know that the c-electrons should mainly come from the first diagonal matrix element $F_+(\mathbf{k} + \mathbf{g}_1) = F_+(\mathbf{k})$ in the block $H_+(\mathbf{k})$, while the f-electron is mainly from the block $H_-(\mathbf{k})$. Since c-electrons should weakly depend on moiré potential for $\Delta_0 > 0$, we make the approximation of neglecting the $N_g\Delta_0 P_0$ terms in $H_+(\mathbf{k})$ of Eq.(S.C74) below, which corresponds to the moiré potential appearing only in layer B, but not in layer A. The Hamiltonian $H_{mC}(\mathbf{k})$ is rewritten into the form

$$H_{mC}(\mathbf{k}) = \begin{pmatrix} H_c(\mathbf{k}) & \tilde{H}_{cf}(\mathbf{k}) \\ \tilde{H}_{cf}^\dagger(\mathbf{k}) & \tilde{H}_f(\mathbf{k}) \end{pmatrix}, \quad (\text{S.C76})$$

$$H_c(\mathbf{k}) = F_+(\mathbf{k} + \mathbf{g}_1 = \mathbf{k}) + \Delta_0 \quad (\text{S.C77})$$

$$\tilde{H}_{cf}(\mathbf{k}) = (0 \ \dots \ 0 \ Ak_+ \ 0 \ \dots \ 0), \quad (\text{S.C78})$$

where H_{cf} is a $1 \times (2N_g - 1)$ vector with the only non-zero component Ak_+ appearing at the position $(1, N_g)$, and

$$\tilde{H}_f(\mathbf{k}) = \begin{pmatrix} \tilde{H}_+(\mathbf{k}) & \tilde{H}_{+-}(\mathbf{k}) \\ \tilde{H}_{+-}^\dagger(\mathbf{k}) & H_-(\mathbf{k}) \end{pmatrix} \quad (\text{S.C79})$$

where

$$\tilde{H}_+(\mathbf{k}) = \begin{pmatrix} F_+(\mathbf{k} + \mathbf{g}_2) & \dots & 0 \\ \vdots & \ddots & \vdots \\ 0 & \dots & F_+(\mathbf{k} + \mathbf{g}_{N_g}) \end{pmatrix}_{(N_g-1) \times (N_g-1)}, \quad (\text{S.C80})$$

$$\tilde{H}_{+-}(\mathbf{k}) = \begin{pmatrix} 0 & A(k_+ + (\mathbf{g}_2)_+) & \dots & 0 \\ \vdots & \vdots & \ddots & \vdots \\ 0 & 0 & \dots & A(k_+ + (\mathbf{g}_{N_g})_+) \end{pmatrix}_{(N_g-1) \times N_g}. \quad (\text{S.C81})$$

Now we want to apply the quasi-degenerate perturbation theory (also known as Löwdin perturbation theory) [19] to the Hamiltonian $\tilde{H}_f(\mathbf{k})$ around Γ above. We divide the whole basis wavefunctions into two subsets \mathcal{A} and \mathcal{B} , which include the basis wavefunctions for $H_-(\mathbf{k})$ and $\tilde{H}_+(\mathbf{k})$, respectively. We hope to project out $\tilde{H}_+(\mathbf{k})$ in $\tilde{H}_f(\mathbf{k})$ and thus divide the whole Hamiltonian $\tilde{H}_f(\mathbf{k})$ into three parts,

$$\tilde{H}_f = H^0 + H^1 + H^2 \quad (\text{S.C82})$$

where

$$H^0 = \begin{pmatrix} F_+(\mathbf{k} + \mathbf{g}_2) & \dots & 0 & 0 & 0 & \dots & 0 \\ \vdots & \ddots & \vdots & \vdots & \vdots & \ddots & \vdots \\ 0 & \dots & F_+(\mathbf{k} + \mathbf{g}_{N_g}) & 0 & \dots & \dots & \dots \\ 0 & \dots & 0 & F_-(\mathbf{k}) + \Delta_0 & 0 & \dots & 0 \\ 0 & \dots & 0 & 0 & F_-(\mathbf{k} + \mathbf{g}_2) + \Delta_0 & \dots & 0 \\ \vdots & \ddots & \vdots & \vdots & \vdots & \ddots & \vdots \\ 0 & \dots & 0 & 0 & 0 & \dots & F_-(\mathbf{k} + \mathbf{g}_{N_g}) + \Delta_0 \end{pmatrix}$$

$$H^1 = \begin{pmatrix} \mathbf{0}_{(N_g-1) \times (N_g-1)} & \mathbf{0}_{(N_g-1) \times 1} & \mathbf{0}_{(N_g-1) \times 1} & \dots & \mathbf{0}_{(N_g-1) \times 1} \\ \mathbf{0}_{1 \times (N_g-1)} & 0 & \Delta_0 & \dots & \Delta_0 \\ \mathbf{0}_{1 \times (N_g-1)} & \Delta_0 & 0 & \dots & \Delta_0 \\ \vdots & \vdots & \vdots & \ddots & \vdots \\ \mathbf{0}_{1 \times (N_g-1)} & \Delta_0 & \Delta_0 & \dots & 0 \end{pmatrix}$$

$$H^2 = \begin{pmatrix} \mathbf{0}_{(N_g-1) \times (N_g-1)} & \tilde{H}_{+-}(\mathbf{k}) \\ \tilde{H}_{+-}^\dagger(\mathbf{k}) & \mathbf{0}_{N_g \times N_g} \end{pmatrix}. \quad (\text{S.C83})$$

Here H^0 is a diagonal matrix, H^1 includes all the off-diagonal components within subsets \mathcal{A} and \mathcal{B} and H^2 includes all the off-diagonal components between subsets \mathcal{A} and \mathcal{B} . Our aim is to remove the off-diagonal components in

H^2 perturbatively by applying the Löwdin perturbation [19]. The effective Hamiltonian for f-electron up to the second-order perturbation terms reads

$$H_f^{eff}(\mathbf{k}) = \begin{pmatrix} F_-(\mathbf{k}) + \Delta_0 & \Delta_0 & \cdots & \Delta_0 \\ \Delta_0 & F_-(\mathbf{k} + \mathbf{g}_2) + \Delta_0 & \cdots & \Delta_0 \\ \vdots & \vdots & \ddots & \vdots \\ \Delta_0 & 0 & \cdots & F_-(\mathbf{k} + \mathbf{g}_{N_g}) + \Delta_0 \end{pmatrix} + H_f^{eff(2)}(\mathbf{k}) \quad (\text{S.C84})$$

$$[H_f^{eff(2)}(\mathbf{k})]_{l'l'} = \frac{1}{2} \sum_m [\tilde{H}_{+-}^\dagger(\mathbf{k})]_{lm} [\tilde{H}_{+-}(\mathbf{k})]_{m'l'} \left(\frac{1}{F_-(\mathbf{k} + \mathbf{g}_l) - F_+(\mathbf{k} + \mathbf{g}_m)} + \frac{1}{F_-(\mathbf{k} + \mathbf{g}_{l'}) - F_+(\mathbf{k} + \mathbf{g}_m)} \right), \quad (\text{S.C85})$$

where $\tilde{H}_{+-}(\mathbf{k})_{ml} = \delta_{m+1,l} A(k_+ + (\mathbf{g}_l)_+)$ from Eq.(S.C81), so that $H_f^{eff(2)}(\mathbf{k})$ only has diagonal terms.

Based on the above discussion, we find the effective Hamiltonian

$$H_f^{eff}(\mathbf{k}) = \tilde{H}_f^0(\mathbf{k}) + \Delta_0 \begin{pmatrix} 1 & 1 & \cdots & 1 \\ 1 & 1 & \cdots & 1 \\ \vdots & \vdots & \ddots & \vdots \\ 1 & 1 & \cdots & 1 \end{pmatrix}, \quad (\text{S.C86})$$

$$\tilde{H}_{f,ij}^0(\mathbf{k}) = \delta_{i,j} E_v(\mathbf{k} + \mathbf{g}_j), \quad (\text{S.C87})$$

where $i, j = 1, \dots, N_g$ and $E_v(\mathbf{k} + \mathbf{g}_j)$ are obtained from the second order perturbation as

$$E_v(\mathbf{k} + \mathbf{g}_j) = \begin{cases} (D - B)|\mathbf{k} + \mathbf{g}_j|^2 - M - \frac{A^2|\mathbf{k} + \mathbf{g}_j|^2}{2B|\mathbf{k} + \mathbf{g}_j|^2 + 2M - \Delta_0}, & j \neq 1 \\ (D - B)\mathbf{k}^2 - M. & j = 1 \end{cases} \quad (\text{S.C88})$$

The term $\frac{A^2|\mathbf{k} + \mathbf{g}_j|^2}{2B|\mathbf{k} + \mathbf{g}_j|^2 + 2M - \Delta_0}$ is from the second order perturbation in Eq.(S.C85). Based on the above discussion, similar to Eq.(S.C22), the eigen-energy \mathcal{E}_0 of the bound states at $\mathbf{k} = \mathbf{0}$ can be solved from the equation

$$\sum_{|\mathbf{g}_j| \leq G_\Lambda} \frac{1}{\mathcal{E}_0 - E_v(\mathbf{g}_j)} = \frac{1}{\Delta_0}. \quad (\text{S.C89})$$

where G_Λ is the momentum cut-off.

We choose the parameters to make the term $B|\mathbf{k} + \mathbf{g}_j|^2$ increasing rapidly due to the small effective mass, so that we can introduce another critical value G_0 , for which $B|\mathbf{g}_j|^2 \gg |M|$ and $|\Delta_0|$ when $|\mathbf{g}_j| > G_0$. Based on this approximation, the E_v in Eq.(S.C88) can be simplified as

$$E_v(\mathbf{k} + \mathbf{g}_j) \approx (D - B)|\mathbf{k} + \mathbf{g}_j|^2 - M - \frac{A^2}{2B} \doteq \tilde{E}_v(\mathbf{k} + \mathbf{g}_j), \quad (\text{S.C90})$$

for $|\mathbf{g}_j| > G_0$. Practically, with $M = 0.1$ eV and $B = 0.706 \text{ nm}^2 \cdot \text{eV}$, we can choose $G_0 = 2|\mathbf{b}_1^M|$ with $|\mathbf{b}_1^M| = 0.63 \text{ nm}^{-1}$, so that the dimensionless quantity $\frac{BG_0^2}{M} \approx 12 \gg 1$. Under this approximation, the energy \mathcal{E}_0 of the bound state is determined by

$$\begin{aligned} \sum_{|\mathbf{g}_j| < G_0} \frac{1}{\mathcal{E}_0 - E_v(\mathbf{g}_j)} + \frac{1}{\Omega_B} \int_{G_0}^{G_\Lambda} \frac{2\pi g}{\mathcal{E}_0 - \tilde{E}_v(\mathbf{g}_j)} dg &= \frac{1}{\Delta_0} \\ \sum_{|\mathbf{g}_j| < G_0} \frac{1}{\mathcal{E}_0 - E_v(\mathbf{g}_j)} + \frac{\pi}{\Omega_B(B - D)} \ln \left(\frac{\mathcal{E}_0 - \tilde{E}_v(G_\Lambda)}{\mathcal{E}_0 - \tilde{E}_v(G_0)} \right) &= \frac{1}{\Delta_0}, \end{aligned} \quad (\text{S.C91})$$

where $g = |\mathbf{g}_j|$ and Ω_B are the area of mBZ. The energy \mathcal{E}_0 of the bound state can be numerically solved from Eq.(S.C91) and compared with the solution from Eq.(S.C63) for different cut-off G_Λ in Fig.S10(a), which shows a good agreement for a larger G_Λ . In the limit $G_\Lambda \rightarrow \infty$, the second term will diverge and thus be much larger than the

first term in the left-hand side of Eq.(S.C91), so we can drop the first term and set G_0 as 0 to get a simplified analytical expression. We further approximate the $E_v(\mathbf{g}_j)$ by $\tilde{E}_v(\mathbf{g}_j)$, so the analytical expression for \mathcal{E}_0 can be obtained as

$$\frac{\pi}{\Omega_B(B-D)} \ln \left(\frac{\mathcal{E}_0 - \tilde{E}_v(G_\Lambda)}{\mathcal{E}_0 - \tilde{E}_v(0)} \right) = \frac{1}{\Delta_0}; \quad \mathcal{E}_0 = \tilde{E}_v(0) + \frac{\tilde{E}_v(0) - \tilde{E}_v(G_\Lambda)}{-1 + e^{\frac{\Omega_B(B-D)}{\Delta_0\pi}}}. \quad (\text{S.C92})$$

Now let's denote this bound state as $|\tilde{f}\rangle$ at $\mathbf{k} = \mathbf{0}$ with eigen-energy \mathcal{E}_0 . Based on Eq.(S.C28), the eigen-wavefunction of the bound state $|\tilde{f}\rangle$ for the effective Hamiltonian $H_f^{eff}(\mathbf{k})$ in Eq.(S.C86) can be found as

$$\langle j|\tilde{f}\rangle = N_v \frac{1}{\mathcal{E}_0 - E_v(\mathbf{g}_j)}, \quad (\text{S.C93})$$

similar to Eq.(S.C27), where $N_v = \sum_j \frac{1}{\mathcal{E}_0 - E_v(\mathbf{g}_j)}$ is a normalization factor and $|j\rangle$ is the unit-vector of the non-zero \mathbf{g}_j component of $H_f^{eff}(\mathbf{k})$. To project H_{mC} in Eq.(S.C76) to the THF model, we choose the basis wavefunction for the c-electron the same as that for $H_c(\mathbf{k})$, namely

$$|c\rangle = (1, \mathbf{0}_{1 \times (2N_g - 1)})^T, \quad (\text{S.C94})$$

and the basis wavefunction for f-electrons should be given by

$$|f\rangle = (\mathbf{0}_{1 \times N_g}, \langle 1|\tilde{f}\rangle, \langle 2|\tilde{f}\rangle, \dots, \langle N_g|\tilde{f}\rangle)^T. \quad (\text{S.C95})$$

On the basis of $|c\rangle$ and $|f\rangle$, we find the Hamiltonian H_{mC} in Eq.(S.C76) can be transformed into

$$H_{HF} = \sum_{|\mathbf{k}| < \Lambda_c} (E_c + \alpha k^2) c_{\mathbf{k}}^\dagger c_{\mathbf{k}} + \sum_{\mathbf{R}} E_f f_{\mathbf{R}}^\dagger f_{\mathbf{R}} + \frac{\beta}{\sqrt{N}} \sum_{|\mathbf{k}| < \Lambda_c, \mathbf{R}} [e^{-i\mathbf{k} \cdot \mathbf{R}} (k_x + ik_y) c_{\mathbf{k}}^\dagger f_{\mathbf{R}} + h.c.], \quad (\text{S.C96})$$

where $E_c = M + \Delta_0$, $E_f = \mathcal{E}_0$, $\alpha = B + D$ and

$$\beta = \left. \frac{\partial \langle c| H_{mC}(\mathbf{k}) |f\rangle}{\partial k_x} \right|_{\mathbf{k} \rightarrow \mathbf{0}} = N_v \frac{\beta}{\mathcal{E}_0 - E_v(0)} = N_v \frac{\beta}{\mathcal{E}_0 + M}. \quad (\text{S.C97})$$

In the second equation of Eq.(S.C97), we substitute Eq.(S.C93) and Eq.(S.C94) into $|f\rangle$ and $\langle c|$. When $E_f > E_c$, the band inversion happens and VB1 becomes topological. Using the parameters for our numerical calculations, we extract all the parameters of the THF model as $E_c = 0.104$ eV, $E_f = 0.127$ eV, $\alpha = 1.238$ eV \cdot nm² and $\beta = 0.120$ eV \cdot nm. In Fig.3(b) of the main text, we find an excellent consistency for the energy dispersion between the THF model (S.C96) and the numerical solution solved from Eq.(S.C63).

D. Other candidates for Moiré heterostructures with type-II band alignment

1. 2D materials heterostructures with the type-II band alignment

In this section, we aim in searching for 2D material heterostructures with type-II band alignment and a narrow band gap. Our selection for two 2D materials, denoted as Material 1 and Material 2, to form a heterostructure is based on the following criteria:

(1) Two 2D materials should form type-II band alignment. Therefore, we extract the material information, including the conduction and valence band edge for individual materials with respect to vacuum and the lattice constants. These properties are obtained through DFT calculations using the Vienna Ab-initio Simulation Package (VASP) [29], with the HSE06 hybrid exchange-correlation functional for accurate determination of band edges [30].

(2) We search for materials with the conduction band minimum (CBM) of Material 1 and valence band maximum (VBM) of Material 2 at Γ in the atomic BZ. We only focus on the materials with Γ valley, in which the moiré potential can be generated via interfacing Material 1 or 2 with another insulating layer to form moiré heterobilayer.

(3) The irreps for CBM in Material 1 and VBM in Material 2 should be different. Particularly, we hope the angular momenta of the states at Γ between the conduction band from Material 1 and the valence band from Material 2 should be different by ± 1 , so that the linear- k coupling will be the dominant term between two materials, allowing for the occurrence of the Chern-band model. This criterion gives a strong constraint on the possible material candidates.

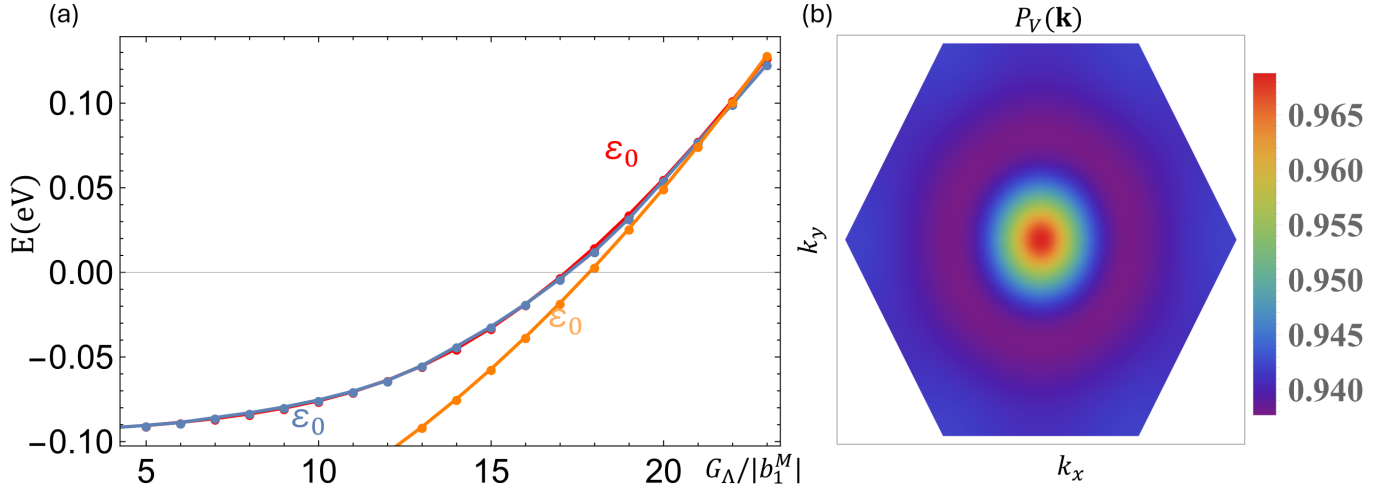


FIG. S10: (a) The solution ϵ_0 with $\Delta_0 = 4.05$ meV of Eq.(S.C91), Eq.(S.C63) and Eq.(S.C92) for different G_Λ are labeled by red, blue and orange dots respectively. These three agree with each other well in the large G_Λ . (b) The projection onto the valence band of the Chern-band model, $P_V(\mathbf{k})$, for VB1 with $\Delta_0 = 3.85$ meV and $G_\Lambda = 23|b_1^M|$.

In the example of the group $p\bar{3}m1$ discussed below, we would expect the irreps of the CBM and VBM to belong to one 1D irrep $\Gamma_{1,2}^\pm$ and one 2D irrep Γ_3^\pm , respectively.

(4) The band gap between CBM in Material 1 and VBM in Material 2 should be smaller than 0.5 eV. As we discussed in main text, in order to achieve the THF limit, we require the moiré potential Δ_0 to be larger than the atomic band gap M in the moiré Chern-band model. The generated moiré potential has a limitation in its energy scale, normally around a few hundreds of meV. Thus, we require the atomic band gap of the whole heterostructure to be smaller than 0.5 eV. It should be noted that our search here is based on the DFT calculations without SOC due to time cost consideration. When including SOC, the type-II band gap can be further reduced, as shown in the example of $\text{Tl}_2\text{Se}_2/\text{Zn}_2\text{Te}_2$ heterostructure below.

(5) The lattice mismatch between two materials should be smaller than 15%. A small lattice constant difference is expected to improve the sample quality in experiments. But this is *not* an essential condition, and materials with a large lattice constant difference can also be possible.

Based on these criteria, a class of possible 2D material hetero-structures for the groups $p\bar{3}m1$ is shown in the Tab.SIII, in which we show Material 1 belonging to the material family of $\text{Tl}_2(\text{Se},\text{Te},\text{S})_2$ with its conduction band at Γ belonging to the irrep Γ_2^- without SOC. Material 2 is selected according to the criteria discussed above. The irrep of Material 2 belongs to Γ_3^\pm . The gaps listed in the Tab.SIII describe the energy difference between the CBM from Material 1 and the VBM from Material 2 for individual compounds without SOC. When SOC is included, we anticipate that this gap will further be reduced since the SOC may split the valence band in Material 2 and thus increase the energy of the VBM. We emphasize that the energy gap in the real heterostructure will be different from the gap listed here since a charge transfer may exist between two layers and needs to be calculated directly from the DFT calculations.

2. Chern-band model from 2D material heterostructures

Below we will take the material combination of Tl_2Se_2 and Zn_2Te_2 monolayers as an example to show the low-energy physics in the material list in Tab.SIII that can be described by the Chern-band model in Eq.(S.A2) when these two 2D materials form a heterostructure. Both Tl_2Se_2 and Zn_2Te_2 belong to the space group $P\bar{3}m1$ and the corresponding wavevector group at Γ belongs to D_{3d} group with the corresponding character table shown in Tab.SIV(a). The conduction band of Tl_2Se_2 has a lower energy than that of Zn_2Te_2 , while the valence band of Zn_2Te_2 has a higher energy than that of Tl_2Se_2 . Thus, we would expect if these two materials are stacked together to form a heterostructure, the conduction band should come from Tl_2Se_2 while the valence band should originate from Zn_2Te_2 . Comparing these two 2D materials, we find the CBM of Tl_2Se_2 is around 200 meV above the VBM of Zn_2Te_2 (without SOC), so we would expect type-II band alignment with a relatively small band gap for their heterostructure. Furthermore, the conduction band in Tl_2Se_2 belongs to the 1D irrep Γ_2^- , which corresponds to the orbital angular momentum $L = 0$, while the valence band in Zn_2Te_2 belongs to the 2D irrep Γ_3^- , which corresponds to the orbital

angular momentum $L = \pm 1$.

Material 1	Lattice const. (Å)	CB edge (eV)	Material 2	Lattice const. (Å)	VB edge (eV)	Δ gap	Lattice mismatch (%)
Tl ₂ Se ₂	4.229	-5.433(Γ_2^-)	Zn ₂ Te ₂	4.33	-5.642(Γ_3^-)	0.209	2.39
Tl ₂ S ₂	4.061	-5.638(Γ_2^-)	H ₂ Si ₂	3.895	-5.658(Γ_3^+)	0.02	4.09
Tl ₂ Se ₂	4.229	-5.433(Γ_2^-)	Au ₂ I ₂	4.444	-5.801(Γ_3^-)	0.368	5.08
Tl ₂ S ₂	4.061	-5.638(Γ_2^-)	Zn ₂ Te ₂	4.33	-5.642(Γ_3^-)	0.004	6.62
Tl ₂ Se ₂	4.229	-5.433(Γ_2^-)	H ₂ Si ₂	3.895	-5.658(Γ_3^+)	0.225	7.9
Tl ₂ S ₂	4.061	-5.638(Γ_2^-)	Au ₂ I ₂	4.444	-5.801(Γ_3^-)	0.163	9.43
Tl ₂ Te ₂	4.52	-4.965(Γ_2^-)	Ge ₂ H ₂	4.077	-5.337(Γ_3^+)	0.372	9.8
Tl ₂ Se ₂	4.229	-5.433(Γ_2^-)	Cd ₂ Te ₂	4.67	-5.918(Γ_3^-)	0.485	10.43
Tl ₂ S ₂	4.061	-5.638(Γ_2^-)	Ag ₂ I ₂	4.577	-6.116(Γ_3^-)	0.478	12.71
Tl ₂ S ₂	4.061	-5.638(Γ_2^-)	Cd ₂ Te ₂	4.67	-5.918(Γ_3^-)	0.28	15

TABLE III: Candidate materials with the type-II band alignment in the space group $p\bar{3}m1$. The first to the third columns show the material providing the conduction band (CB), the corresponding lattice constant and the CB edge. The CB edge is at Γ point and the Γ_i in the parentheses is the irrep of CB for the D_{3d} point group. The fourth to the sixth columns show the material providing the valence band (VB), the corresponding lattice constant and the VB edge. The VB edge is at Γ point and the Γ_i in the parentheses is the irrep of VB for the D_{3d} group. The last two columns show the energy difference between CBM of material 1 and VBM of material 2 and the lattice mismatch between them.

D_{3d}	Γ_1^+	Γ_2^+	Γ_3^+	Γ_1^-	Γ_2^-	Γ_3^-	$\bar{\Gamma}_4^+$	$\bar{\Gamma}_5^+$	$\bar{\Gamma}_6^+$	$\bar{\Gamma}_4^-$	$\bar{\Gamma}_5^-$	$\bar{\Gamma}_6^-$
E	1	1	2	1	1	2	2	1	1	2	1	1
$2C_3$	1	1	-1	1	1	-1	-1	-1	-1	-1	-1	-1
$3C_2$	1	-1	0	1	-1	0	0	i	$-i$	0	i	$-i$
I	1	1	2	-1	-1	-2	2	1	1	-2	-1	-1
$2IC_3$	1	1	-1	-1	-1	-1	1	-1	-1	-1	1	1
$3IC_2$	1	-1	0	-1	1	0	0	i	$-i$	0	$-i$	i

(a)

C_{3v}	Γ_1	Γ_2	Γ_3	$\bar{\Gamma}_4$	$\bar{\Gamma}_5$	$\bar{\Gamma}_6$
E	1	1	2	2	1	1
$2C_3$	1	1	-1	1	-1	-1
$3IC_2$	1	-1	0	0	i	$-i$

(b)

TABLE IV: Character tables for the point groups D_{3d} and C_{3v} in (a) and (b), respectively. The irreps with a bar denote double (spinful) representations, while those without a bar correspond to single (spinless) representations.

Spin-orbit coupling (SOC) has not been included in Tab. III (a). Since SOC in Zn₂Te₂ is expected to split the bands with orbital angular momentum $L = \pm 1$ into the $J_z = \pm 1/2$ bands and $J_z = \pm 3/2$ bands where J_z is the z -directional total angular momentum that includes both orbital angular momentum and spin. For the Tl₂Se₂/Zn₂Te₂ heterostructure, the inversion symmetry in the D_{3d} group is broken and the remaining symmetry operations form an C_{3v} group. According to the compatibility relation, the Γ_2^- and Γ_3^- irreps of D_{3d} group for the conduction of Tl₂Se₂ and valence band of Zn₂Te₂ correspond to the Γ_1 and Γ_3 irreps in C_{3v} group, respectively, whose character table is shown in Tab. IV (b). Thus, we will below construct the effective Hamiltonian of the Tl₂Se₂/Zn₂Te₂ heterostructure based on the irreps of the C_{3v} group. Without spin, we would expect a spinless three-band model with the 1D Γ_1 irrep for the conduction band and the 2D Γ_3 irrep for the valence band. Including spin and SOC will lead to a six-band model, which has a general form

$$H_{3b,hetero}(\mathbf{k}) = \sum_{i=0}^3 \sum_{j=0}^8 F^{ij}(\mathbf{k}) \sigma_i \lambda_j, \quad (\text{S.D1})$$

where the expansion coefficients $F^{ij}(\mathbf{k})$ are the polynomials of \mathbf{k} , σ_0 and $\sigma_{1,2,3}$ are the 2×2 identity and Pauli matrices in the spin basis, while λ_0 and $\lambda_i (i = 1, \dots, 8)$ are the 3×3 identity and the Gell-Mann matrices [31] in the orbital

basis with the Γ_1 and Γ_3 irreps. The Gell-Mann matrices are defined by

$$\begin{aligned}\lambda_1 &= \begin{pmatrix} 0 & 1 & 0 \\ 1 & 0 & 0 \\ 0 & 0 & 0 \end{pmatrix}, & \lambda_2 &= \begin{pmatrix} 0 & -i & 0 \\ i & 0 & 0 \\ 0 & 0 & 0 \end{pmatrix}, & \lambda_3 &= \begin{pmatrix} 1 & 0 & 0 \\ 0 & -1 & 0 \\ 0 & 0 & 0 \end{pmatrix}, \\ \lambda_4 &= \begin{pmatrix} 0 & 0 & 1 \\ 0 & 0 & 0 \\ 1 & 0 & 0 \end{pmatrix}, & \lambda_5 &= \begin{pmatrix} 0 & 0 & -i \\ 0 & 0 & 0 \\ i & 0 & 0 \end{pmatrix}, & \lambda_6 &= \begin{pmatrix} 0 & 0 & 0 \\ 0 & 0 & 1 \\ 0 & 1 & 0 \end{pmatrix}, \\ \lambda_7 &= \begin{pmatrix} 0 & 0 & 0 \\ 0 & 0 & -i \\ 0 & i & 0 \end{pmatrix}, & \lambda_8 &= \frac{1}{\sqrt{3}} \begin{pmatrix} 1 & 0 & 0 \\ 0 & 1 & 0 \\ 0 & 0 & -2 \end{pmatrix}, & \lambda_0 &= \begin{pmatrix} 1 & 0 & 0 \\ 0 & 1 & 0 \\ 0 & 0 & 1 \end{pmatrix}\end{aligned}\quad (\text{S.D2})$$

on the orbital basis $\{|L = 0\rangle, |L = 1\rangle, |L = -1\rangle\}$, where the $L = 0$ state belongs the Γ_1 irrep and is from the Te_2Se_2 layer while the $L = \pm 1$ states belong to Γ_3 state and are from the Zn_2Te_2 layer. The C_{3v} group includes two generators, the three-fold rotation C_{3z} along the z axis and the mirror-y symmetry M_y . Under the spin and orbital basis, the σ and λ matrices transform as

$$D(C_{3z}^s)\sigma_i D^{-1}(C_{3z}^s) = \sum_j \mathcal{D}^{ji}(C_{3z}^s)\sigma_j; D(C_{3z}^o)\lambda_i D^{-1}(C_{3z}^o) = \sum_j \mathcal{D}^{ji}(C_{3z}^o)\lambda_j, \quad (\text{S.D3})$$

$$D(M_y^s)\sigma_i D^{-1}(M_y^s) = \sum_j \mathcal{D}^{ji}(M_y^s)\sigma_j; D(M_y^o)\lambda_i D^{-1}(M_y^o) = \sum_j \mathcal{D}^{ji}(M_y^o)\lambda_j. \quad (\text{S.D4})$$

Here $D(C_{3z}^s)$, $D(C_{3z}^o)$ are representation matrices of spin and orbital parts of C_{3z} , respectively, and given by

$$D(C_{3z}^s) = \begin{pmatrix} e^{-i\frac{\pi}{3}} & 0 \\ 0 & e^{i\frac{\pi}{3}} \end{pmatrix}; D(C_{3z}^o) = \begin{pmatrix} 1 & 0 & 0 \\ 0 & e^{-i\frac{2\pi}{3}} & 0 \\ 0 & 0 & e^{i\frac{2\pi}{3}} \end{pmatrix}, \quad (\text{S.D5})$$

while $D(M_y^s)$, $D(M_y^o)$ are representation matrices of spin and orbital parts of M_y respectively,

$$D(M_y^s) = \begin{pmatrix} 0 & 1 \\ -1 & 0 \end{pmatrix}; D(M_y^o) = \begin{pmatrix} 1 & 0 & 0 \\ 0 & 0 & 1 \\ 0 & 1 & 0 \end{pmatrix}. \quad (\text{S.D6})$$

Using these representation matrices of C_{3z} and M_y , we can compute the transformation matrices \mathcal{D} , from which we can classify the σ and λ matrices into the irrep table of the C_{3v} group, as shown in Table SV. To simplify the notation, we make the linear combinations of λ matrices to introduce Λ matrices as

$$\begin{aligned}\Lambda_1 &= \frac{1}{\sqrt{2}}(\lambda_1 + \lambda_4) = \frac{1}{\sqrt{2}} \begin{pmatrix} 0 & 1 & 1 \\ 1 & 0 & 0 \\ 1 & 0 & 0 \end{pmatrix}, & \Lambda_2 &= \frac{1}{\sqrt{2}}(\lambda_2 - \lambda_5) = \frac{1}{\sqrt{2}} \begin{pmatrix} 0 & -i & i \\ i & 0 & 0 \\ -i & 0 & 0 \end{pmatrix}, \\ \Lambda_3 &= \frac{1}{\sqrt{2}}(\lambda_2 + \lambda_5) = \frac{1}{\sqrt{2}} \begin{pmatrix} 0 & -i & -i \\ i & 0 & 0 \\ i & 0 & 0 \end{pmatrix}, & \Lambda_4 &= \frac{1}{\sqrt{2}}(\lambda_4 - \lambda_1) = \frac{1}{\sqrt{2}} \begin{pmatrix} 0 & -1 & 1 \\ -1 & 0 & 0 \\ 1 & 0 & 0 \end{pmatrix} \\ \Lambda_5 &= \frac{1}{2}(\sqrt{3}\lambda_3 + \lambda_8) = \frac{1}{\sqrt{3}} \begin{pmatrix} 2 & 0 & 0 \\ 0 & -1 & 0 \\ 0 & 0 & -1 \end{pmatrix}, & \Lambda_6 &= \frac{1}{2}(\lambda_3 - \sqrt{3}\lambda_8) = \begin{pmatrix} 0 & 0 & 0 \\ 0 & -1 & 0 \\ 0 & 0 & 1 \end{pmatrix} \\ \Lambda_7 &= \lambda_6 & \Lambda_8 &= \lambda_7 & \Lambda_0 &= \lambda_0.\end{aligned}\quad (\text{S.D7})$$

In the Table SV, the first column shows the irrep, the second and third columns show the construction of the representation matrices using Λ and σ matrices, respectively, and the last column shows the construction of representations using k -polynomials up to the k^2 order. The \pm signs in parentheses after the representation matrices and k -polynomials show their parity under TR.

Using the representation matrices and k -polynomials in Table SV, we can construct all the symmetry-invariant terms around $\mathbf{k} = 0$ for the C_{3v} group order by order in the momentum \mathbf{k} . Here we only keep the terms up to the

C_{3v}	Λ	σ	k
$\Gamma_1(A_1)$	$\Lambda_0(+), \Lambda_5(+)$	$\sigma_0(+)$	$k_x^2 + k_y^2(+), C(+)$
$\Gamma_2(A_2)$	$\Lambda_6(-)$	$\sigma_3(-)$	higher order
$\Gamma_3(E)$	$(\Lambda_7, \Lambda_8)(+)(\Lambda_1, \Lambda_2)(+), (\Lambda_3, \Lambda_4)(-)$	$(\sigma_2, \sigma_1)(-)$	$(k_x, -k_y)(-), (k_x^2 - k_y^2, 2k_x k_y)(+)$

TABLE SV: The classification of the representation matrices and k -polynomials for the C_{3v} group. Here Λ matrices are in orbital basis and σ matrices are in the spin basis. The + or - in the bracket indicates how the matrices transform under TR (even or odd). The symbol C in the column of k -polynomial is for a constant.

k^2 order for the spin-independent terms (σ_0) and the linear \mathbf{k} order for spin-orbit coupling terms, and obtain the effective Hamiltonian around Γ point as

$$\begin{aligned}
H_{3b,hetero}(\mathbf{k}) = & \left[\frac{1}{3}(E_1 + A_1 k^2) + \frac{2}{3}(E_2 + A_2 k^2) \right] \sigma_0 \Lambda_0 + \left[\frac{1}{\sqrt{3}}(E_1 + A_1 k^2) - \frac{1}{\sqrt{3}}(E_2 + A_2 k^2) \right] \sigma_0 \Lambda_5 \\
& + \sqrt{2} B_0 (k_x \sigma_0 \Lambda_3 - k_y \sigma_0 \Lambda_4) + \sqrt{2} B_1 [(k_x^2 - k_y^2) \sigma_0 \Lambda_1 + 2k_x k_y \sigma_0 \Lambda_2] + B_2 [(k_x^2 - k_y^2) \sigma_0 \Lambda_7 + 2k_x k_y \sigma_0 \Lambda_8] \\
& - \Delta_{SOC} \sigma_3 \Lambda_6 + \sqrt{2} \Delta_{Inter} (\sigma_2 \Lambda_3 + \sigma_1 \Lambda_4) + R_2 (\sigma_3 \Lambda_7 k_y + \sigma_3 \Lambda_8 k_x) + R_3 (\sigma_3 \Lambda_1 k_y + \sigma_3 \Lambda_2 k_x) \\
& + \frac{1}{3} R_0 \left[\sigma_2 (\Lambda_0 + \sqrt{3} \Lambda_5) k_x - \sigma_1 (\Lambda_0 + \sqrt{3} \Lambda_5) k_y \right] + \frac{2}{3} R_1 \left[\sigma_2 (\Lambda_0 - \frac{\sqrt{3}}{2} \Lambda_5) k_x - \sigma_1 (\Lambda_0 - \frac{\sqrt{3}}{2} \Lambda_5) k_y \right], \quad (S.D8)
\end{aligned}$$

where $E_1, E_2, A_1, A_2, B_0, B_1, B_2$ are material dependent parameters independent of spin, Δ_{SOC} and Δ_{Inter} describe the \mathbf{k} -independent SOC terms, R_0 and R_1 terms are Rashba SOC in TI_2Se_2 and Zn_2Te_2 layers, respectively, and the R_2 and R_3 terms are spin-dependent hopping terms connected to out-of-plane spin (σ_3).

To project the above Hamiltonian to the Chern-band model, we will below ignore the interlayer SOC term $\Delta_{inter}(\sigma_2 \Lambda_3 + \sigma_1 \Lambda_4)$, \mathbf{k} -dependent SOC terms and the off-diagonal \mathbf{k}^2 terms (B_1 and B_2 terms), which are expected to be small, so the effective 6-bands model becomes block diagonal and can be written as

$$H_{3b,hetero}(\mathbf{k}) = \begin{pmatrix} H_{hetero,\uparrow}(\mathbf{k}) & 0 \\ 0 & H_{hetero,\downarrow}(\mathbf{k}) \end{pmatrix}, \quad (S.D9)$$

$$H_{3b,hetero,\uparrow}(\mathbf{k}) = \begin{pmatrix} E_1 + A_1 k^2 & iB_0(k_x + ik_y) & iB_0(k_x - ik_y) \\ -iB_0(k_x - ik_y) & E_2 + \Delta_{SOC} + A_2 k^2 & 0 \\ -iB_0(k_x + ik_y) & 0 & E_2 - \Delta_{SOC} + A_2 k^2 \end{pmatrix} \quad (S.D10)$$

$$H_{3b,hetero,\downarrow}(\mathbf{k}) = \begin{pmatrix} E_1 + A_1 k^2 & iB_0(k_x + ik_y) & iB_0(k_x - ik_y) \\ -iB_0(k_x - ik_y) & E_2 - \Delta_{SOC} + A_2 k^2 & 0 \\ -iB_0(k_x + ik_y) & 0 & E_2 + \Delta_{SOC} + A_2 k^2 \end{pmatrix}, \quad (S.D11)$$

on the basis wavefunctions $|\Gamma_1, J_z = 1/2, \uparrow\rangle$, $|\Gamma_3, J_z = 3/2, \uparrow\rangle$, $|\Gamma_3, J_z = -1/2, \uparrow\rangle$ and $|\Gamma_1, J_z = -1/2, \downarrow\rangle$, $|\Gamma_3, J_z = 1/2, \downarrow\rangle$, $|\Gamma_3, J_z = -3/2, \downarrow\rangle$ for spin up and down, respectively. Here, $E_1 > E_2$ so that for each spin block of the Hamiltonian H_{hetero} , the first component gives the conduction band with $L = 0$ while the second and third components provide the valence bands with $L = \pm 1$. We focus on the spin up block $H_{hetero,\uparrow}$. If $\Delta_{SOC} > 0$, we would expect the $|\Gamma_3, J_z = 3/2, \uparrow\rangle$ state has a higher energy than the $|\Gamma_3, J_z = -1/2, \uparrow\rangle$ state and thus serves as the topmost valence band, so we project out the $|\Gamma_3, J_z = -1/2, \uparrow\rangle$ state and the resulting Hamiltonian on the basis $|\Gamma_1, J_z = 1/2, \uparrow\rangle, |\Gamma_3, J_z = 3/2, \uparrow\rangle$ is given by

$$H_{hetero,\uparrow}^{eff}(\mathbf{k}) = \begin{pmatrix} E_1 + A_1 k^2 + \frac{B_0^2 \mathbf{k}^2}{E_1 - E_2 + \Delta_{SOC}} & iB_0(k_x + ik_y) \\ -iB_0(k_x - ik_y) & E_2 + \Delta_{SOC} + A_2 k^2 \end{pmatrix}, \quad (S.D12)$$

which is identical to the Chern-band model in Eq.(S.A2) up to a unitary transformation.

If $\Delta_{SOC} < 0$, we can project out the $|\Gamma_3, J_z = 3/2, \uparrow\rangle$ state instead and the Hamiltonian on the basis $|\Gamma_1, J_z = 1/2, \uparrow\rangle$ and $|\Gamma_3, J_z = -1/2, \uparrow\rangle$ is

$$H_{hetero,\uparrow}^{eff}(\mathbf{k}) = \begin{pmatrix} E_1 + A_1 k^2 + \frac{B_0^2 \mathbf{k}^2}{E_1 - E_2 - \Delta_{SOC}} & iB_0(k_x - ik_y) \\ -iB_0(k_x + ik_y) & E_2 - \Delta_{SOC} + A_2 k^2 \end{pmatrix}, \quad (S.D13)$$

which still recovers the Chern-band model form Eq.(S.A2) up to a unitary transformation.

3. $\text{Ti}_2\text{Se}_2/\text{Zn}_2\text{Te}_2$ heterostructure with moiré potential

In this section, we will discuss the calculations of the flat bands in the heterostructure consisting of Ti_2Se_2 and Zn_2Te_2 when there is moiré potential on either Ti_2Se_2 layer of Zn_2Te_2 layer.

We first consider a heterostructure with the lattice constant of Ti_2Se_2 being relaxed to match that of Zn_2Te_2 , so that no moiré pattern is formed between Ti_2Se_2 and Zn_2Te_2 layers, and we can directly perform the DFT calculation for the heterostructure (See Fig.4 in the main text). From the DFT calculations, we find the conduction band in the $\text{Ti}_2\text{Se}_2/\text{Zn}_2\text{Te}_2$ heterostructure shows a strong Rashba-type of spin splitting from the SOC (See Fig.4(c) in the main text) while the valence band has negligible spin splitting around $\mathbf{k} = 0$. To take into account the Rashba-type of spin splitting, we need to consider \mathbf{k} -dependent intra-layer SOC terms in Eq.(S.D8), namely the R_0, R_1, R_2 terms, while the inter-layer SOC terms, namely the Δ_{Inter} and R_3 terms, are dropped. We project out the $|\Gamma_3, J_z = -1/2, \uparrow\rangle$ and $|\Gamma_3, J_z = 1/2, \downarrow\rangle$ with the second order perturbation theory and reduce the effective 6-bands model to 4-bands model, which reads

$$H_{hetero}(\mathbf{k}) = \begin{pmatrix} H_{hetero}^{\uparrow\uparrow}(\mathbf{k}) & H_{hetero}^{\uparrow\downarrow}(\mathbf{k}) \\ (H_{hetero}^{\uparrow\downarrow}(\mathbf{k}))^\dagger & H_{hetero}^{\downarrow\downarrow}(\mathbf{k}) \end{pmatrix}, \quad (\text{S.D14})$$

where $H_{hetero}^{\uparrow(\downarrow)}(\mathbf{k})$ is the spin up (down) block with the same form as Eq.(S.D12). Here we keep the terms up to k^2 order for the diagonal terms and k -linear order for the off-diagonal terms, so that the Hamiltonian can be rewritten as

$$\begin{aligned} H_{hetero}^{\uparrow\uparrow}(\mathbf{k}) &= \begin{pmatrix} E_1 + \tilde{A}_1 k^2 & iB_0(k_x + ik_y) \\ -iB_0(k_x - ik_y) & \tilde{E}_2 + A_2 k^2 \end{pmatrix}, \\ H_{hetero}^{\downarrow\downarrow}(\mathbf{k}) &= (H_{hetero}^{\uparrow\uparrow}(-\mathbf{k}))^* \end{aligned} \quad (\text{S.D15})$$

on the basis wavefunctions of $|\Gamma_1, J_z = 1/2, \uparrow\rangle|\Gamma_3, J_z = 3/2, \uparrow\rangle$ for $H_{hetero}^{\uparrow\uparrow}(\mathbf{k})$ and $|\Gamma_1, J_z = -1/2, \downarrow\rangle|\Gamma_3, J_z = -3/2, \downarrow\rangle$ for $H_{hetero}^{\downarrow\downarrow}(\mathbf{k})$, where $\tilde{A}_1 = A_1 + \frac{B_0^2}{E_1 - E_2 + \Delta_{SOC}}$, $\tilde{E}_2 = E_2 + \Delta_{SOC}$ and E_1, A_2, B_0 are the same as those in Eq.(S.D9)-Eq.(S.D11). $H_{hetero}^{\uparrow\downarrow}(\mathbf{k})$ describes the lowest order \mathbf{k} -dependent SOC with the Rashba-type of SOC form for the conduction band,

$$H_{hetero}^{\uparrow\downarrow}(\mathbf{k}) = \begin{pmatrix} -iR_0 k_- & 0 \\ 0 & 0 \end{pmatrix}. \quad (\text{S.D16})$$

By choosing the parameters $E_2 = -E_1 = 0.0649\text{eV}$, $A_1 = 0.9 a_0^2 \cdot \text{eV}$, $A_2 = -0.896 a_0^2 \cdot \text{eV}$, $B_0 = 0.21 a_0 \cdot \text{eV}$ and $R_0 = 0.168 a_0 \cdot \text{eV}$ with $a_0 = 4.32\text{\AA}$ as the lattice constant of the heterostructure, the effective model can fit the band dispersions from the DFT calculations in the energy range from -0.1 eV to 0.1 eV , as shown in Fig.4(c) in the main text. We note a strong Rashba-type spin splitting existing in the conduction band, but not in the valence band. This is because of different total angular momentum between the conduction bands with $J_z = \pm 1/2$ and the valence bands with $J_z = \pm 3/2$.

Next we will introduce the moiré potential into the $\text{Ti}_2\text{Se}_2/\text{Zn}_2\text{Te}_2$ hetero-structure, which can be generally induced by interfacing either Ti_2Se_2 or Zn_2Te_2 with another insulating layer. Due to the strong Rashba-type of SOC in the conduction band, but not in the valence band, the effect of introducing the moiré potential into the Ti_2Se_2 layer will be completely different from that in the Zn_2Te_2 layer.

We first consider introducing moiré superlattice potential to the Ti_2Se_2 layer, and the whole system is described by the Hamiltonian

$$\hat{H} = \hat{H}_{hetero} + \hat{H}_m, \quad (\text{S.D17})$$

where

$$\hat{H}_{hetero} = \sum_{\mathbf{k}\alpha\beta} a_{\alpha\mathbf{k}}^\dagger [H_{hetero}(\mathbf{k})]_{\alpha\beta} a_{\beta\mathbf{k}}, \quad (\text{S.D18})$$

with $H_{hetero}(\mathbf{k})$ given in Eq.(S.D14) and the basis index $\alpha, \beta = 1, 2, 3, 4$, and the moiré potential at the Ti_2Se_2 layer is given by

$$\hat{H}_m = \sum_{\alpha=1,3} \int d^2r a_{\alpha\mathbf{r}}^\dagger H_m^{\alpha\alpha}(\mathbf{r}) a_{\alpha\mathbf{r}}, \quad (\text{S.D19})$$

and with the first shell approximation, we have $H_m^{\alpha\alpha}(\mathbf{r}) = \sum_{\mathbf{g} \in \mathbf{G}_M^1} \Delta_0 e^{i\mathbf{g}\cdot\mathbf{r}} (\delta_{\alpha,1} + \delta_{\alpha,3})$. In the current basis, $\alpha = 1, 3$ is for conduction bands in TI_2Se_2 layer and $\alpha = 2, 4$ is for valence bands in Zn_2Te_2 layer. Here, we take Δ_0 as a tuning parameter, which is chosen to be a negative value $\Delta_0 < 0$ to introduce bound states for the conduction band, instead of the valence band. The moiré lattice constant a_0^M for the calculation is 24.75 nm . The dispersions with different Δ_0 are shown in Fig.S11(a)-(d). When $\Delta_0 = -0.01 \text{ eV}$, the conduction bands CB1 originating from TI_2Se_2 are trivial and have a bandwidth of approximately 6 meV, as shown in Fig.S11(a). This is due to the strong spin splitting that originates from strong Rashba-type of SOC for a small moiré potential strength. With increasing Δ_0 , we find the energy of CB1 is lowered and the spin splitting is also suppressed, so that the corresponding bandwidth decreases, as illustrated in Fig.S11(b) for $\Delta_0 = -0.03 \text{ eV}$. For $\Delta_0 \approx -0.0445 \text{ eV}$, we find the CB1 touches the valence band top at $\mathbf{\Gamma}$, leading to band inversion in Fig.S11(c). After the band inversion, the CB1 becomes topologically non-trivial while its bandwidth remains small, thus realizing topologically nontrivial flat bands depicted in Fig.S11(d). The Wannier function flow of CB1 in Fig.S11(d) is presented in Fig.4(e) of the main text. Similar to the calculation in Sec.B 1, the topology of VB1 can be tuned by the atomic gap M . The band dispersions with a fixed Δ_0 and different M values are shown in Fig.S12. From Fig.S12(a) to (c), as M decreases, the CB1 evolves from trivial to topological bands, for a fixed Δ_0 .

We next add the moiré potential to the Zn_2Te_2 layer, so that the moiré Hamiltonian $H_m^{\alpha\alpha}(\mathbf{r})$ in Eq.(S.D19) reads

$$H_m^{\alpha\alpha}(\mathbf{r}) = \sum_{\mathbf{g} \in \mathbf{G}_M^1} \Delta_0 e^{i\mathbf{g}\cdot\mathbf{r}} (\delta_{\alpha,2} + \delta_{\alpha,4}), \quad (\text{S.D20})$$

within the first shell approximation. We choose $\Delta_0 > 0$ to induce bound states for the valence band in Zn_2Te_2 layer. The band dispersions with different Δ_0 are shown in Fig.S13(a)-(f). When $\Delta_0 = 0.02 \text{ eV}$, the top valence mini-bands VB1 originating from the Zn_2Te_2 layer are trivial and have a bandwidth of approximately 5 meV, as shown in Fig.S13(a). As Δ_0 increases, VB1 are pushed upward in energy, as shown in Fig.S13(b) and (c) for $\Delta_0 = 0.03 \text{ eV}$ and 0.04 eV , respectively. We also notice that when the VB1 approaches the conduction band bottom, the spin splitting of the VB1 becomes more pronounced, leading to an enhancement of bandwidth for VB1 in Fig.S13(b) and (c). At $\Delta_0 = 0.05 \text{ eV}$, the VB1 touch the conduction bands at the \mathbf{K} point in mBZ in Fig.S13(d), leading to a semi-metal phase for the VB1 in Fig.S13(e) for a larger $\Delta_0 = 0.054 \text{ eV}$. We slightly decrease the R_0 value of the Rashba SOC term, and find a Z_2 nontrivial insulator in Fig.S13(f), as demonstrated by the Wannier center flow of VB1 in the inset of Fig.S13(f). However, compared to the moiré potential at the TI_2Se_2 layer, the bandwidth of VB1 is significantly larger for the moiré potential at the Zn_2Te_2 layer due to the strong Rashba SOC of the conduction band.

4. Twisted TI_2Se_2 homobilayer/ Zn_2Te_2 monolayer heterostructure

In the above, we have discussed the role of moiré potential on the TI_2Se_2 or Zn_2Te_2 layers. In this section, we will consider the heterostructure consisting of twisted TI_2Se_2 homobilayer and Zn_2Te_2 monolayer, as schematically shown in Fig.S14(a). For the twisted TI_2Se_2 homobilayer with the twist angle around 1° , the primitive moiré reciprocal lattice vectors are $\mathbf{b}_1^M = (2\pi, -\frac{2\pi}{\sqrt{3}})\frac{1}{a_0^M}$, $\mathbf{b}_2^M = (0, \frac{4\pi}{\sqrt{3}})\frac{1}{a_0^M}$, where the moiré lattice constant is $a_0^M = 24.75 \text{ nm}$. The Hamiltonian for this hetero-structure takes the form

$$H = \begin{pmatrix} H_A & H_{AB} \\ H_{AB}^\dagger & H_B \end{pmatrix}, \quad (\text{S.D21})$$

where

$$H_B = \begin{pmatrix} H_{B0} + V_M(\mathbf{r})_{12 \times 2} & T_M(\mathbf{r})_{12 \times 2} \\ T_M^*(\mathbf{r})_{12 \times 2} & H_{B0} + V_M(\mathbf{r})_{12 \times 2} \end{pmatrix}, \quad (\text{S.D22})$$

with

$$\begin{aligned} H_{B0} &= (E_1 + A_1 k^2 + V_M(\mathbf{r}))_{12 \times 2} + \begin{pmatrix} 0 & -iRk_- \\ iRk_+ & 0 \end{pmatrix}; \\ H_A &= (E_2 + A_2 k^2)_{12 \times 2}; \\ H_{AB} &= \begin{pmatrix} 0 & 0 & -iB_0 k_- & 0 \\ 0 & 0 & 0 & -iB_0 k_+ \end{pmatrix}. \end{aligned} \quad (\text{S.D23})$$

Here H_A for the part A describes the Hamiltonian for the valence band in the Zn_2Te_2 layer on the basis wavefunctions $|\mathbf{\Gamma}_3, 3/2, \uparrow\rangle$ and $|\mathbf{\Gamma}_3, -3/2, \downarrow\rangle$, while the Hamiltonian H_B for the part B describes the Hamiltonian for the conduction

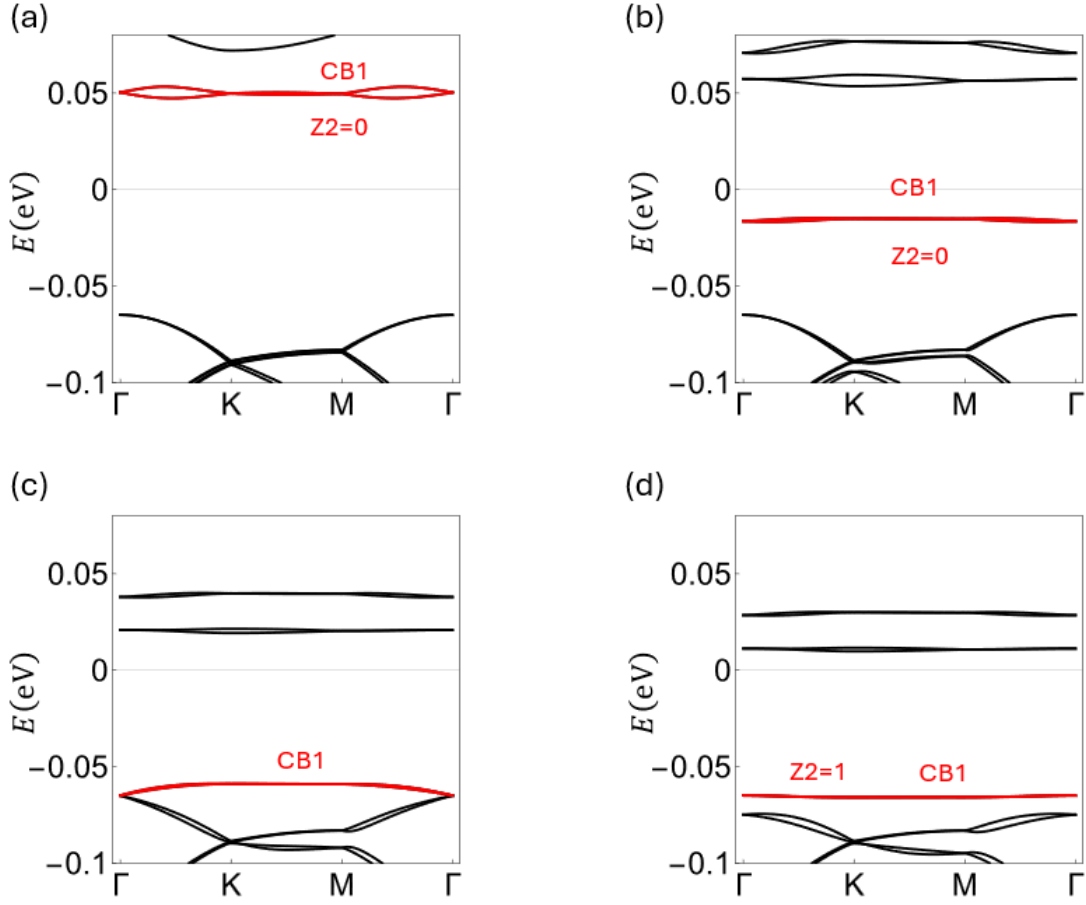


FIG. S11: (a)–(d) show the band dispersions for the $\text{Tl}_2\text{Se}_2/\text{Zn}_2\text{Te}_2$ heterojunction for $\Delta_0 = -0.01, -0.03, -0.0445,$ and -0.048 eV, respectively, with the moiré potential applied to the Tl_2Se_2 layer. We also choose the atomic gap $M=0.0649$ eV.

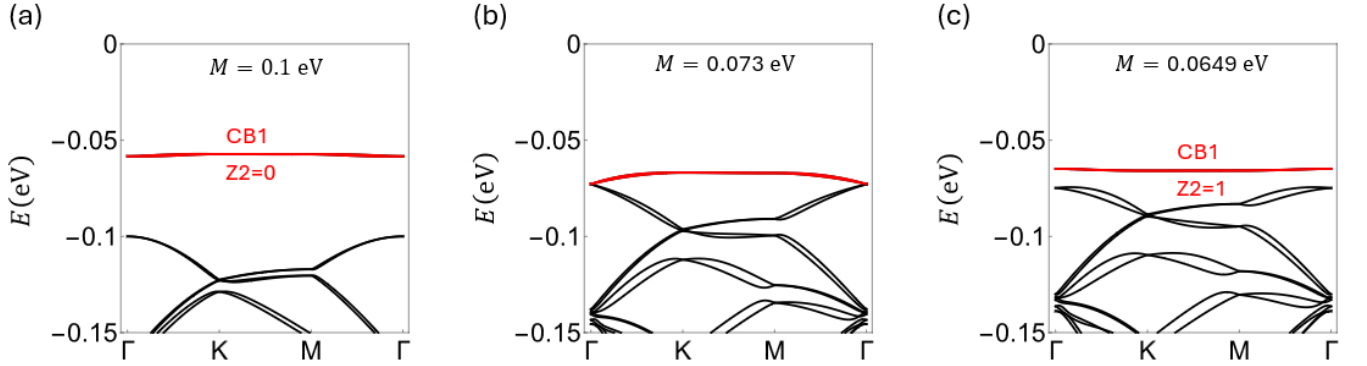


FIG. S12: (a)–(d) show the band dispersions for the $\text{Tl}_2\text{Se}_2/\text{Zn}_2\text{Te}_2$ heterojunction for the atomic gap $M = 0.1, 0.073,$ and 0.0649 eV, respectively, with the moiré potential applied to the Tl_2Se_2 layer. The moiré potential strength $\Delta_0=0.0649$ eV.

bands of the twisted Tl_2Se_2 homobilayer on the basis wavefunctions $|\Gamma_1, 1/2, \uparrow, t\rangle, |\Gamma_1, -1/2, \downarrow, t\rangle, |\Gamma_1, 1/2, \downarrow, b\rangle$ and $|\Gamma_1, -1/2, \downarrow, b\rangle$, where t and b represent the top and bottom layers, respectively. The Hamiltonian H_{AB} describes the tunneling between the parts A and B. In $H_B, T_M(\mathbf{r})$ and $V_M(\mathbf{r})$ describe the moiré tunneling between two Tl_2Se_2 layers and the moiré potential on each Tl_2Se_2 layer, respectively, and both should satisfy the symmetry of the moiré

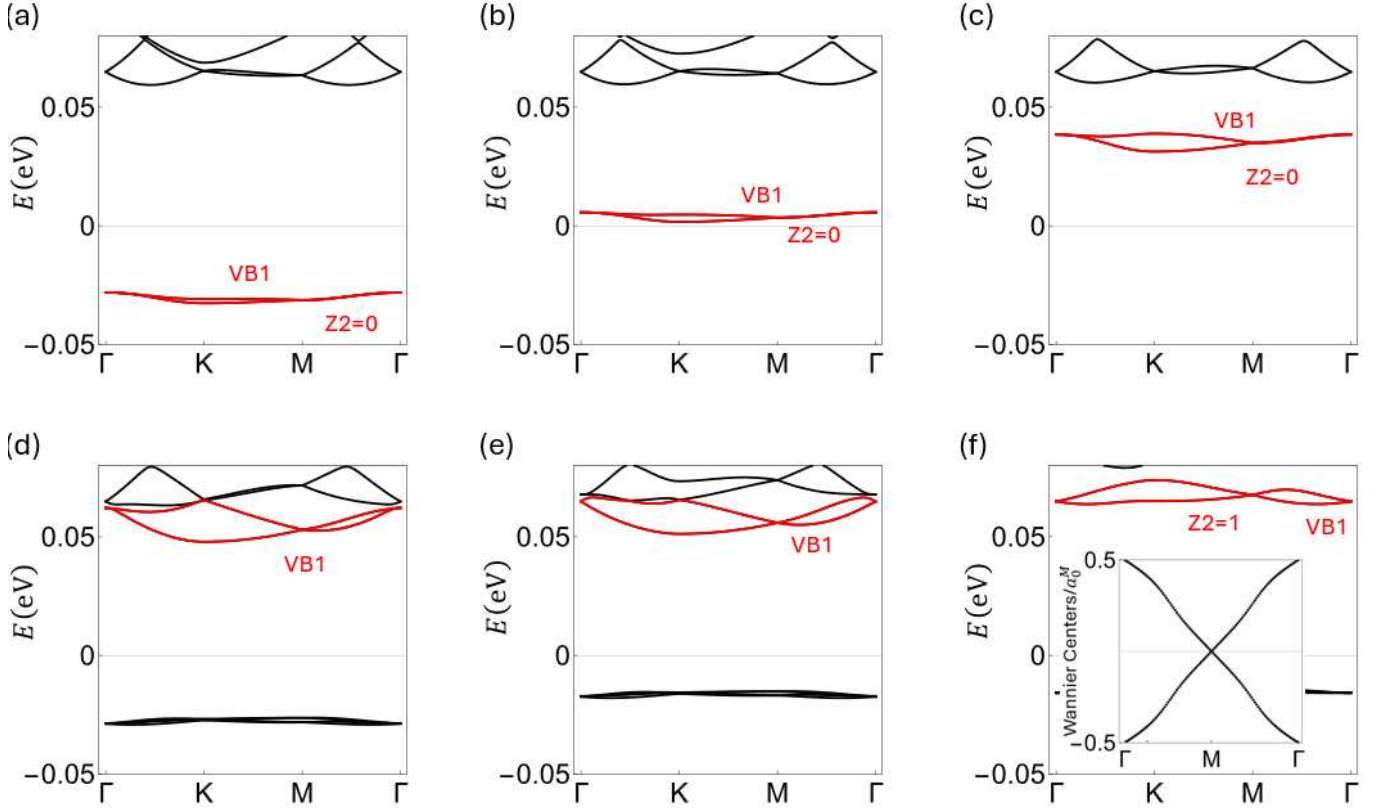


FIG. S13: (a)-(e) show the band dispersions for the $\text{Tl}_2\text{Se}_2/\text{Zn}_2\text{Te}_2$ heterojunction with $\Delta_0=0.02, 0.03, 0.04, 0.05$ and 0.054 eV, respectively, with the moiré potential applied to the Zn_2Te_2 layer. The Rashba term is $R_0 = 0.168 a_0 \cdot \text{eV}$ (f) shows the band dispersion for $\Delta_0 = 0.054 \text{eV}$, with the Rashba term reduced to $R_0 = 0.05 a_0 \cdot \text{eV}$. The inset in (f) shows the Wannier center flow of VB1.

pattern in the twisted Tl_2Se_2 bilayer. Thus, we can expand them as

$$T_{\mathbf{M}}(\mathbf{r}) = \sum_{\mathbf{g} \in \mathbf{G}_M} T_{\mathbf{M}}(\mathbf{g}) e^{i\mathbf{g} \cdot \mathbf{r}}; \quad V_{\mathbf{M}}(\mathbf{r}) = \sum_{\mathbf{g} \in \mathbf{G}_M} V_{\mathbf{M}}(\mathbf{g}) e^{i\mathbf{g} \cdot \mathbf{r}}, \quad (\text{S.D24})$$

similar to the expansion in Eq.(S.A4), where $\mathbf{G}_M = \{n_1 \mathbf{b}_1^M + n_2 \mathbf{b}_2^M | n_1, n_2 \in \mathcal{Z}\}$ includes all moiré reciprocal lattice vectors. It should be noted that since our effective model is expanded around Γ in ABZ, $\mathbf{g} = \mathbf{0}$ is included in \mathbf{G}_M , and $T_{\mathbf{M}}(\mathbf{g} = \mathbf{0})$ and $V_{\mathbf{M}}(\mathbf{g} = \mathbf{0})$ correspond to the uniform tunneling between two layers and uniform potential, respectively. The uniform potential $V_{\mathbf{M}}(\mathbf{g} = \mathbf{0})$ can be absorbed into the Fermi energy and thus we will drop $V_{\mathbf{M}}(\mathbf{g} = \mathbf{0})$ below. We denote $T_{M0} = T_{\mathbf{M}}(\mathbf{g} = \mathbf{0})$ and rewrite

$$T_{\mathbf{M}}(\mathbf{r}) = T_{M0} + \tilde{T}_{\mathbf{M}}(\mathbf{r}) = T_{M0} + \sum_{\mathbf{g} \neq \mathbf{0}} T_{\mathbf{M}}(\mathbf{g}) e^{i\mathbf{g} \cdot \mathbf{r}}, \quad (\text{S.D25})$$

where $\tilde{T}_{\mathbf{M}}(\mathbf{r})$ includes the moiré tunneling other than T_{M0} . We make the assumption that the inter-layer tunneling is dominated by the uniform part T_{M0} . This assumption has been justified in the previous studies on the moiré homobilayer systems with the low-energy atomic bands around Γ in the ABZ, as demonstrated in twisted TMD materials with Γ -valley [32, 33] and twisted ZrS_2 homobilayer[34]. We set the uniform tunneling term to be $T_{M0} = 0.08$ eV and consider the first-shell potential approximation for the moiré tunneling and moiré potential, given by $T_{\mathbf{M}}(\mathbf{g}) = \Delta_0$ and $V_{\mathbf{M}}(\mathbf{g}) = V_0$ for $\mathbf{g} \in \mathbf{G}_M^1$ and $T_{\mathbf{M}}(\mathbf{g}) = V_{\mathbf{M}}(\mathbf{g}) = 0$ for $\mathbf{g} \notin \mathbf{G}_M^1$ and $\mathbf{g} \neq \mathbf{0}$. Below, we choose $V_0 = 0$ and $\Delta_0 \ll T_{M0}$ for the numerical calculations below, so that the uniform tunneling term dominates over the moiré tunneling and moiré potential.

The band dispersions with different values of Δ_0 are shown in Fig.S14(b)-(e). When $\Delta_0 = 0.019$ eV, the CB1 originating from the conduction band of twisted Tl_2Se_2 homobilayer reveals a spin splitting and is topologically trivial, shown in Fig.S14(b). By increasing Δ_0 , the CB1 touches the valence band top and its spin splitting is

reduced, shown in Fig.S14(c). When $\Delta_0 = 0.024$ eV, the CB1 becomes topologically nontrivial and its spin splitting is negligible, thus realizing a topologically nontrivial flat band, which is demonstrated by the nontrivial winding of the Wannier center flow for CB1 in Fig.S14(f). With further increasing Δ_0 , the CB1 becomes more dispersive while remains topologically nontrivial, and behaves similarly to a valence band with a negative effective mass around Γ , as shown in Fig.S14(e). From Fig.S14(b)-(e), we find the evolution of the CB1 for twisted Tl_2Se_2 homobilayer case is quite similar to that for the case with adding moiré potential on Tl_2Se_2 layer in Fig.S11(a)-(d).

Below we will provide an analytical understanding of the similarity between these two cases using the perturbation theory. Under the assumption $T_{M0} \gg |T_M(\mathbf{g} \neq 0)|, |V_M(\mathbf{g} \neq 0)|$, we can apply a unitary transformation

$$U_0 = \frac{1}{\sqrt{2}} \begin{pmatrix} -1_{2 \times 2} & 1_{2 \times 2} \\ 1_{2 \times 2} & 1_{2 \times 2} \end{pmatrix} \quad (\text{S.D26})$$

to H_B and the resulting Hamiltonian H'_B is given by

$$\begin{aligned} H'_B &= U_0 H_B U_0^{-1} \\ &= \begin{pmatrix} H_{B0} + \left(-T_{M0} - \frac{1}{2}(\tilde{T}_M(\mathbf{r}) + \tilde{T}_M^\dagger(\mathbf{r})) + V_M(\mathbf{r}) \right) 1_{2 \times 2} & \frac{1}{2}(-\tilde{T}_M(\mathbf{r}) + \tilde{T}_M^\dagger(\mathbf{r})) 1_{2 \times 2} \\ \frac{1}{2}(\tilde{T}_M(\mathbf{r}) - \tilde{T}_M^\dagger(\mathbf{r})) 1_{2 \times 2} & H_{B0} + \left(T_{M0} + \frac{1}{2}(\tilde{T}_M(\mathbf{r}) + \tilde{T}_M^\dagger(\mathbf{r})) + V_M(\mathbf{r}) \right) 1_{2 \times 2} \end{pmatrix}. \end{aligned} \quad (\text{S.D27})$$

H'_B is written in the basis of antibonding and bonding states between two layers, where $\alpha = 1, 2$ (upper block) and $\alpha = 3, 4$ (lower block) correspond to the antibonding and bonding states, respectively. Based on the assumption of $T_{M0} \gg |T_M(\mathbf{g} \neq 0)|$, we can treat $\tilde{T}_M(\mathbf{r})$ as a perturbation, and neglect the off-diagonal terms in H'_B , since the energy difference between the diagonal terms in H'_B is dominated by $2|T_{M0}|$. The energy ordering of two bands for part B depends on the sign of T_{M0} . In the numerical calculations, T_{M0} is chosen to be positive, so that the antibonding states have lower energy for H'_B in Eq.(S.D27). After the unitary transformation U_0 , the full Hamiltonian becomes

$$H' = \begin{pmatrix} H_A & H'_{AB} \\ (H')_{AB}^\dagger & H'_B \end{pmatrix}, \quad (\text{S.D28})$$

where H_A remains the same, H'_B is given by Eq.(S.D27) and H'_{AB} after the unitary transformation is given by

$$H'_{AB} = \begin{pmatrix} -i\frac{B_0}{\sqrt{2}}k_- & 0 & -i\frac{B_0}{\sqrt{2}}k_- & 0 \\ 0 & -i\frac{B_0}{\sqrt{2}}k_+ & 0 & -i\frac{B_0}{\sqrt{2}}k_+ \end{pmatrix}. \quad (\text{S.D29})$$

For the whole moiré heterostructure, H_A for the part A is from the Zn_2Te_2 layer and provides the dispersive valence band, while H'_B for the part B is from the twisted Tl_2Se_2 homobilayer and provides the localized orbital from the conduction band, as shown in Fig. 4(e) of the main text. Thus, we need to pick out the lowest energy bands in H'_B . For $T_{M0} > 0$, the antibonding state (the upper block) in H'_B (Eq. (S.D27)) has the lowest energy and thus we project out the bonding states (lower block) in H'_B and only keep the antibonding states (upper block). The resulting four-band model Hamiltonian, which includes H_A and the upper block in H'_B , reads

$$H'_{eff} = \begin{pmatrix} H_A & H''_{AB} \\ (H''_{AB})^\dagger & H_{B0} - T_{M0} 1_{2 \times 2} + \left(-\frac{1}{2}(\tilde{T}_M(\mathbf{r}) + \tilde{T}_M^\dagger(\mathbf{r})) + V_M(\mathbf{r}) \right) 1_{2 \times 2} \end{pmatrix}, \quad (\text{S.D30})$$

where

$$H''_{AB} = \begin{pmatrix} -i\frac{B_0}{\sqrt{2}}k_- & 0 \\ 0 & -i\frac{B_0}{\sqrt{2}}k_+ \end{pmatrix}, \quad (\text{S.D31})$$

and H_A and H_{B0} take the same form as those in Eq.(S.D23). In Eq.(S.D30), one can see $-\frac{1}{2}(\tilde{T}_M(\mathbf{r}) + \tilde{T}_M^\dagger(\mathbf{r})) + V_M(\mathbf{r})$ plays the role of moiré potential for the antibonding states of the conduction bands in the twisted Tl_2Se_2 homobilayer. Thus, the Hamiltonian (S.D30) describes a dispersive valence band without any moiré potential and a conduction band with moiré potential given by $-\frac{1}{2}(\tilde{T}_M(\mathbf{r}) + \tilde{T}_M^\dagger(\mathbf{r})) + V_M(\mathbf{r})$, which is equivalent to the Hamiltonian described in Eqs. (S.D14)-(S.D19). This conclusion can be applied to other 2D Γ -valley moiré materials under the assumption $T_{M0} \gg |T_M(\mathbf{g} \neq 0)|$.

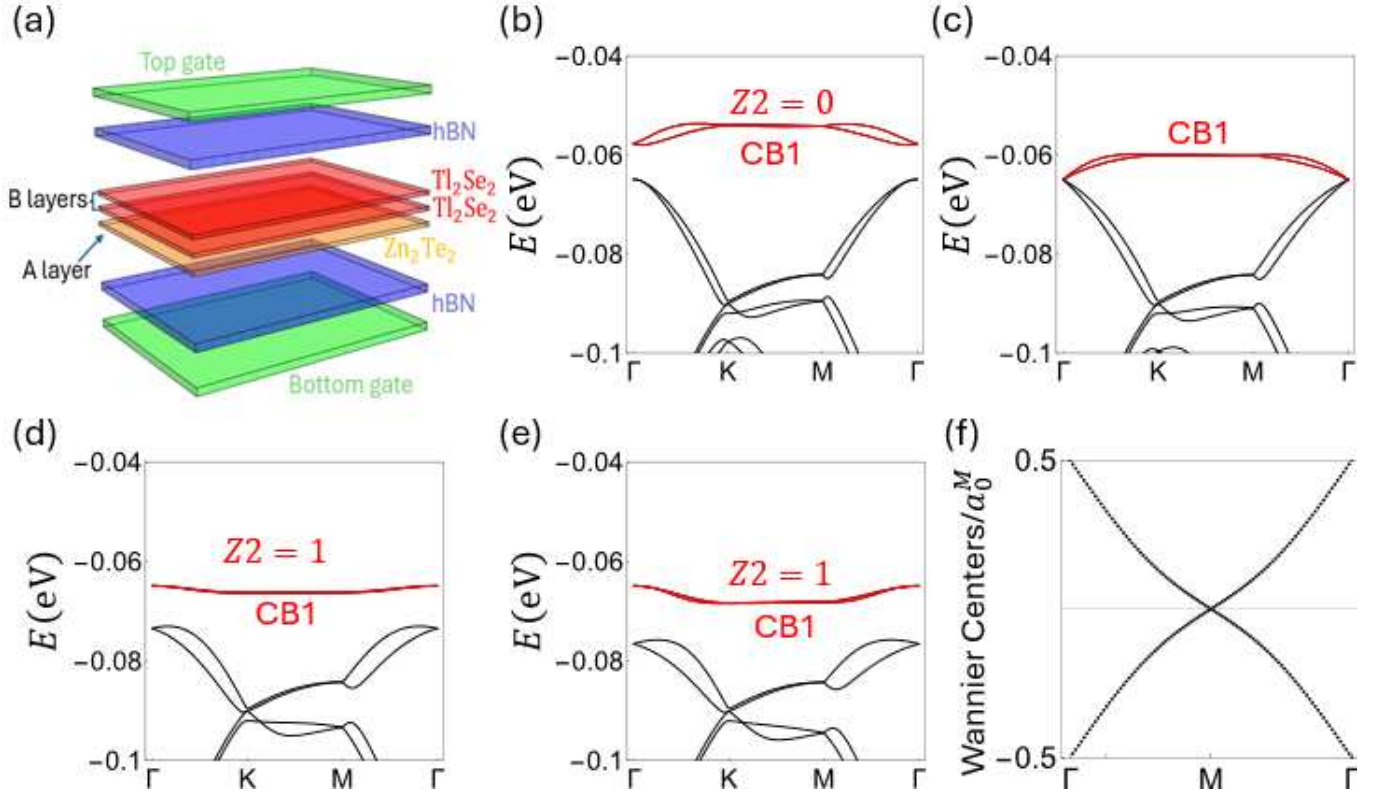


FIG. S14: (a) shows the schematics for the heterostructure with twisted Tl_2Se_2 bilayer and Zn_2Te_2 . In this setup, the twisted Tl_2Se_2 bilayer serves as part B while the Zn_2Te_2 monolayer serves as the layer A for our general scenario in Fig. 1 of the main text. (b)-(e) show the band dispersions with $\Delta_0 = 0.019\text{eV}$, 0.0213eV , 0.024eV and 0.025eV . (f) shows the Wannier center flow of CB1 highlighted in red in panel (d).

-
- [1] X.-L. Qi, Y.-S. Wu, and S.-C. Zhang, Topological quantization of the spin hall effect in two-dimensional paramagnetic semiconductors, *Physical Review B—Condensed Matter and Materials Physics* **74**, 085308 (2006).
 - [2] C.-Z. Chang, C.-X. Liu, and A. H. MacDonald, Colloquium: Quantum anomalous hall effect, *Reviews of Modern Physics* **95**, 011002 (2023).
 - [3] B. A. Bernevig, T. L. Hughes, and S.-C. Zhang, Quantum spin hall effect and topological phase transition in hgte quantum wells, *science* **314**, 1757 (2006).
 - [4] X.-L. Qi and S.-C. Zhang, Topological insulators and superconductors, *Reviews of modern physics* **83**, 1057 (2011).
 - [5] E. Y. Andrei and A. H. MacDonald, Graphene bilayers with a twist, *Nature materials* **19**, 1265 (2020).
 - [6] K. F. Mak and J. Shan, Semiconductor moiré materials, *Nature Nanotechnology* **17**, 686 (2022).
 - [7] T. Devakul, V. Crépel, Y. Zhang, and L. Fu, Magic in twisted transition metal dichalcogenide bilayers, *Nature communications* **12**, 6730 (2021).
 - [8] C. Forsythe, X. Zhou, K. Watanabe, T. Taniguchi, A. Pasupathy, P. Moon, M. Koshino, P. Kim, and C. R. Dean, Band structure engineering of 2d materials using patterned dielectric superlattices, *Nature nanotechnology* **13**, 566 (2018).
 - [9] D. Q. Wang, Z. Krix, O. P. Sushkov, I. Farrer, D. A. Ritchie, A. R. Hamilton, and O. Klochan, Formation of artificial fermi surfaces with a triangular superlattice on a conventional two-dimensional electron gas, *Nano Letters* **23**, 1705 (2023).
 - [10] C. Liu, T. L. Hughes, X.-L. Qi, K. Wang, and S.-C. Zhang, Quantum spin hall effect in inverted type-ii semiconductors, *Physical review letters* **100**, 236601 (2008).
 - [11] D. Rothe, R. Reinthaler, C. Liu, L. Molenkamp, S. Zhang, and E. Hankiewicz, Fingerprint of different spin-orbit terms for spin transport in hgte quantum wells, *New Journal of Physics* **12**, 065012 (2010).
 - [12] Z.-D. Song and B. A. Bernevig, Magic-angle twisted bilayer graphene as a topological heavy fermion problem, *Physical review letters* **129**, 047601 (2022).
 - [13] Z. Song, Z. Wang, W. Shi, G. Li, C. Fang, and B. A. Bernevig, All magic angles in twisted bilayer graphene are topological, *Physical review letters* **123**, 036401 (2019).
 - [14] C. Fang, M. J. Gilbert, and B. A. Bernevig, Bulk topological invariants in noninteracting point group symmetric insulators, *Physical Review B—Condensed Matter and Materials Physics* **86**, 115112 (2012).

- [15] B. Bradlyn, L. Elcoro, J. Cano, M. G. Vergniory, Z. Wang, C. Felser, M. I. Aroyo, and B. A. Bernevig, Topological quantum chemistry, *Nature* **547**, 298 (2017).
- [16] M. Vergniory, L. Elcoro, Z. Wang, J. Cano, C. Felser, M. Aroyo, B. A. Bernevig, and B. Bradlyn, Graph theory data for topological quantum chemistry, *Physical Review E* **96**, 023310 (2017).
- [17] L. Elcoro, B. Bradlyn, Z. Wang, M. G. Vergniory, J. Cano, C. Felser, B. A. Bernevig, D. Orobengoa, G. Flor, and M. I. Aroyo, Double crystallographic groups and their representations on the bilbao crystallographic server, *Journal of Applied Crystallography* **50**, 1457 (2017).
- [18] J. M. Luttinger, Quantum theory of cyclotron resonance in semiconductors: General theory, *Physical review* **102**, 1030 (1956).
- [19] R. Winkler, *Spin-orbit coupling effects in two-dimensional electron and hole systems*, Vol. 191 (Springer, 2003).
- [20] Y. Peter and M. Cardona, *Fundamentals of semiconductors: physics and materials properties* (Springer Science & Business Media, 2010).
- [21] S. G. Stewart, Heavy-fermion systems, *Reviews of Modern Physics* **56**, 755 (1984).
- [22] A. C. Hewson, The kondo problem to heavy fermions, Cambridge, UK: Cambridge Univ. Press Crossref Google Scholar Article Location More AR articles citing this reference Pushing Boundaries: My Personal and Scientific Journey Myriam P. Sarachik Department of Physics, City College of the City University of New York, NY **10031**, 1 (1993).
- [23] N. Marzari, A. A. Mostofi, J. R. Yates, I. Souza, and D. Vanderbilt, Maximally localized wannier functions: Theory and applications, *Reviews of Modern Physics* **84**, 1419 (2012).
- [24] A. A. Mostofi, J. R. Yates, Y.-S. Lee, I. Souza, D. Vanderbilt, and N. Marzari, wannier90: A tool for obtaining maximally-localised wannier functions, *Computer physics communications* **178**, 685 (2008).
- [25] Z. Fisk, J. L. Sarrao, J. Smith, and J. Thompson, The physics and chemistry of heavy fermions., *Proceedings of the National Academy of Sciences* **92**, 6663 (1995).
- [26] J. Wang, J. Cano, A. J. Millis, Z. Liu, and B. Yang, Exact landau level description of geometry and interaction in a flatband, *Physical review letters* **127**, 246403 (2021).
- [27] P. J. Ledwith, A. Vishwanath, and D. E. Parker, Vortexability: A unifying criterion for ideal fractional chern insulators, *Physical Review B* **108**, 205144 (2023).
- [28] R. B. Laughlin, [Kronig-penny model in higher dimension](#) (2007).
- [29] G. Kresse and J. Furthmüller, Efficiency of ab-initio total energy calculations for metals and semiconductors using a plane-wave basis set, *Computational materials science* **6**, 15 (1996).
- [30] J. Heyd, G. E. Scuseria, and M. Ernzerhof, Hybrid functionals based on a screened coulomb potential, *The Journal of chemical physics* **118**, 8207 (2003).
- [31] A. Zee, *Group theory in a nutshell for physicists* (Princeton University Press, 2016).
- [32] M. Angeli and A. H. MacDonald, γ valley transition metal dichalcogenide moiré bands, *Proceedings of the National Academy of Sciences* **118**, e2021826118 (2021).
- [33] Y. Zhang, T. Liu, and L. Fu, Electronic structures, charge transfer, and charge order in twisted transition metal dichalcogenide bilayers, *Physical Review B* **103**, 155142 (2021).
- [34] M. Claassen, L. Xian, D. M. Kennes, and A. Rubio, Ultra-strong spin-orbit coupling and topological moiré engineering in twisted zrs2 bilayers, *Nature communications* **13**, 4915 (2022).